ORNL/MD/LTR-199
Revision 0

MOX Average Power Intermediate PIE: 21 GWd/MT Final Report

R.N. Morris
C.A. Baldwin
S.A. Hodge
L.J. Ott
C.M. Malone
N.H. Packan

December 2000

Fissile Materials Disposition Program

Notice

This report was prepared as an account of work sponsored by an agency of the United States Government. Neither the United States Government nor any agency thereof, or any of their employees, makes any warranty, expressed or implied, or assumes any legal liability or responsibility for the accuracy, completeness, or usefulness of any information, apparatus, product, or process disclosed, or represents that its use would not infringe privately owned rights. Reference herein to any specific commercial product, process, or service by trade name, trademark, manufacturer, or otherwise, does not necessarily constitute or imply its endorsement, recommendation, or favoring by the United States Government or any agency thereof. The views and opinions of authors expressed herein do not necessarily state or reflect those of the United States Government or any agency thereof.

Revision History

Revision number	Date Issued	Reason for revision
0	December 2000	First Issue

OAK RIDGE NATIONAL LABORATORY
MANAGED BY UT-BATTELLE FOR THE DEPARTMENT OF ENERGY

Post Office Box 2008
Bldg. 3525, MS 6295, Room 104
Oak Ridge, TN 37831-6295
Phone: (865) 241-4237
Fax: (865) 576-7862
Email: morrisrn@ornl.gov

December 2000

Distribution

MOX Average Power Intermediate PIE: 21 GWd/MT Final Report

The enclosed document details the MOX Average Power Test PIE that was performed on the intermediate-withdrawal Capsules 2 and 9 under the guidance of the DOE-sponsored Fissile Materials Disposition Program (FMDP). This work was carried out at the Irradiated Fuels Examination Laboratory by the staff of the Metals and Ceramics Division of the Oak Ridge National Laboratory during the period from October 1999 though November 2000.

This is a Level-2 document as defined in the Fissile Materials Disposition Program Light-Water Reactor Mixed-Oxide Fuel Irradiation Test Project Plan, ORNL/MD/LTR-78, Rev 2.

Sincerely,

Robert N. Morris
Fissile Materials Disposition Program

Enclosure

Distribution: See Section 11 of enclosure

ORNL/MD/LTR-199
Revision 0

MOX Average Power Intermediate PIE: 21 GWd/MT Final Report

R.N. Morris
C.A. Baldwin
S.A. Hodge
L.J. Ott
C.M. Malone
N.H. Packan

December 2000

Oak Ridge National Laboratory

CONTENTS

List of Figures vii

List of Tables xii

Acronyms xiv

ABSTRACT xv

EXECUTIVE SUMMARY xvi

1. INTRODUCTION 1-1
    1.1 General 1-1
    1.2 Scope 1-2
    1.3 Gallium Migration 1-2
    1.4 Findings Concerning Improved Code Representation 1-2

2. PREIRRADIATION CHARACTERIZATION 2-1
    2.1 Fuel Types 2-1
    2.2 Irradiation Geometry 2-1
    2.3 Preirradiation Dimensional Data 2-7

3. IRRADIATION HISTORY AND PREDICTED RESPONSE FOR CAPSULES 2 AND 9 DURING PHASES I AND II 3-1
    3.1 Introduction 3-1
    3.2 Phase-I Irradiation History 3-2
    3.3 Phase-II Irradiation History 3-2
    3.4 Calculation Scope 3-5
    3.5 CARTS Results for Capsule Conditions During the Irradiation 3-6
        3.5.1 Cycle to Cycle Variations in Capsule Parameters 3-6
        3.5.2 Conditions at the End of the Phase-II Irradiation 3-11
    3.6 The Capsules in the Hot Cell 3-14
        3.6.1 Best-Estimate Results 3-16
        3.6.2 Conservative Results 3-16
    3.7 Summary and Conclusions 3-17
    3.8 Retrospective on CARTS Predictions 3-18

4. PIE METROLOGY OF CAPSULES 2 AND 9 4-1
    4.1 Capsule Photo Visual Inspection 4-1
    4.2 Capsule Temperature Measurement 4-6
    4.3 Capsule Dimensional Inspections 4-6

4.4 Capsule Gamma Scans 4-9
4.4.1 Capsule 2 Gamma Scan 4-10
4.4.2 Capsule 9 Gamma Scan 4-15
4.4.3 Gamma Scanner Data Collection Orientation 4-20
4.5 Fission Gas Measurement 4-20
4.6 Fuel Pin Photo Visual Inspections 4-23
4.7 Fuel Pin Dimensional Inspections 4-27
4.8 Metrology Summary 4-29

5. METALLOGRAPHY 5-1
5.1 Introduction 5-1
5.2 Sample Preparation 5-1
5.3 Results of the Polishing 5-1
5.4 Mount 6146 Etching 5-14
5.5 Gamma Scan of Mount 6145 5-18
5.6 SEM Analysis 5-21

6. APT MOX FUEL DENSIFICATION AND SWELLING 6-1
6.1 Introduction 6-1
6.2 Capsule Component Dimensions 6-2
6.2.1 Capsule Outer Diameter 6-2
6.2.2 Fuel Pin Outer- and Inner-Clad Diameters 6-2
6.2.3 Fuel-to-Clad Radial Gap 6-5
6.2.4 Fuel Pellet Outer Diameter 6-7
6.2.5 Conclusions from Dimensional Inspections of the Metallographic Mounts 6-8
6.3 Assessment of APT Fuel Densification and Swelling 6-9

7. RADIOCHEMISTRY RESULTS 7-1
7.1 Introduction 7-1
7.2 Gallium Analysis Results 7-1
7.3 Radiochemical Determination of Fuel Burnup 7-11

8. SUMMARY AND CONCLUSIONS 8-1
8.1 Fuel and Clad Performance Found Acceptable 8-1
8.2 Pellet Densification and Permanent Clad Expansion 8-2
8.3 Clad Samples Identified for Future Testing 8-2

9. ACKNOWLEDGMENTS 9-1

10. REFERENCES 10-1

11. DISTRIBUTION 11-1

FIGURES

Figure 2.1 Longitudinal cross section of the as-fabricated MOX fuel 2-2

Figure 2.2 Micrograph of unetched as-fabricated microstructure detailing porosity distribution. 2-2

Figure 2.3 Micrograph of etched as-fabricated microstructure detailing grain distribution. 2-2

Figure 2.4 Typical MOX pellet as fabricated at LANL for the average-power test 2-3

Figure 2.5 Capsule, fuel pin, and basket assemblies 2-4

Figure 2.6 Capsule and fuel pin axial dimensions 2-5

Figure 2.7 Pellet, fuel pin, and capsule radial dimensions 2-6

Figure 3.1 Dates, effective full-power days, and accumulated burnups for Capsules 2 and 9 during the Phase I irradiation cycles. 3-3

Figure 3.2 Dates, effective full-power days, and accumulated burnups during the Phase II irradiation cycles, for which Capsules 2 and 9 held the lead 3-4

Figure 3.3 Best-estimate results for Capsules 2 and 9 based upon minimum initial pellet-clad gaps and 0.50 percent densification 3-7

Figure 3.4 Best-estimate results for Capsules 2 and 9 based upon minimum initial pellet-clad gaps and zero densification 3-8

Figure 3.5 Best-estimate results for Capsules 2 and 9 based upon maximum initial pellet-clad gaps and zero densification 3-10

Figure 3.6 Conservative results for Capsules 2 and 9 based upon maximum initial gaps and 0.50 percent pellet densification 3-12

Figure 4.1 Side view of Capsule 2 4-3

Figure 4.2 Top view of Capsule 2 4-3

Figure 4.3 Bottom view of Capsule 2 4-4

Figure 4.4 Top view of Capsule 9 4-4

Figure 4.5 Side view of Capsule 9 4-5

Figure 4.6 Bottom view of Capsule 9 4-5

Figure 4.7 Free air temperature measurement on Capsule 9 4-7

Figure 4.8 Schematic of diameter measurement 4-9

Figure 4.9 Capsule 2 mid energy gamma raster scan 4-11

Figure 4.10 Capsule 2 high energy gamma raster scan 4-12

Figure 4.11 Capsule 2 mid energy gamma line scan 4-13

Figure 4.12 Capsule 2 high energy gamma line scan 4-14

Figure 4.13 Capsule 9 mid energy gamma raster scan 4-16

Figure 4.14 Capsule 9 high energy gamma raster scan. 4-17

Figure 4.15 Capsule 9 mid energy gamma line scan 4-18

Figure 4.16 Capsule 9 high energy gamma line scan 4-19

Figure 4.17 Orientation of the capsule and the gamma scanner collimator/detector 4-20

Figure 4.18 Cross sectional view of the Fission Gas Pressure Measuring Apparatus 4-21

Figure 4.19 Bottom end of Fuel Pin 5. Note the shortened pedestal from the cutting operation 4-23

Figure 4.20 Top end of Fuel Pin 5. Note the hole from the fission gas pressure measurement 4-24

Figure 4.21 Side view of Fuel Pin 5. Note capsule components in background 4-24

Figure 4.22 Bottom end of Fuel Pin 12. Note the shortened pedestal from the cutting operations 4-25

Figure 4.23 Top end of Fuel Pin 12. Note the hole from the fission gas pressure measurement. It also appears (top of hole) that the drill may have wandered or the pin may have rotated before the drill bit started cutting the hole 4-26

Figure 4.24 Side view of Fuel Pin 12. Note the capsule components in background 4-26

Figure 5.1 Composite view of Mount 6143. The plutonium rich agglomerates can be clearly seen 5-3

Figure 5.2 Composite view of Mount 6144. This level of cracking is considered normal. Note the plutonium rich agglomerates 5-4

Figure 5.3 Composite view of Mount 6145. Almost all the cracks are radial. The Black regions are epoxy filled pull-out areas. The agglomerates are clearly visible 5-5

Figure 5.4 Composite view of Mount 6146. Again, note the plutonium rich agglomerates and radial cracks 5-6

Figure 5.5 Graduated zoomed view of 1/4 of Mount 6144 5-7

Figure 5.6 Graduated zoom of Mount 6144 showing plutonium rich agglomerates in the outer radius regions 5-8

Figure 5.7 Graduated zoom of Mount 6144 showing the center region of the pellet 5-8

Figure 5.8 Closeup view of a group of agglomerates in Mount 6143. In general, the agglomerates were not uniformly distributed and some were rather large . 5-9

Figure 5.9 Closeup of Mount 6144 showing an agglomerate bonding to the clad 5-10

Figure 5.10 One of the larger agglomerates found in Mount 6144. Approximately 500 µm in diameter 5-10

Figure 5.11 High magnification view of an agglomerate in Mount 6145. Note the higher density of bubbles/voids 5-11

Figure 5.12 Medium magnification of the central region of Mount 6143. The central region lacks strong indications of agglomerates, although one may see a weak indication of an agglomerate in the lower left corner 5-12

Figure 5.13 High magnification view of the central region of Mount 6143. Generally, only small porosity is seen. Because of the higher temperature, the agglomerate structures likely have coalesced into the micron sized bubbles/voids 5-13

Figure 5.14 Composite view of Mount 6146 after etching. Note the plutonium rich agglomerates 5-15

Figure 5.15 Medium high magnification of the edge region of Mount 6146. Note the grain boundaries 5-16

Figure 5.16 High magnification view of the edge region of Mount 6146 5-16

Figure 5.17 Medium high magnification view of the central region of Mount 6146. The grain boundaries are less pronounced than at the edge region 5-17

Figure 5.18 High magnification view of the central region of Mount 6146 5-17

Figure 5.19 Data from raster scan of Mount 6145. The solid circles outline the approximate location of the clad 5-19

Figure 5.20 Smoothed data from the raster scan of Mount 6145. The solid circles outline the approximate location of the clad 5-20

Figure 5.21 Color map of an agglomerate and the nearby matrix. The agglomerate was at the fuel pellet mid radius 5-21

Figure 5.22 Electron backscatter view of the agglomerate and fuel matrix detailed in Figure 5.21 5-22

Figure 6.1 Cold clad inner and outer diameters as measured in APT MOX fuel pins 6-3

Figure 6.2 Cold radial pellet-to-clad gaps in APT MOX fuel pins 6-7

Figure 6.3 Cold pellet outer diameter in APT MOX fuel pins 6-9

Figure 6.4 Cold radial pellet-to-clad gaps in APT MOX fuel pins compared with ESCORE and FRAPCON model results 6-11

Figure 6.5 Cold pellet outer diameter in APT MOX fuel pins compared with ESCORE and FRAPCON model results 6-12

Figure 7.1 Fuel Pin 5 upper half cutting guide 7-2

Figure 7.2 Fuel Pin 5 bottom half cutting guide 7-3

Figure 7.3 Fuel Pin 12 top half cutting guide 7-5

Figure 7.4 Fuel Pin 12 bottom half cutting guide 7-6

TABLES

Table 2.1 ATR-MOX Capsule Preirradiation Information 2-7

Table 3.1 Results of CARTs Calculations for Capsules 2 and 9 Just Prior to End of Phase II 3-13

Table 3.2 CARTS Results for Capsules 2 and 9 Under Hot Cell Conditions 3-15

Table 4.1 Metrology Items 4-1

Table 4.2 Capsule and Fuel Pin Numbers 4-2

Table 4.3 Capsules 2 and 9 Temperature Measurements 4-6

Table 4.4 Capsule Measurements 4-8

Table 4.5 Fission Gas Measurements 4-22

Table 4.6 Fuel Pin Measurements 4-28

Table 5.1 Mount ID Numbers and Fuel Pellet Locations 5-1

Table 5.2 SEM Data 5-22

Table 6.1 Fuel Pin Metallographic Mount Identification 6-1

Table 6.2 Measured Fuel Pin Outer Diameters 6-4

Table 6.3 Fuel Pin Cladding Inner Diameter 6-4

Table 6.4 Fuel to Clad Radial Gap 6-6

Table 6.5 Fuel Outer Diameter 6-8

Table 7.1 Fuel Pin 5 Sampling 7-4

Table 7.2 Fuel Pin 12 Sampling 7-7

Table 7.3 Summary of RMAL Analysis Specimens 7-8

Table 7.4 Results of Gallium Analysis 7-9

Table 7.5 Bounding Gallium Mass Balance (Assumes Clad Starts with Zero Gallium) 7-10

Table 7.6 Fuel Burnup 7-11

Table 7.7 FP-5-P-1 Burnup 7-12

Table 7.8 FP-5-P-4 Burnup 7-13

Table 7.9 FP-12-P-1 Burnup 7-14

Table 8.1 Clad Samples Archived for Later Testing 8-3

ACRONYMS

APT	Average Power Test
ATR	Advanced Test Reactor
BOL	Beginning of Life
CARTS	Capsule Assembly Response-Thermal Swelling (Code)
EFPD	Effective Full Power Days
FGPMA	Fission Gas Pressure Measuring Apparatus
FMDP	Fissile Materials Disposition Program
GWd/MT	Giga-Watt Days per Metric Ton
INEEL	Idaho National Engineering and Environmental Laboratory
LANL	Los Alamos National Laboratory
LHGR	Linear Heat Generation Rate
LWR	Light Water Reactor
MCNP	Monte Carlo Neutron Photon (Code)
Mils	0.001 inches
MOX	Mixed Oxide
NRC	Nuclear Regulatory Commission
ORNL	Oak Ridge National Laboratory
PIE	Post Irradiation Examination
PPB	Parts Per Billion
PPM	Parts Per Million
PWR	Pressurized Water Reactor
RG	Reactor Grade
RMAL	Radioactive Materials Analysis Laboratory
TD	Theoretical Density
TIGR	Thermally Induced Gallium Removal
WG	Weapons Grade

ABSTRACT

This report summarizes the results of the post irradiation examination of the 21 GWd/MT MOX average power test capsules (numbers 2 and 9). The purpose of this examination was to document and monitor the progress of the MOX average power irradiation. Both capsules were examined, opened, and the fuel pin removed. Capsule 2 contained Fuel Pin 5 and Capsule 9 contained Fuel Pin 12. Both fuel pins were easily removed from the capsules and were found to be in excellent condition. Visual and dimensional inspections revealed no problems.

Measurement of the fission gas release fraction (1.5 to 2.0%) and fuel pellet stack gamma scan measurements indicate that the fuel is behaving satisfactorily. Metallographic mounts were prepared from both fuel pins and fuel behavior was examined with no indications of excessive swelling or fuel restructuring. One discovery during the PIE was that the range of plutonium rich agglomerates is larger than expected, up to approximately 500 µm in size.

Careful observation of the metallographic mounts indicates that the fuel densification has been greater than previously assumed, and there is evidence of irradiation-induced clad expansion (creep). Both of these effects are important in predicting changes in fuel dimensions as irradiation increases, and both will have to be represented in future code calculations.

The gallium content of the clad was in the sub ppm range indicating no significant migration of gallium from the fuel to the clad. Overall, both capsules underwent the irradiation with no detrimental effects and gallium migration/effects have not proved to be an issue.

EXECUTIVE SUMMARY

The post irradiation examination (PIE) of the second set of two capsules in a series being irradiated by the FMDP to investigate the properties of weapons grade (WG) plutonium in mixed-oxide (MOX) light-water reactor fuel is described in this report. This test irradiation and associated PIE series was deemed necessary because WG plutonium differs from reactor grade (RG) plutonium in both isotopic enrichment of ^{239}Pu and in trace impurities, particularly gallium. As set forth in the *Fissile Materials Disposition Program Light-Water Reactor Mixed Oxide Fuel Irradiation Test Project Plan*, ORNL/TM-13419, Rev 1, the goals include "Demonstrate the utilization of plutonium derived from weapons components in a light water reactor (LWR) environment," and "Contribute experience with irradiation of gallium-containing fuel to the data base required for resolution of generic LWR WG MOX fuel design issues." These goals are being pursued by examination of fuel pin material performance and, specifically, by focusing such examinations on the trace gallium behavior.

The MOX average power test capsules are irradiated in the Advanced Test Reactor (ATR) at INEEL and are being withdrawn for PIE in four phases, denoted early, intermediate, final, and extended. The purpose of this second examination at completion of the intermediate phase with a burnup of 21 GWd/MT is to monitor the progress of the irradiation so that it can be determined if the fuel is behaving in accordance with the performance models utilized in the pretest safety analyses. The two capsules undergoing the intermediate withdrawal PIE are Capsule 2, which provided containment during the irradiation for Fuel Pin 5, and Capsule 9, which served as containment for Fuel Pin 12. The MOX fuel within Fuel Pin 12 was created from PuO_2 that was treated by a TIGR (Thermally-Induced Gallium Removal) process before being blended with UO_2 and pressed into pellets. The MOX within Fuel Pin 5 was untreated.

As the first step of the PIE, both capsules were examined and gamma-scanned before opening. Both fuel pins were easily removed from the capsules and were found to be in excellent condition. Visual and dimensional inspections revealed no abnormalities. Pellet cracking was evident, but the extent is considered normal in view of the thermal cycling experienced during the Phase I & II irradiations. The pretest CARTS code application had predicted pellet-clad contact during the latter period of the irradiation. Although the pellet-clad gap as observed in the hot cell is smaller than that observed at the early PIE, it is now believed that pellet-clad contact will not occur until the fuel has attained higher burnups. This later gap closure is more representative of the power reactor experience.

Gamma scans provided qualitative indications of the burnup peaking along the fuel pin and within a pellet in agreement with the pretest neutronic predictions of the MCNP code. These inspections also showed that no axial gaps are developing within the fuel stack. Fission gas pressures were measured and the fractional fission gas release was determined to be between 1.5 and 2.0%, within the expected range.

Metallographic mounts were prepared from both fuel pins and fuel behavior was found to be in

accordance with expectations, with no indications of significant fuel restructuring or abnormal swelling. The fuel swelling is within the range predicted by the fuel performance models, but the pellet densification is found to be greater then previously estimated. An additional item of note is the presence of larger than expected plutonium rich agglomerates. Some agglomerates were as large as 500 µm, two to three times the size of the agglomerates expected in contemporary fuel. No irradiation difficulties have been experienced with these agglomerates, but they do indicate less than optimum powder mixing, more typical of the early MOX fuels.

Radiochemical determination of burnup is in good agreement with the code-predicted capsule-average value of about 21 GWd/MT. All indications are that the irradiation is proceeding as planned and that the fuel is performing normally.

Fuel performance code predictions depend upon input assumptions concerning the extent and duration of pellet densification. The fuel metrology for this PIE, when combined with results previously obtained for the early-withdrawal PIE, provide evidence that pellet densification has been in accordance with the European MOX experience. Previously, it had been thought that this test fuel would exhibit less densification because of the higher temperatures and longer duration of pellet sintering. It is now evident, however, that any effects of the more extensive sintering upon pellet densification have been minor.

Careful comparison of the present clad dimensions with the initial values, and with the values measured during the early-withdrawal PIE, indicate clad expansion, as would be caused by the combined effects of irradiation growth and outward clad creep. Care will be taken to check this finding, including the potential for eventual clad-capsule contact, in future PIEs.

Both fuel pins were sectioned to facilitate the tracking of gallium within the fuel pin clad. The gallium content of the clad was in the sub ppm range indicating no significant migration of gallium from the fuel to the clad (gallium in the sub ppm range has been found in unirradiated clad). Gallium contents of selected pellets were as expected as well. Samples of the clad have been set aside for later ductility testing.

The archiving of the clad samples pertains to the ultimate need to determine the effects, if any, of the transported gallium (if any) upon the clad. Toward this end, samples from the early and intermediate PIEs have been saved for ductility testing at a future time when apparatus for the destructive testing of clad specimens from this test series have been fabricated and installed within the hot cell.

The important lessons learned from this PIE of the intermediate-withdrawal capsules are as follows:

1. This test MOX fuel prepared with weapons-derived plutonium has behaved normally, and there is no cause to reconsider the extension of its test irradiation to higher burnups.

2. There is no significant difference between the performance of the TIGR-treated and the untreated MOX fuels.

3. Densification of the test fuel appears to be normal and prototypic of commercial fuel. Previous code predictions for this test were based on an assumed lesser degree of densification, but this will be rectified for future calculations.

4. Permanent outward relocation of the clad appears conclusive. The combination of outward creep and irradiation-induced clad growth (0.2% - 0.3%) is considered consistent with the operating conditions (positive outward pressure gradient across the fuel pin wall) and the accumulated fast neutron fluence. This clad displacement will be represented in future code calculations.

5. Measurement of capsule and fuel pin internal pressure and ^{85}Kr activity was successful. The implied gas release fraction from the fuel matrix is within the expectations based on the European MOX fuel experience.

6. The results of the gamma scans and burnup analyses are in accordance with the predictions of the MCNP code. The observed fuel swelling is as expected from CARTS code predictions. There is no reason to question the use of either the MCNP or CARTS codes in performing the safety analyses for irradiation of the test fuel to higher burnups.

7. Gallium migration to the clad appears to be insignificant. In this context, it is important to recognize that the fuel linear heat generation rate and the pellet-to-clad temperature difference has been larger for these test capsules then is expected for the mission fuel.

1. INTRODUCTION

1.1 General

The Fissile Materials Disposition Program (FMDP) is investigating the use of weapons-derived or weapons-grade (WG) plutonium in mixed oxide (MOX) fuel for light-water reactors (LWR). Commercial MOX fuel has been successfully used in overseas reactors for many years and a large data base has been generated for MOX fuel applications; however, weapons-derived fuel may differ from the commercial fuels in two ways. First, the isotopics of the fuel are different. Weapons-derived fuel contains greater amounts of ^{239}Pu and smaller amounts of the higher plutonium isotopes. Second, fuel derived from weapons material may contain trace amounts of gallium as an impurity. To pursue the disposition of surplus weapons-usable plutonium via reactor irradiation, it must be demonstrated that the unique properties of the WG Pu do not compromise the applicability of the existing MOX experience base.

It is the primary purpose of the current test irradiation to demonstrate that the substitution of weapons-derived plutonium for the reactor grade (RG) plutonium used in commercial MOX fuel does not negatively affect the performance of the fuel system and, thus, that the commercial database is applicable. To meet this end, the average-power test (APT) program has been created to fabricate, assemble, and irradiate small test capsules containing MOX fuel fabricated by Los Alamos National Laboratory (LANL) from weapons-derived plutonium [Refs. 1 to 8].

Simple, uninstrumented, drop-in capsules with local flux monitor wires were fabricated and placed in the Advanced Test Reactor (ATR) at Idaho National Engineering and Environmental Laboratory (INEEL). The average power test program comprises 13 capsules (including two archives), 7 of which contain MOX fuel prepared without a specific gallium removal step, and 6 of which contain fuel prepared with a gallium removal step. The target irradiation goal is 50 GWd/MT and capsules have been removed at 8 and 21 GWd/MT for the purpose of monitoring the effects of the irradiation. This report is the second in a series of post-irradiation examination reports and addresses the examination of the capsules irradiated to 21 GWd/MT. Such examinations are necessary to provide assurances that the fuel is performing as expected so that the ATR operators may have confidence in the continued irradiation of the remaining test capsules.

The basic Post Irradiation Examination (PIE) plan is detailed in Reference 9. While this report continues to provide the fundamental direction for the PIE effort, the good performance of the fuel and issues surrounding fuel system material gallium levels resulted in a shift of resources from the examination of fuel to the tracking of gallium in the clad. In addition, the issues surrounding the testing of the clad ductility were brought to the forefront and a relevant clad testing methodology has been developed for future application.

1.2 Scope

The purpose of this report is to document the PIE effort conducted on the second set of two average power test MOX capsules withdrawn from the ATR. The first three Chapters of this report summarize the fuel, the irradiation history, and performance predictions. The reader is referred to the references for greater detail and for the results of the first PIE.

The remaining Chapters 4 through 6 of this report detail the PIE work conducted and the results obtained. Radiochemistry results are discussed in Chapter 7. The goal was to perform a materials compatibility test rather than a fuels test, so the emphasis of the examination has been on the behavior of the fuel pin as a unit rather than the fuel; however, the fuel was examined to a degree sufficient to establish that no deviations from the expected are present. A qualitative gamma scan of a fuel segment has exhibited the expected off-center burnup profile. The clad is found to have behaved as expected during the irradiation. More critical examinations of the clad such as ductility testing are planned for the future when the necessary test apparatus has been fabricated and installed in the hot cell.

1.3 Gallium Migration

The test fuel contains gallium in excess of the upper concentration limit set for the mission fuel. Large amounts of gallium are known to adversely affect Zircaloy clad. Accordingly, it is of interest for this PIE to determine if gallium has migrated during the irradiation from the fuel to the clad. Results for the current PIE are discussed in Section 7.2.

1.4 Findings Concerning Improved Code Representation

Fuel Performance Models taken from the ESCORE and FRAPCON codes are applied before each PIE to predict the fuel configurations to be observed in the hot cell examinations. The predictions for the current PIE are described in Chapter 3. With respect to fuel densification, the current hot cell observations provide the third data point (following the initial and early-withdrawal values), and thereby permit refinement of the assumptions used in the previous code predictions. As discussed in Chapter 6, the observed pellet-clad gaps are larger than predicted. This is attributed to an outward irradiation-induced clad growth combined with an actual fuel densification greater than previously assumed.

2.0 PREIRRADIATION CHARACTERIZATION

2.1 Fuel Types

Two fuel types, which differ in their treatment of a common PuO_2 source, are included in the average-power test. Fuel type B was fabricated with plutonium dioxide that was subjected to a thermal treatment ("TIGR") for gallium removal prior to pellet fabrication. Fuel type A was fabricated with plutonium dioxide that was not treated. Ten pellets of each batch were analyzed at ORNL for gallium content [Ref 10]. Batch A had an average gallium content of 2.97 ppm (mass) while Batch B had a average gallium content of 1.33 ppm (mass). The 95% confidence interval for Batch A is 1.00 to 4.95 ppm and for Batch B, 0.79 to 1.88.

Tests were performed on the fuel during fabrication and the resulting characterization information was summarized in two pellet data packages prepared by Los Alamos National Laboratory (LANL). One archive capsule assembly of each fuel type was also prepared and sent to Oak Ridge National Laboratory (ORNL) unirradiated. These archives are available for future examination if questions arise regarding in-reactor performance. The unique fuel fabrication process and processing parameters that were utilized may influence the in-reactor performance of the APT fuel; the planned postirradiation examinations are meant to detect any such nonstandard behavior.

A longitudinal (pellet resting on side) cross section of the unirradiated fuel, Fig. 2.1, reveals the dish and chamfer of the pellets as well as the uniformity of the microstructure. Both batches of fuel contain 5% plutonium by weight. Chemical impurity analyses performed at LANL confirmed the presence of no contaminants above acceptable levels.

Both batches of fuel achieved high density in part due to the extended sintering schedule. Average immersion densities of 94.5 % TD and 95.3 % TD were measured on fuel types A and B respectively. Essentially no density change was achieved during a subsequent 24 hour thermal densification test. The porosity distribution includes a uniform distribution of fine pores, as shown in Fig. 2.2. The average grain size is 10 µm (fuel type A) and 11 µm (fuel type B). The unirradiated etched microstructure is shown in Fig. 2.3. A typical pellet is shown in Fig. 2.4.

2.2 Irradiation Geometry

The fuel pellets and stainless steel springs were loaded into Zircaloy clad fuel pins and the pins sealed by welding at Los Alamos. The pins were then transferred to Idaho National Engineering and Environmental Laboratory (INEEL), where they were loaded and seal welded into closely fitting stainless steel capsules (to meet the ATR pressure vessel operational requirements for this type of experiment as loaded into the reflector I-holes). Finally, the capsules were loaded into a basket assembly that was subsequently inserted into the ATR reflector for irradiation. Figs. 2.5 through 2.7 show the geometry of the configuration.

Figure 2.1 Longitudinal cross section of the as-fabricated MOX fuel.

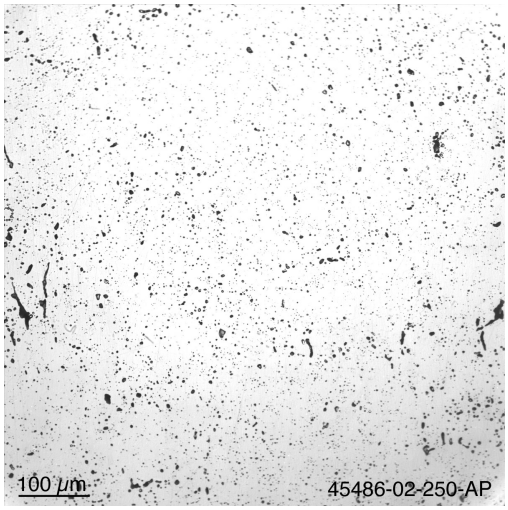

Figure 2.2 Micrograph of unetched as-fabricated microstructure detailing porosity distribution.

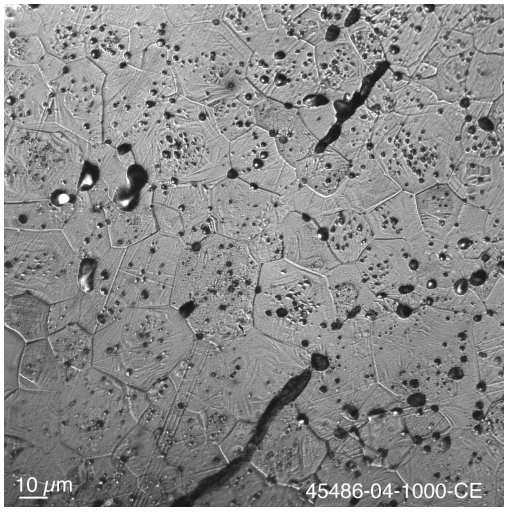

Figure 2.3 Micrograph of etched as-fabricated microstructure detailing grain distribution.

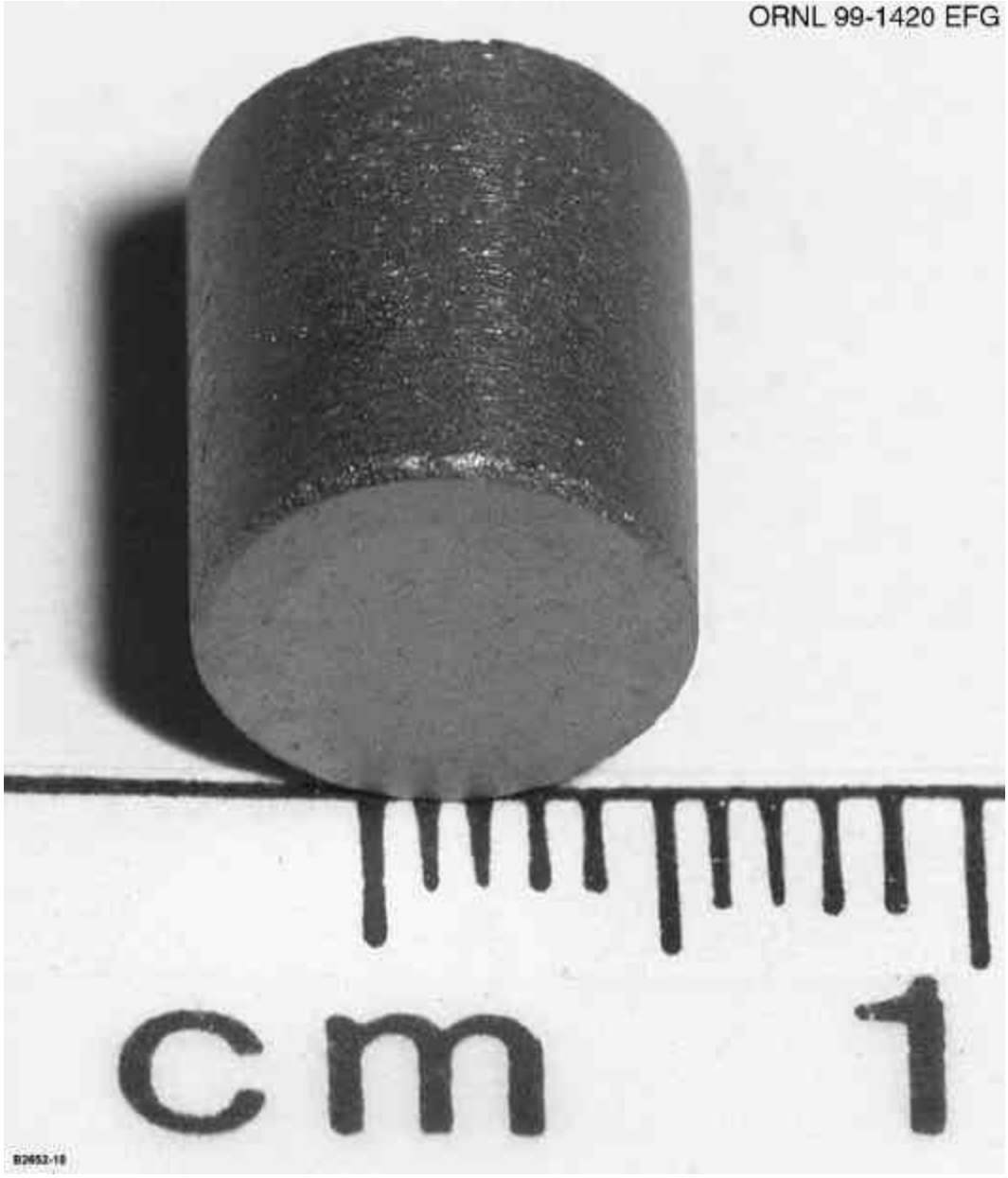

Figure 2.4 Typical MOX pellet as fabricated at LANL for the average-power test.

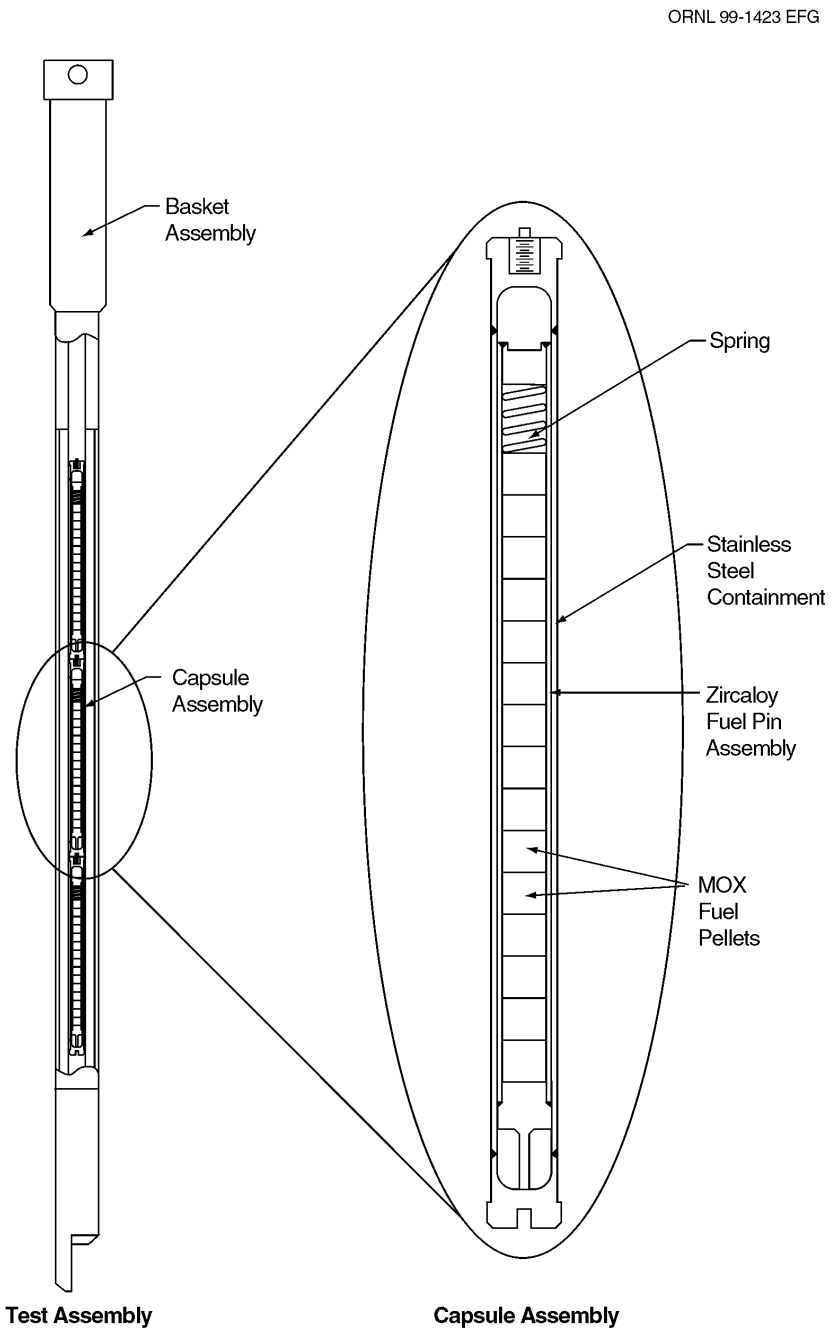

Figure 2.5 Capsule, fuel pin, and basket assemblies.

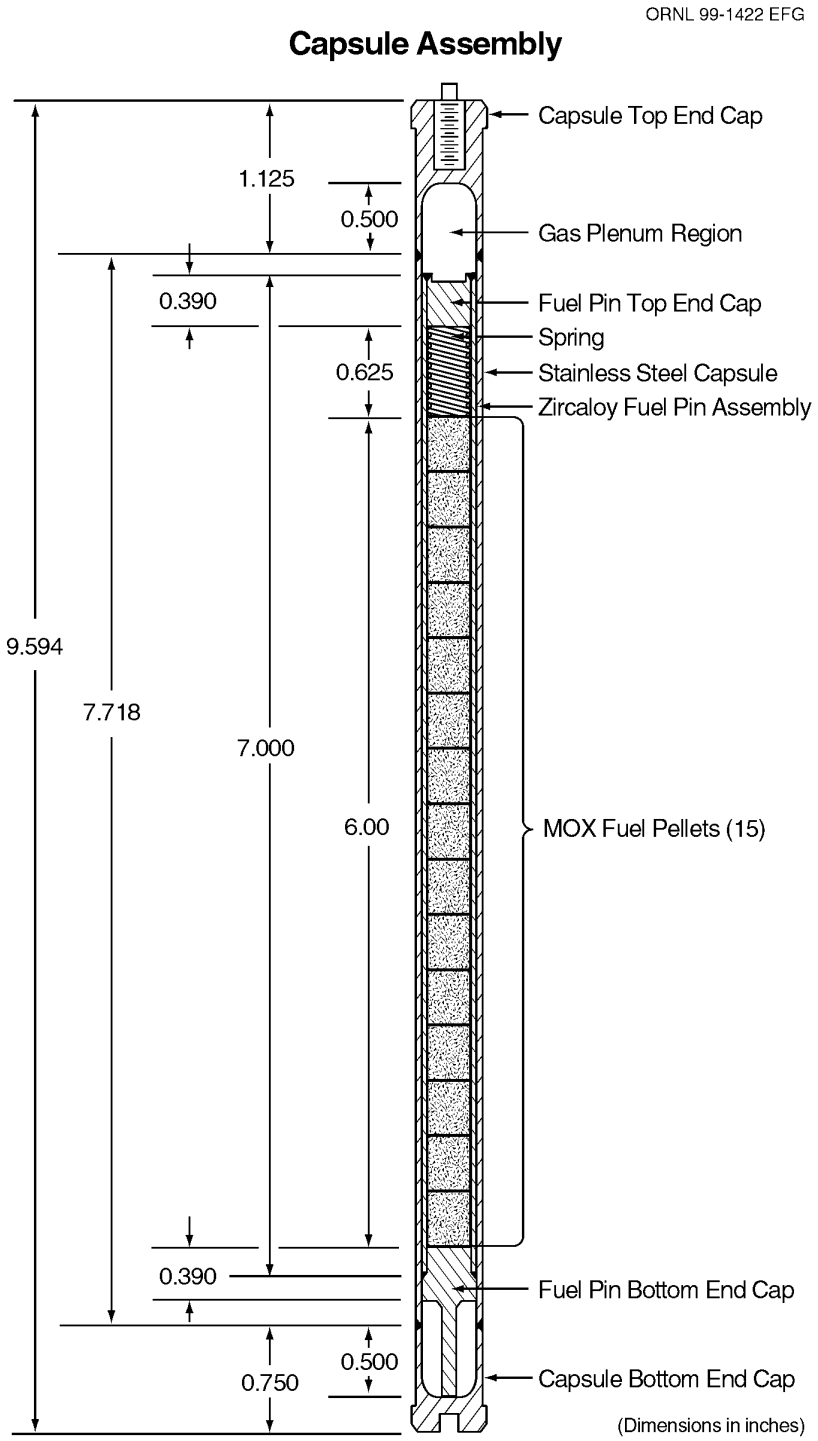

Figure 2.6 Capsule and fuel pin axial dimensions.

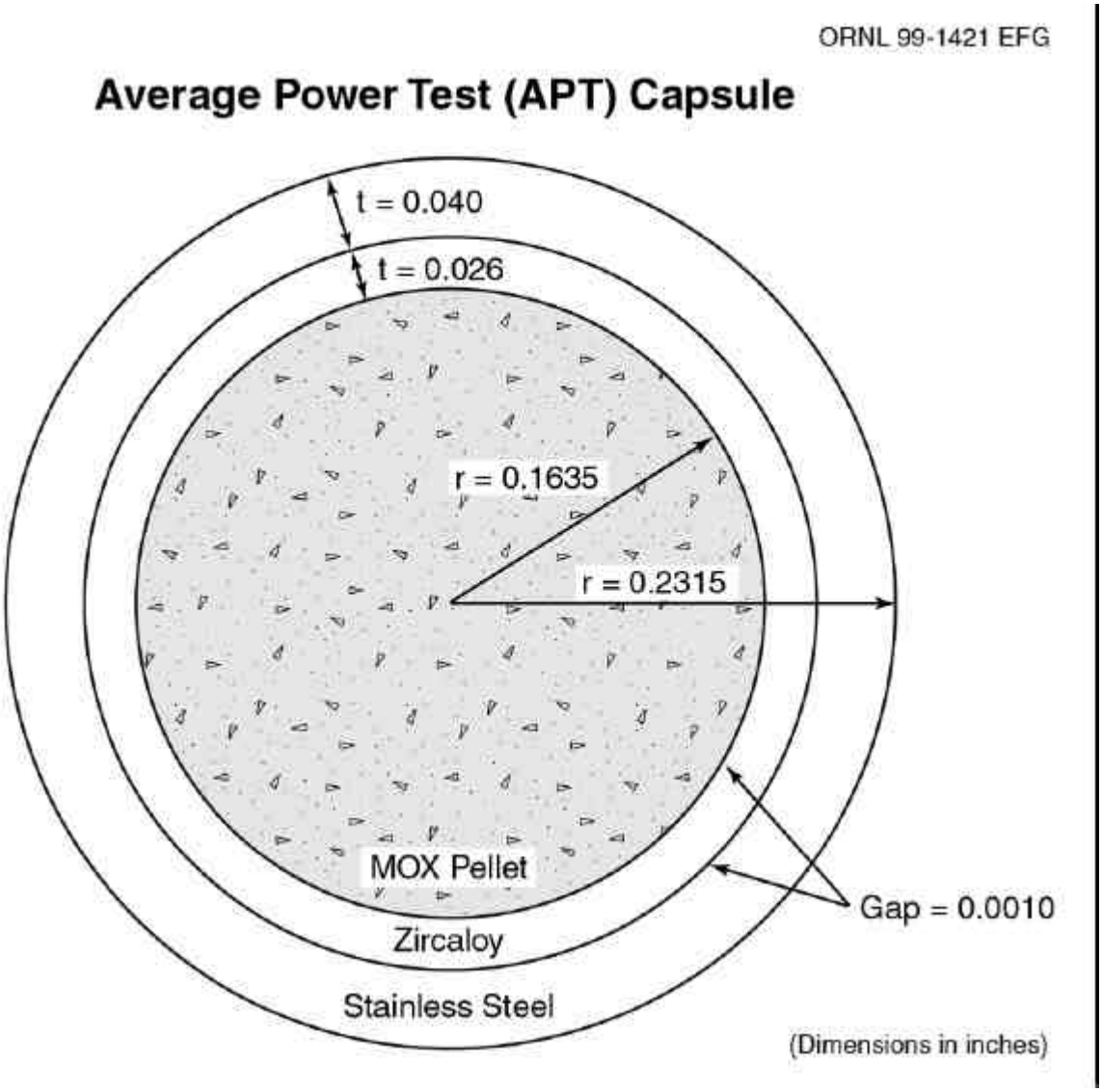

Figure 2.7 Pellet, fuel pin, and capsule radial dimensions.

2.3 Preirradiation Dimensional Data

Table 2.1 lists the dimensional data and part identification of the fuel capsule components prior to assembly.

TABLE 2.1
ATR-MOX Capsule Preirradiation Information

Capsule Number	**1**	**2**	**3**	**4**	**5**	**6**	**7**
Fuel Pin Number	2	5	6	7	8	9	10
Zr Tube Number	2	5	6	7	8	9	10
Zr Top Number	2	5	1	7	8	9	10
Zr Bottom Number	2	5	6	7	8	9	10
Zr Tube OD (inches)[1]	0.3806 0.3808	0.3806 0.3808	0.3805 0.3808	0.3805 0.3807	0.3806 0.3808	0.3805 0.3809	0.3806 0.3808
Zr Tube ID (inches)[1]	0.3290 0.3292	0.3290 0.3292	0.3290 0.3293	0.3291 0.3294	0.3290 0.3294	0.3290 0.3292	0.3290 0.3294
SS Tube OD (inches)[1]	0.4643 0.4649	0.4643 0.4649	0.4643 0.4649	0.4643 0.4649	0.4643 0.4649	0.4643 0.4649	0.4643 0.4649
SS Tube ID (inches)[1]	0.3830 0.3835	0.3830 0.3835	0.3830 0.3835	0.3830 0.3835	0.3830 0.3835	0.3830 0.3835	0.3830 0.3835
SS Top Number	1	2	3	4	5	6	7
Fuel Stack Height (inches)	5.821	5.833	5.859	5.816	5.816	5.829	5.823
Fuel Mass (grams)	81.41	81.63	80.51	81.40	81.31	81.66	81.47
Pellet Batch[2]	A	A	A	A	A	A	A
Burnup (GWd/MT)	8.6	21	30	40 (Planned)	50 (Planned)	50 (Planned)	None (Archive)

TABLE 2.1 (Cont.) ATR-MOX Capsule Preirradiation Information						
Capsule Number	**8**	**9**	**10**	**11**	**12**	**13**
Fuel Pin Number	11	12	13	14	15	16
Zr Tube Number	11	12	13	14	15	16
Zr Top Number	11	12	13	14	15	16
Zr Bottom Number	11	12	13	14	15	16
Zr Tube OD (inches)[1]	0.3806 0.3808	0.3806 0.3808	0.3805 0.3808	0.3805 0.3807	0.3805 0.3807	0.3806 0.3808
Zr Tube ID (inches)[1]	0.3290 0.3293	0.3290 0.3294	0.3292 0.3293	0.3292 0.3294	0.3290 0.3293	0.3291 0.3294
SS Tube OD (inches)[1]	0.4643 0.4649	0.4643 0.4649	0.4643 0.4649	0.4643 0.4649	0.4643 0.4649	0.4643 0.4649
SS Tube ID (inches)[1]	0.3830 0.3835	0.3830 0.3835	0.3830 0.3835	0.3830 0.3835	0.3830 0.3835	0.3830 0.3835
SS Top Number	8	9	10	11	12	13
Fuel Stack Height (inches)	5.810	5.810	5.813	5.810	5.795	5.790
Fuel Mass (grams)	82.26	82.23	82.29	82.20	82.00	81.84
Pellet Batch[2]	B	B	B	B	B	B
Burnup (GWd/MT)	8.6	21	30	None (Archive)	50 (Planned)	40 (Planned)

[1] Numerator is the smallest measurement, denominator is the largest measurement.
[2] Pellet batch A was fabricated with PuO_2 that was not treated. Pellet batch B was fabricated with PuO_2 that was thermally treated ("TIGR") for Ga removal prior to pellet fabrication.

3. IRRADIATION HISTORY AND PREDICTED RESPONSE FOR CAPSULES 2 AND 9 DURING PHASES I AND II

3.1 Introduction

For the MOX (mixed oxide) tests in the Advanced Test Reactor (ATR), the Capsule Assembly Response – Thermal Swelling (CARTS) code developed at ORNL (Oak Ridge National Laboratory) by Larry Ott is used to predict fuel and structural status for each of the planned periods of irradiation. In addition to calculating the interplays between fuel swelling and the temperatures and thermal expansions of the fuel and structures, the CARTS models [Section 6.4 of Ref 11 and Section 3.3 of Ref 12] predict the internal pressure associated with the fission gas released within the fuel pin.

The intermediate-withdrawal PIE (postirradiation examination) has been performed on Capsules 2 and 9, which occupied the two lower front positions within the test assembly during the Phase-I and -II irradiations [Ref. 8].

To provide the component temperature and pellet swelling histories of the intermediate-withdrawal capsules as necessary to interpretation of the associated PIE results, CARTS has been applied to predict the pellet, fuel pin, and capsule behaviors during the Phase-I and Phase-II irradiations. In essence, the CARTS code has provided the quasi-steady state coupled thermal/mechanical solution at each point in a series of stepwise advances in fuel burnup. Code output includes the pellet, clad, and capsule temperatures; the pressure- and temperature-induced radial dimensional changes of the fuel pin and capsule walls; and the associated wall strains.

The following Section describes the Phase-I irradiation of the Average-Power Test, during which Capsules 2 and 9 accumulated about 8.34 GWd/MT. The Phase-II irradiation, during which these intermediate-withdrawal capsules attained a final burnup of 20.9 GWd/MT, is discussed in Section 3.3. Section 3.4 describes the manner in which the CARTS code calculations were carried out, including the assumptions considered in the various cases for pellet initial size and the extent of pellet densification during irradiation. The calculated conditions within the test capsules at the end of the irradiation are discussed in Section 3.5. The calculated status of the capsule components at the time that the capsules were introduced to the hot cells for PIE purposes is addressed in Section 3.6. Section 3.7 provides a summary of the calculated results and associated conclusions.

The CARTS calculations whose results are documented in this Chapter were performed in advance of the PIE. These results represent both the expected operating behavior of the fuel pin and capsule during irradiation and the predicted conditions of the fuel, clad, and capsule when subsequently observed in the hot cell. The post-PIE CARTS analyses based on the actual observations are discussed in Chapter 6 of this report.

3.2 Phase-I Irradiation History

Phase I of the Average-Power Test is defined as the period of irradiation before withdrawal of Capsules 1 and 8 for the early PIE [Ref. 13]. Phase I extended from February 5 until September 13, 1998, and comprised ATR Cycles 115C through 117B. During this period, the test assembly experienced 154.9 effective full power days (EFPDs) of irradiation in the Northwest I-hole position I-24. Figure 3.1 illustrates the Phase-I irradiation cycles with their calendar dates and the associated accumulations of EFPDs and calculated burnups for the intermediate-withdrawal capsules.

The Inconel shield basket assembly (Model 1) was employed throughout. The average linear heat generation rates (LHGRs) and accumulated burnups for Capsules 2 and 9 during the Phase-I cycles are as follows:

8.41 kW/ft for	0.00	to	2.78 GWd/MT	–	Cycle 115C	(48.4 EFPDs)
7.97 kW/ft for	2.78	to	3.45 GWd/MT	–	Cycle 116A	(12.8 EFPDs)
8.47 kW/ft for	3.45	to	4.70 GWd/MT	–	Cycle 116B	(22.2 EFPDs)
7.65 kW/ft for	4.70	to	5.42 GWd/MT	–	Cycle 117A	(14.1 EFPDs)
7.62 kW/ft for	5.42	to	8.34 GWd/MT	–	Cycle 117B	(57.4 EFPDs).

These EFPD totals for each cycle are as reported in the INEEL letter “Advanced Test Reactor (ATR) Power History Through Cycle 120B-2,” DSL-07-99 dated October 7, 1999. The cycle-averaged LHGRs and accumulated burnups are taken from the MCNP (Monte Carlo N-Particle) code results calculated at INEEL. Because Capsules 2 and 9 occupied similar (left and right front-bottom) positions in the test assembly, these results are considered to apply equally to both.

There were two brief unplanned ATR shutdowns during Cycle 115C and one during Cycle 116A. Thus, the test capsules were thermally cycled eight times during the five ATR operation cycles of the Phase-I irradiation.

3.3 Phase-II Irradiation History

The Phase-II irradiation began on November 9, 1998, with ATR Cycle 118A and continued through Cycle 120A, which ended September 12, 1999. The Model-2 aluminum-shield basket assembly was employed throughout. The test assembly was loaded with seven capsules carried over from Phase I, plus the two fresh fuel capsules that replaced the capsules withdrawn for the early PIE. Capsules 2 and 9 occupied the same left and right front-bottom positions for Phase II that they had occupied during Phase I [Ref. 8].

During Phase II, the test assembly accumulated 227.7 EFPDs in the Northwest I-hole position I-24. Figure 3.2 illustrates these irradiation periods with their calendar dates and the associated accumulations of EFPDs and burnups for both the capsules carried over from Phase I and the two fresh fuel capsules. Capsules 2 and 9 were the lead capsules during Phase II, and as such, the burnups listed along the top of the shaded area shown in Figure 3.2 apply to them.

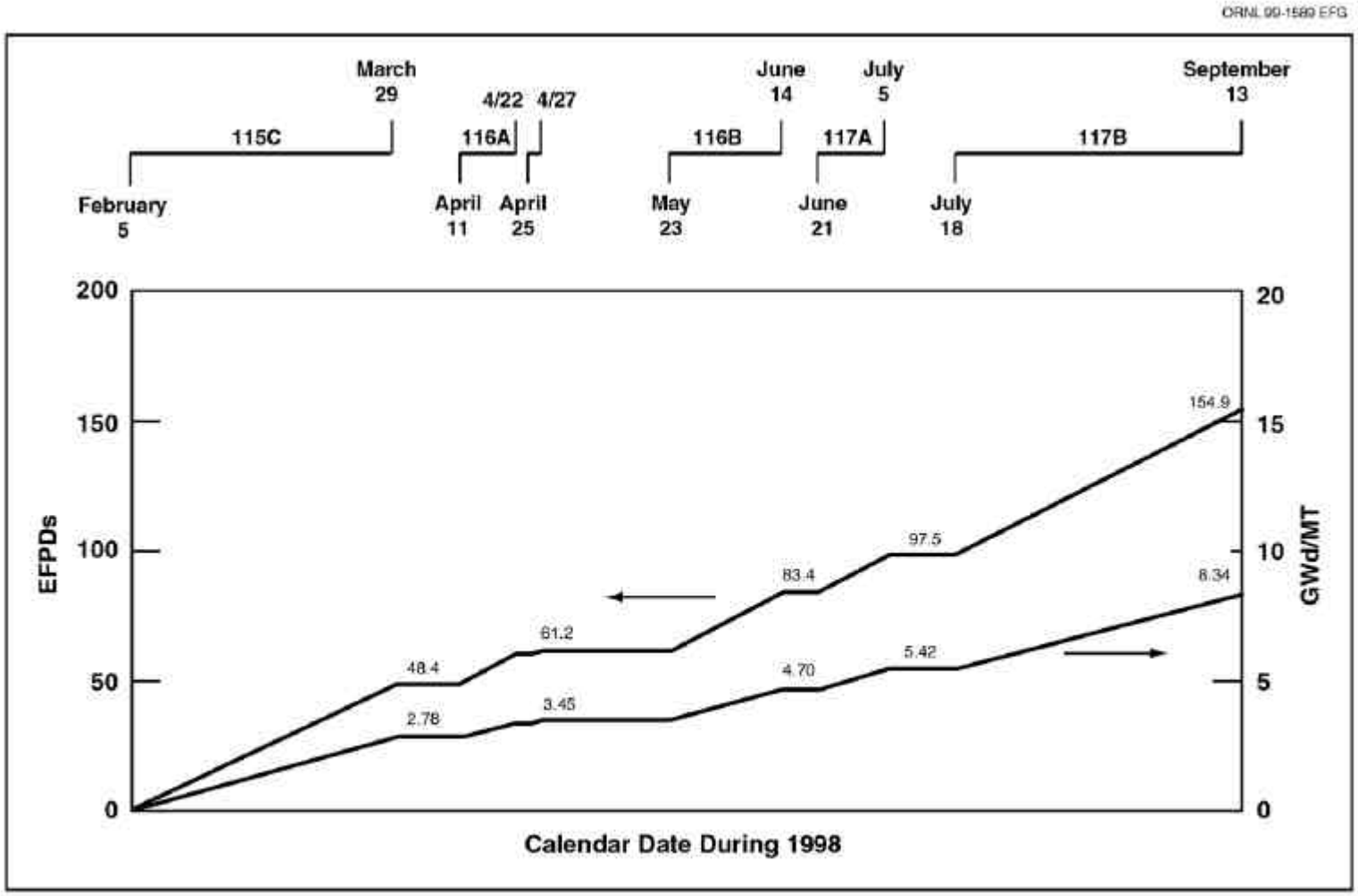

Figure 3.1. Dates, effective full-power days, and accumulated burnups for capsules 2 and 9 during the Phase I irradiation cycles.

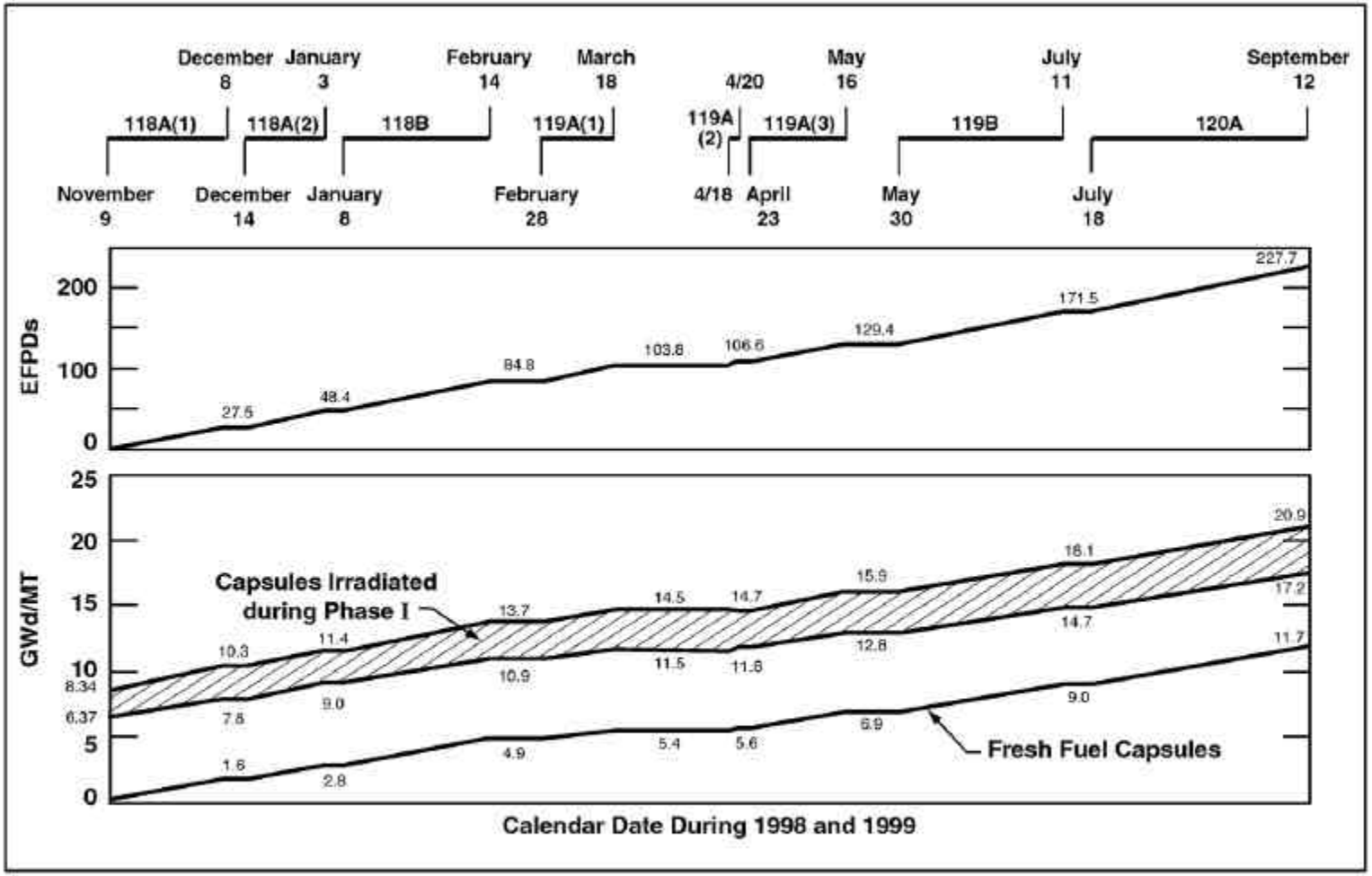

Figure 3.2. Dates, effective full-power days, and accumulated burnups during the Phase II irradiation cycles, for which capsules 2 and 9 held the lead.

The CARTS code input for Capsules 2 and 9 during Phase II represents the following LHGR history:

9.56 kW/ft for	8.34	to	10.34 GWd/MT	–	Cycle 118A(1)	(27.5 EFPDs)
9.52 kW/ft for	10.34	to	11.44 GWd/MT	–	Cycle 118A(2)	(20.9 EFPDs)
9.41 kW/ft for	11.44	to	13.70 GWd/MT	–	Cycle 118B	(36.4 EFPDs)
7.05 kW/ft for	13.70	to	14.48 GWd/MT	–	Cycle 119A(1)	(19.0 EFPDs)
9.38 kW/ft for	14.48	to	14.67 GWd/MT	–	Cycle 119A(2)	(2.8 EFPDs)
9.24 kW/ft for	14.67	to	15.87 GWd/MT	–	Cycle 119A(3)	(22.8 EFPDs)
9.79 kW/ft for	15.87	to	18.15 GWd/MT	–	Cycle 119B	(42.1 EFPDs)
7.37 kW/ft for	18.15	to	20.93 GWd/MT	–	Cycle 120A	(56.2 EFPDs).

With two brief unplanned shutdowns during Cycle 118B and one during Cycle 120A, the test capsules were thermally cycled 11 times during the eight ATR operational cycles that make up Phase II.

Combining the Phase-I and Phase-II experiences, Capsules 2 and 9 accumulated a total of 382.6 EFPDs and underwent 19 thermal cycles. The overall burnup-averaged LHGR for these capsules is 8.56 kW/ft. The highest LHGR was 9.79 kW/ft near the end of Phase II.

The LHGRs and burnup accumulations for both Phases I and II are taken from the as-run MCNP code results obtained at INEEL at the conclusion of each ATR cycle. Uncertainties in these MCNP results, estimated to be +/- 2.5 percent, are not addressed in the CARTS code calculations, which are run using the base MCNP values only.

3.4 Calculation Scope

Eight CARTS calculations have been run for the intermediate-withdrawal capsules, each based upon the burnup accumulations and the average LHGRs during ATR Cycles 115C through 120A as described in the previous two Sections. The three parameters varied are the initial pellet-to-clad and clad-to-capsule gaps (minimum versus maximum), the extent of pellet densification during irradiation (zero versus 0.5 percent), and the classification of assumptions (best estimate versus conservative).

As the name implies, the best-estimate calculations are believed to provide the most accurate predictions of the pellet, fuel pin, and capsule response during the various irradiation cycles. The set of four best-estimate calculation results provides a predicted range for the postirradiation gaps depending upon the initial gap size and the extent of the densification experienced by a pellet during the irradiation. The considered densification range of zero to 0.5 percent is based upon the observations of the early-withdrawal PIE [Ref. 13].

A set of conservative CARTS code results has also been obtained for the same variations of initial gap size and extent of pellet densification. For these four conservative cases, the gas gap

thermal conductance model and parameters such as material thermal conductivities and capsule/fluid surface heat-transfer coefficients were chosen in directions relative to the best-estimate values that tend to increase the calculated pellet temperature during reactor operation. This in turn causes increases in the predicted thermal expansion.

The CARTS calculations were advanced in burnup steps of 0.01 GWd/MT, with data printout every 0.10 GWd/MT. Timestep independence was confirmed by observing that results were virtually the same when one set was repeated with steps of 0.005 GWd/MT. Since the irradiation histories of Capsules 2 and 9 are nearly identical, the calculations were run for the averages of the as-run LHGRs. As explained previously, these two capsules were in symmetric locations within the test assembly with respect to the core. Their LHGRs were always in close agreement (maximum difference was about 0.6 percent), and hence the CARTS results discussed here are considered applicable to either capsule.

The final burnup advancement step in each CARTS calculation represents conditions at the time (January 2000) when the capsules were opened within the hot cell. For this final step, the fuel pellets are heated internally by decay power, while heat transfer from the outer capsule surface is by convection to the hot cell atmosphere.

3.5 CARTS Results for Capsule Conditions During the Irradiation

For the Average-Power Test, each capsule surrounds a fuel pin containing 15 MOX pellets. Each pellet has unique dimensions within the specified fabrication tolerances, so that a spectrum of initial pellet-to-clad gaps and irradiation-induced pellet densifications exists within each fuel pin. Before discussing the conditions predicted for the capsule components in the hot cell, it is of interest to first consider the variations in pellet temperatures and diametral gaps as calculated for the period of reactor operation, with particular attention to the conditions at the end of Phase II, just prior to removal of the intermediate-withdrawal capsules for PIE. In accordance with the experience documented in the literature, the CARTS code input for these calculations provides that pellet densification (if any) be completed before burnup exceeds 10 GWd/MT.

3.5.1 Cycle to Cycle Variations in Capsule Parameters

Figure 3.3 illustrates the best-estimate results for variations in pellet mean temperature, pellet-clad diametral gap, and clad mechanical strain as calculated for pellets with the largest initial diameter (minimum initial pellet-clad gap), and assuming that the pellet densification is 0.50 percent. Figure 3.4 provides the same information, except that for this calculation, the pellet densification is assumed to be zero. In the interest of avoiding unnecessary clutter, the plots on

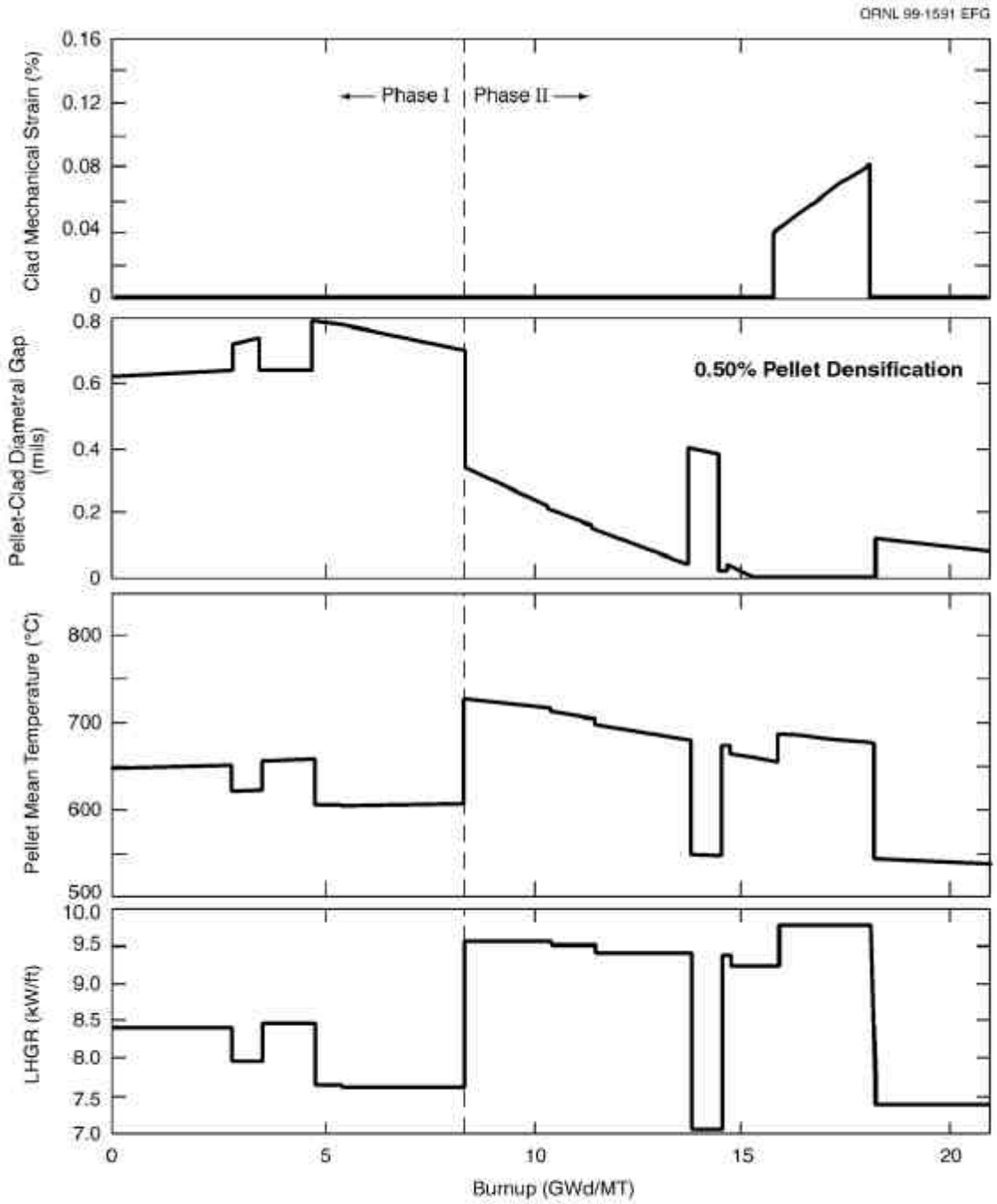

Figure 3.3. Best-estimate results for capsules 2 and 9 based upon minimum initial pellet-clad gaps and 0.50 percent densification.

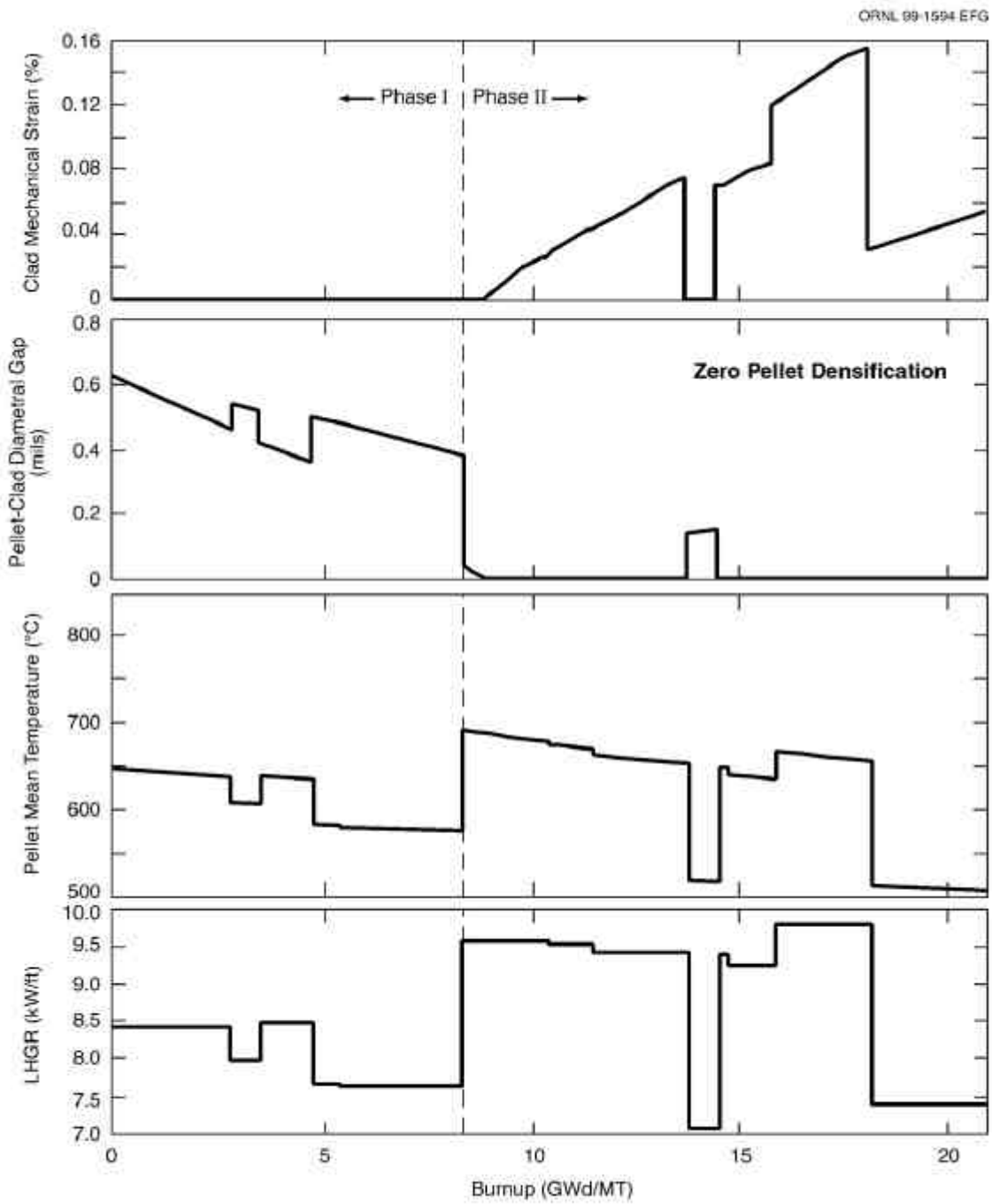

Figure 3.4. Best-estimate results for capsules 2 and 9 based upon minimum initial pellet-clad gaps and zero densification.

these figures do not include spikes to zero power to mark the between-cycle reactor outages, the periods of which are indicated on Figures 3.1 and 3.2.

The clad mechanical strain is the result of the internal force produced by the combination of internal pressure and any displacement by pellet swelling. (For the current calculations, the pressure force is negligible.) The CARTS code also calculates the total clad strain, which is the sum of the thermal strain and the mechanical strain.

For the pellets with minimum initial diametral gap (2.0 mils), Figures 3.3 and 3.4 show that pellet-clad contact did not occur during Phase I. Contact is predicted to have occurred just after the beginning of the first Phase-II Cycle 118A(1) for zero pellet densification or during the sixth Phase-II Cycle 119A(3) for 0.5 percent densification. As indicated in Section 3.3, LHGRs approached 10 kW/ft during the first two cycles of the Phase-II irradiation, so that the higher pellet temperatures and associated increased thermal expansion promoted gap closure.

The variations in pellet-clad diametral gap as shown on Figures 3.3 and 3.4 exhibit the expected behavior. Gap closure is promoted by both thermal expansion of the pellet and by fission product-induced swelling. Thus, the long-term progression toward gap closure by pellet swelling is subject to temporary reversals by gap increases whenever reductions in LHGR cause the pellet temperature to decrease. Pellet densification also tends to increase the gap, but this process is complete by 10 GWd/MT, and the effect is small, decreasing the calculated maximum clad mechanical strain during Phase II from 0.15 (Fig. 3.4) to 0.08 (Fig. 3.3). Nevertheless, it is solely the assumption of 0.5 percent pellet densification that causes the delay in gap closure in Figure 3.3 as compared to Figure 3.4.

For the pellets with maximum initial diametral gap (3.5 mils) and zero densification, Figure 3.5 shows that pellet-clad contact is also predicted to occur, but is delayed until the middle of Phase-II Cycle 119B, when the irradiation-induced swelling becomes sufficient to close the gap. (The diametral gap plot scale is larger in Fig. 3.5, as necessary to accommodate the larger initial gap.) The consistently larger gap for these pellets increases the resistance to heat transfer during the irradiation, as evidenced by the higher pellet temperatures (relative to Figs. 3.3 and 3.4) shown for these pellets, particularly during Phase I and the portion of Phase II before gap closure.

None of the best-estimate calculations predicts that pellet-clad contact occurred at any time during the Phase-I irradiation. As previously mentioned, no pellet-clad contact was predicted during Phase II for pellets with maximum initial gaps and 0.5 percent densification. (The minimum diametral gap predicted for these pellets is 0.04 mils at the end of Cycle 119B.)

When conservative values are selected for CARTS code input, pellet-clad contact is generally predicted to have been continuous during Phase II, and to have produced higher clad mechanical strains. As indicated in Figure 3.6, the only exception is for pellets with 0.5 percent densification and maximum initial gaps, where pellet contact with the clad is predicted to have been broken briefly during Cycle 119A(1), but reestablished thereafter.

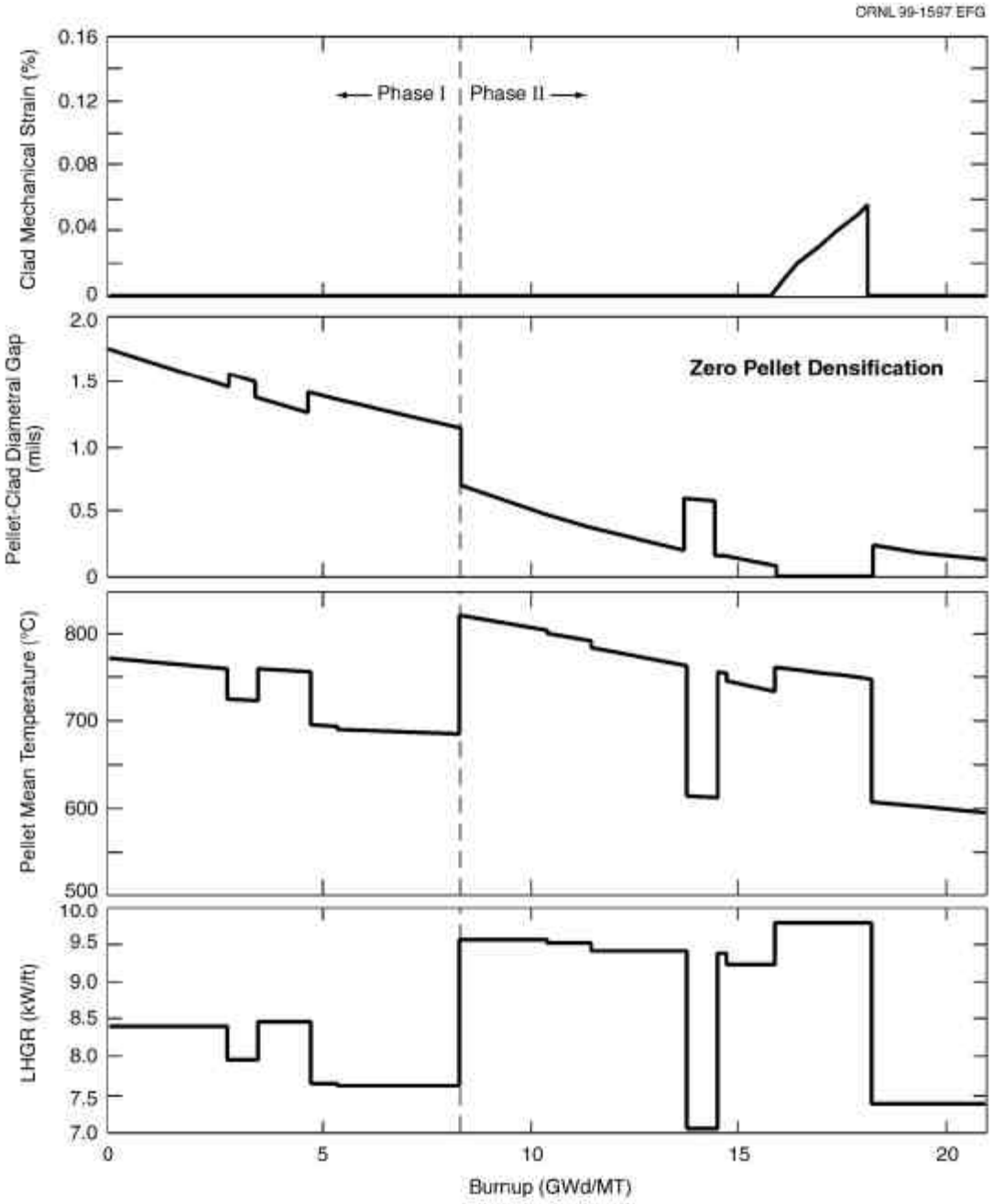

Figure 3.5. Best-estimate results for capsules 2 and 9 based upon maximum initial pellet-clad gaps and zero densification.

Neither the best estimate nor the conservative calculations predict any contact between the fuel pin and the capsule at any time during the irradiation.

3.5.2 Conditions at the End of the Phase-II Irradiation

Table 3.1 presents the results of the eight CARTS calculations for conditions in the intermediate-withdrawal capsules just prior to the completion of the Phase-II irradiation and their withdrawal for PIE. The last column of Table 3.1 indicates the durations of any predicted periods of pellet-clad contact.

Although the calculated capsule wall temperature is almost independent of assumptions concerning the initial pellet-clad diametral gap and the extent of pellet densification, the calculated clad temperature is lower for pellets with minimum initial gaps. During reactor operation at the end of Phase II, the clad temperature (272°–320°C) is much higher than the temperature (about 107°C) of the capsule wall, which is cooled on its outer surface by forced water convection. Further, the predicted mean pellet temperatures range from 508° to 621°C, so the pellets exhibit significant thermal expansion. (The pellet centerline temperatures range from 731° to 868°C.) Thus, although pellet-clad contact is not expected in the hot cell, periods of pellet-clad contact were predicted with the pellets at elevated temperatures during reactor operation.

As indicated in Table 3.1, the best-estimate CARTS code predictions of pellet-to-clad diametral gaps just prior to reactor shutdown from Cycle 120A range from zero to 0.28 mils. The accompanying clad mechanical strains range from 0.05 percent to zero. The largest predicted strain occurs for the case of zero pellet densification and minimum initial pellet-clad diametral gap (Figure 3.4), for which the maximum mechanical strain at any time during the irradiation is 0.15 percent.

Mechanical strain is predicted to have remained zero throughout the irradiation only for the best-estimate case of pellets with 0.5 percent densification combined with maximum initial diametral gap (first entry in Table 3.1). When thermal strains are added, the total clad strain just before shutdown is predicted to lie in the range from 0.16 to 0.11 percent.

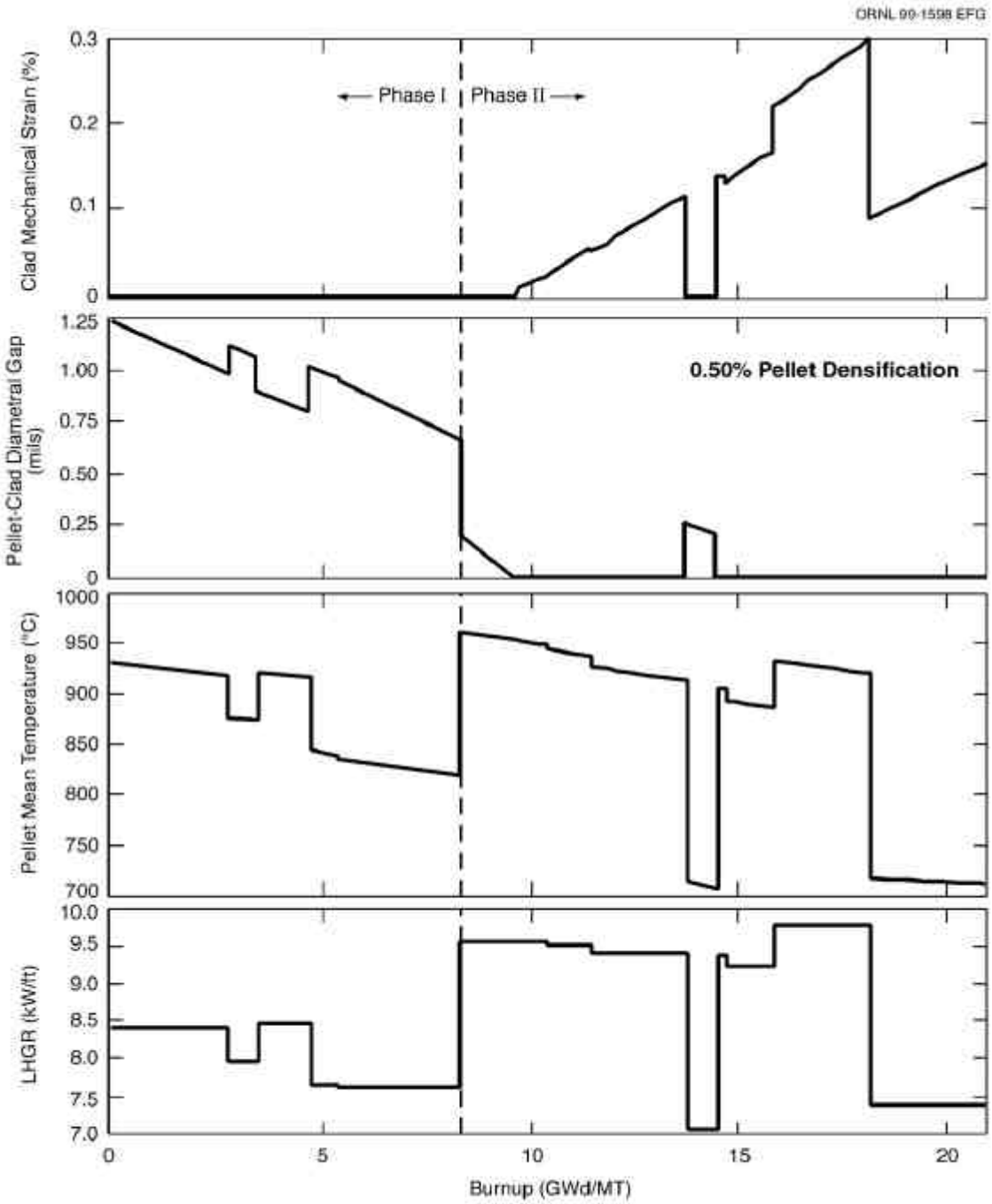

Figure 3.6. Conservative results for capsules 2 and 9 based upon maximum initial gaps and 0.50 percent pellet densification.

TABLE 3.1
Results of CARTS Calculations for Capsules 2 and 9 Just Prior to End of Phase II

Calculation classification	Initial Gap	Assumed pellet densification	Temperatures °C				Diametral gap (mil)		Pellet-clad contact during Phase II
			Pellet centerline	Pellet mean	Clad wall	Capsule wall	Pellet-to-clad	Clad-to-capsule	
Best-estimate	Maximum	0.5%	868	621	320	107	0.28	3.06	Never
		zero	836	595	320	107	0.14	3.06	First in Cycle 119B; relaxed during 120A
	Minimum	0.5%	767	537	280	107	0.08	2.14	First in Cycle 119A (3); relaxed during 120A
		zero	731	508	272	107	0.00	2.00	Continuous except during Cycle 119A (1)
Conservative	Maximum	0.5%	998	711	356	112	0.00	2.54	Continuous except during Cycle 119A (1)
		zero	982	698	345	112	0.00	2.28	Continuous
	Minimum	0.5%	914	643	293	112	0.00	1.16	Continuous
		zero	896	628	281	112	0.00	0.90	Continuous

3.6 The Capsules in the Hot Cell

The intermediate-withdrawal capsules were introduced into the ORNL hot cell in late October 1999, about five weeks after their removal from the ATR. The MOCUP protocol (coordinating calculations by MCNP and ORIGEN) was applied at INEEL to predict isotopic inventories [Ref. 14]. During the period from mid-October to end November, these results show that the pellet stack decay power decreased from 4.4 to 2.7 watts (0.0088 to 0.0054 kW/ft).

The Capsule-9 surface temperature was measured as 53.2°C (127.6°F) at a time when the decay heat was 3.42 watts. At this temperature, the thermal strain in the capsule wall is 0.06 percent. There is no fuel pin – capsule contact, and thus there is no capsule mechanical strain.

For the hot-cell calculations, heat transfer from the outer capsule surface is represented as convection to the hot-cell atmosphere, where the ambient temperature was measured as 30.2°C (86.4°F) at the time when the Capsule-9 surface temperature was taken. Based on these known values for decay heat and hot-cell atmosphere temperature, and defining the heat-transfer area as the portion of the capsule outer wall directly over the six-inch pellet stack, the associated surface heat-transfer coefficient is 26.36 W/m^2-C (4.64 Btu/hr-ft^2-°F). From similar measurements, the surface heat-transfer coefficient for Capsule 2 was found to be 27.82 W/m^2-C (4.90 Btu/hr-ft^2-°F). These are about three times the value that would be expected for natural convection to stagnant air, but are considered reasonable since there is some forced air flow through the hot cell. These are also very close to the value of 26.69 W/m^2-C (4.70 Btu/hr-ft^2-°F) reported previously for the early-withdrawal capsules.

The CARTS predictions for the capsule conditions at the expected time of opening are based on a decay power of 2.0 watts (0.0040 kW/ft), which corresponds to mid-January 2000. By the end of February, the predicted decay power was reduced to about 1.4 watts (0.0028 kW/ft).

Table 3.2 presents the results of the eight CARTS calculations for conditions in the intermediate-withdrawal capsules in the hot cell with decay heats corresponding to mid-January 2000. The final column of Table 3.2 indicates the predicted internal pressure within the fuel pins.

TABLE 3.2

Carts Results for Capsules 2 and 9 Under Hot Cell Conditions

Calculation classification	Initial Gap	Assumed pellet densification	Temperatures °C				Diametral gap (mil)		Fuel pin internal pressure psia
			Pellet centerline	Pellet mean	Clad wall	Capsule wall	Pellet-to-clad	Clad-to-capsule	
Best-estimate	Maximum	0.5%	43.8	43.7	43.4	43.3	1.52	3.10	27.5
		zero	43.8	43.7	43.4	43.3	1.28	3.10	27.8
	Minimum	0.5%	43.7	43.7	43.4	43.3	1.10	2.10	27.2
		zero	43.7	43.6	43.4	43.3	0.78	2.10	27.7
Conservative	Maximum	0.5%	44.0	43.9	43.5	43.3	1.00	3.10	63.0
		zero	43.9	43.8	43.5	43.3	0.68	3.10	64.1
	Minimum	0.5%	43.7	43.7	43.4	43.3	0.36	2.10	64.7
		zero	43.7	43.6	43.4	43.3	0.06	2.10	66.0

3.6.1 Best-Estimate Results

For the time of capsule opening, the pellet-to-clad diametral gaps within the fuel pins are predicted to lie in the range from 0.78 to 1.52 mils. These are best estimates and within this range, the different gaps associated with the fifteen individual pellets are determined by the extent of pellet densification (zero to 0.5 percent) and each pellet's initial cold diametral gap, which the design tolerances allow to lie between 2.0 and 3.5 mils. The pressure within the fuel pins (based on the pellet-clad annular gap volume plus the gas plenum volume associated with a nominal six-inch pellet stack length) is predicted to be about 27.5 psia (12.9 psig). This result is obtained by use of an assumed fission gas (krypton and xenon) release from the fuel matrix of 1.2 percent, which corresponds to previous experience with MOX fuels in Europe.

The diametral gap between the outer surface of the Zircaloy clad and the inner surface of the stainless steel capsule is calculated by CARTS to lie in the range between 2.1 and 3.1 mils. This one-mil range strictly follows from the design tolerances, which permit the cold clad-to-capsule initial diametral gap to vary between 2.0 and 3.0 mils. It is interesting to note that the predicted gaps are slightly larger than the gaps associated with the initial cold dimensions. This is because the clad and capsule wall are at very nearly the same temperature (about 43.3°C) in the hot cell, and the coefficient of expansion for steel is about three times larger than that of Zircaloy. Thus, with temperatures higher than when the cold dimensions were measured, differential thermal expansion has increased the separation between the clad and the capsule. The thermal strains for the capsule and fuel pin are 0.04 percent and 0.01 percent, respectively.

3.6.2 Conservative Results

The capsule conditions in the hot cell have also been predicted by a set of conservative calculations. Here the gas gap thermal conductance model and parameters such as material thermal conductivities and fluid/capsule heat transfer coefficients were chosen in directions relative to the best-estimate values that tend to increase the calculated pellet temperature and, hence, the predicted thermal expansion and extent of irradiation-induced swelling. The capsule powers during reactor operation and in the hot cell are, however, the same as used in the best-estimate calculations. Accordingly, the capsule surface temperature in mid-January 2000 is predicted to be 43.3°C (110°F), with an associated capsule wall thermal strain of 0.04 percent, the same as predicted by the best-estimate calculations.

Even with the conservative assumptions for gap conductance, material conductivities, and irradiation-induced swelling, pellet-clad contact is not predicted in the hot cell. The closest approach is for the case of minimum initial gap combined with the assumption of zero pellet densification during irradiation. For this case (last entry in Table 3.2), the pellet-clad diametral gap in the hot cell is predicted as 0.06 mils. With a predicted clad temperature of 43.4°C, the thermal (and total) clad strain is predicted to be just 0.01 percent.

Although the pellet-to-clad diametral gaps under hot-cell conditions are smaller with the

conservative assumptions, the results do not differ significantly from the best-estimate values. The conservatively predicted pellet-to-clad diametral gaps lie in the range from 0.06 to 1.00 mils.

The internal fuel pin pressure is predicted to lie between 63.0 and 66.0 psia (48.3 and 51.3 psig), which corresponds to a (conservative) 4.4% release from the fuel matrix. The calculated clad-to-capsule gaps are not affected by the imposition of conservative bias with respect to pellet behavior and lie in the same range as for the best-estimate cases.

3.7 Summary and Conclusions

Based upon the swelling algorithms developed from extensive experience with UO_2 fuel, and the European experience demonstrating that these algorithms can also be applied to MOX, the CARTS code has been developed to predict the effects of pellet irradiation in the ATR MOX fuel irradiations. In considering the results calculated by CARTS, it is important to remember that application of the existing algorithms for irradiation-induced pellet swelling has been justified based upon experience with the MOX fuel produced in Europe [Ref. 5]. In a sense, the PIE results provide a measure as to how closely the pellets irradiated during the Average-Power Test replicate the behavior represented by the European data.

For the two intermediate-withdrawal capsules with 20.9 GWd/MT burnups, the best-estimate CARTS code predictions are that the 15 pellets in each fuel pin will exhibit, under hot-cell conditions, individual pellet-to-clad diametral gaps ranging from 0.78 to 1.52 mils. When conservative assumptions regarding heat-transfer parameters are imposed, the calculated gaps are smaller, but residual pellet-clad contact in the hot cell is still not expected.

The diametral gap between the fuel pin and the capsule is expected to be between 2.1 and 3.1 mils, which is slightly larger than the range for the initial cold capsule assemblies. Thus, no difficulty should be encountered in removing the fuel pins from the capsules.

The gas pressure within the fuel pins is predicted to be about 27.5 psia (12.9 psig). The LHGRs experienced during this test irradiation are higher than those normally encountered in the literature, which tends to increase the extent of fission gas release from the fuel matrix. Allowance for the effects of these higher LHGRs has been included in the pressure calculation. However, the predicted pressures correspond to a nominal pellet stack length of six inches. The calculated pressure will be proportionally less for a shorter pellet stack (and the increased volume associated with the longer gas plenum).

Another consideration with respect to the calculated pressures is that these fuel pins have experienced nineteen thermal cycles. Thus, the release of fission gas from the fuel matrix may have been increased due to a greater-than-normal pellet thermal cracking. The pressure calculations reported here have utilized an assumed gas release of 1.2 percent, based upon the available literature for MOX applications.

Although pellet-clad contact is not expected to persist at the lower component temperatures when the fuel pins are opened in the hot cell, the CARTS code results indicate that pellet-clad contact was initiated at some point during Phase II of the irradiation. (The only best-estimate calculation for which pellet-clad contact was never predicted was for the pellets with maximum initial gaps combined with an assumed 0.50 percent densification during irradiation.) The largest of the mechanical strains predicted by the best-estimate calculations to have occurred during irradiation is 0.15 percent, which is insufficient to cause yielding of the clad Zircaloy. Thus, no residual mechanical strain is predicted for the clad in the hot cells.

3.8 Retrospective on CARTS Predictions

The prior Sections (3.1 through 3.7) of this Chapter were prepared before the current (intermediate-withdrawal) PIE was completed. The following Chapters provide the information obtained during this PIE. It is of interest to pause at this point and reflect as to how well the predictions match the findings.

The best agreement is obtained with the best estimate results, utilizing a 0.5 percent assumed densification. The predicted range of pellet-to-clad diametral gaps (1.10 to 1.52 mils as listed in Table 3.2) is too small, however, when compared with the observed range of 2.46 to 3.34 mils. This larger gapwidth between pellet and clad is attributed to a combination of unanticipated outward clad creep and greater-than-expected fuel densification. The evidence for both of these effects is discussed in Chapter 6.

The CARTS code has been modified to represent the observed clad creep and the input with respect to fuel densification has been upgraded to reflect the observed densification history as derived from the current PIE. With these changes, the code calculates the observed gaps, and no pellet-clad contact is predicted to have occurred during the irradiation. A new set of calculations has been performed to predict the gap and other dimensions for the capsules withdrawn at 30 GWd/MT, and that PIE will serve as the test for the new models. Thus, the progressive series of PIEs with the intervening code upgrades and input adjustments provide a means to obtain improved accuracy when the higher burnups are reached.

4. PIE METROLOGY OF CAPSULES 2 AND 9

Table 4.1 details the metrology items that have been selected for PIE effort. Note that these items form a subset of the total PIE effort. The capsules made available for the intermediate PIE are Capsule 2 (fuel prepared without gallium removal) and Capsule 9 (fuel prepared with gallium removal).

TABLE 4.1
Metrology Items

No.	Examination	Comments
1	Capsule photo visual	Containment integrity is major interest.
2	Capsule temperature measurement	Compare measured temperatures with predictions.
3	Capsule dimensional inspection	Containment integrity is major interest.
4	Capsule gamma scan	Determine gross internal state of capsule and fuel pin.
5	Fission gas sampling	The fission gas pressure and ^{85}Kr content of both the containment and the fuel pin will be analyzed.
Remove fuel pin from capsule		
6	Fuel pin photo visual	First assessment of clad integrity. (An additional gamma scan may be performed if the situation warrants.)
7	Fuel pin dimensional inspection	Second assessment of clad integrity.

Note that the capsule and fuel pin identification numbers are not the same; Table 4.2 details the relationship between the two and identifies the status with respect to gallium removal treatment.

4.1 Capsule Photo Visual Inspection

The first portion of the PIE effort was to visually examine the capsule surfaces at low magnification. Both capsules appeared to be clean and bright with no sign of corrosion or damage. The black lines near the welding border are the heat-affected zone and are unrelated to the irradiation. In general, the stainless steel containment survived the irradiation as expected and these capsules appear no differently than the capsules removed at 8 GWd/MT. Photographs of Capsules 2 and 9 are shown in Figures 4.1 through 4.6 for a variety of views. The two capsules appear identical except for the identification marks

TABLE 4.2
Capsule and Fuel Pin Numbers

Capsule Number	Fuel Pin Number	Fuel Batch	Gallium Treatment	Exposure (GWD/MT)	PIE Status
1	2	A	None	8	Complete - clad tests pending
2	5	A	None	21	Subject of this report - clad tests pending
3	6	A	None	30	ORNL Hot Cell (9/18/00)
4	7	A	None	In reactor	
5	8	A	None	In reactor	
6	9	A	None	In reactor	
7	10	A	None	Unirradiated archive	
8	11	B	Thermal (TIGR)	8	Complete - clad tests pending
9	12	B	Thermal (TIGR)	21	Subject of this report - clad tests pending
10	13	B	Thermal (TIGR)	30	ORNL Hot Cell (9/18/00)
11	14	B	Thermal (TIGR)	Unirradiated archive	
12	15	B	Thermal (TIGR)	In reactor	
13	16	B	Thermal (TIGR)	In reactor	

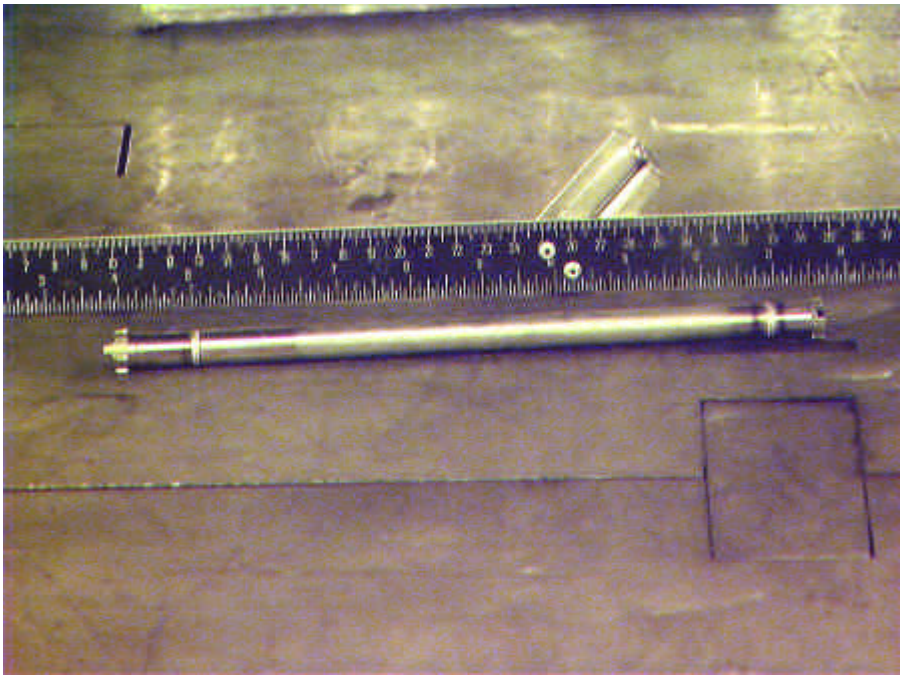

Figure 4.1 Side view of Capsule 2. [R2-side-front.JPG]

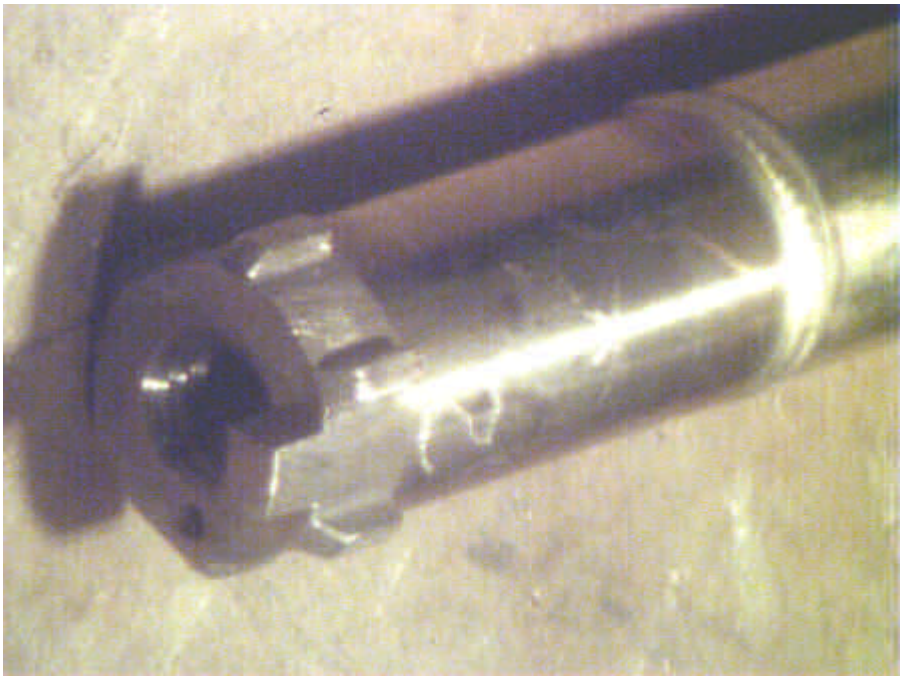

Figure 4.2 Top view of Capsule 2. [R2-top-high.JPG]

Figure 4.3 Bottom view of Capsule 2. [R2-bot-high.JPG]

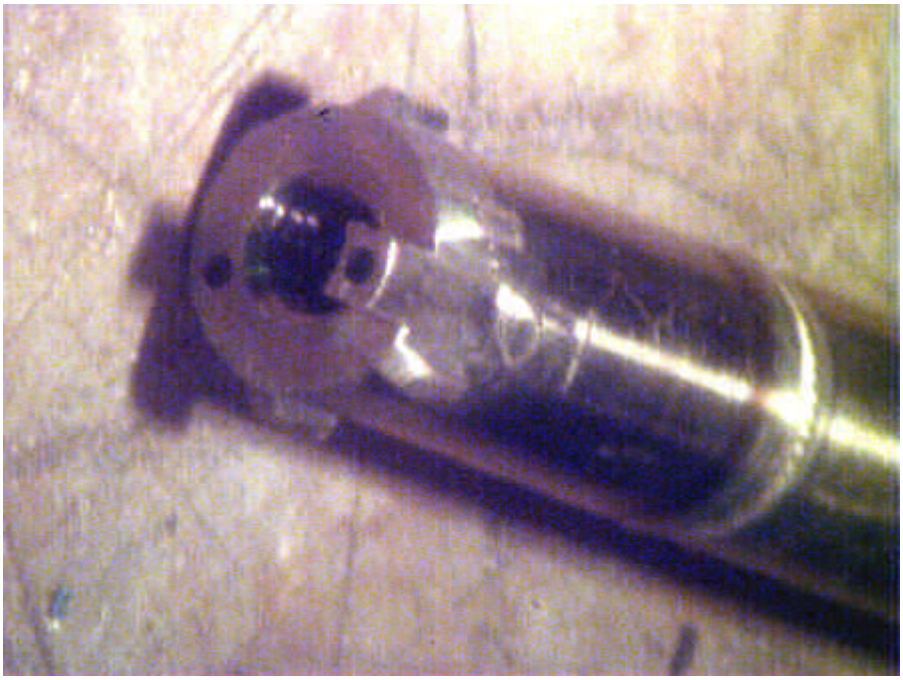

Figure 4.4 Top view of Capsule 9. [R9-top-high.JPG]

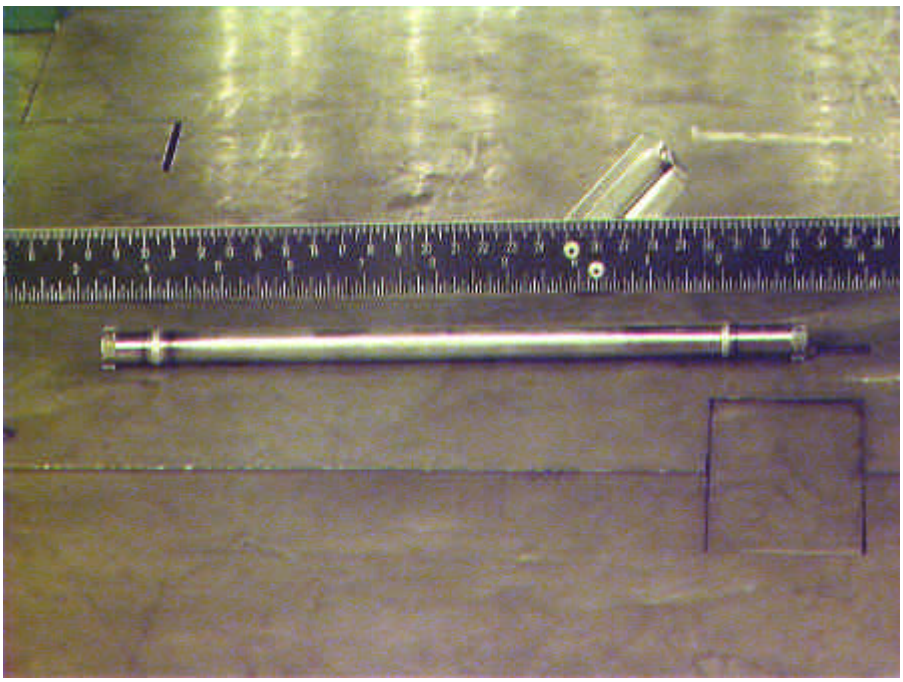

Figure 4.5 Side view of Capsule 9. [R9-side-front.JPG]

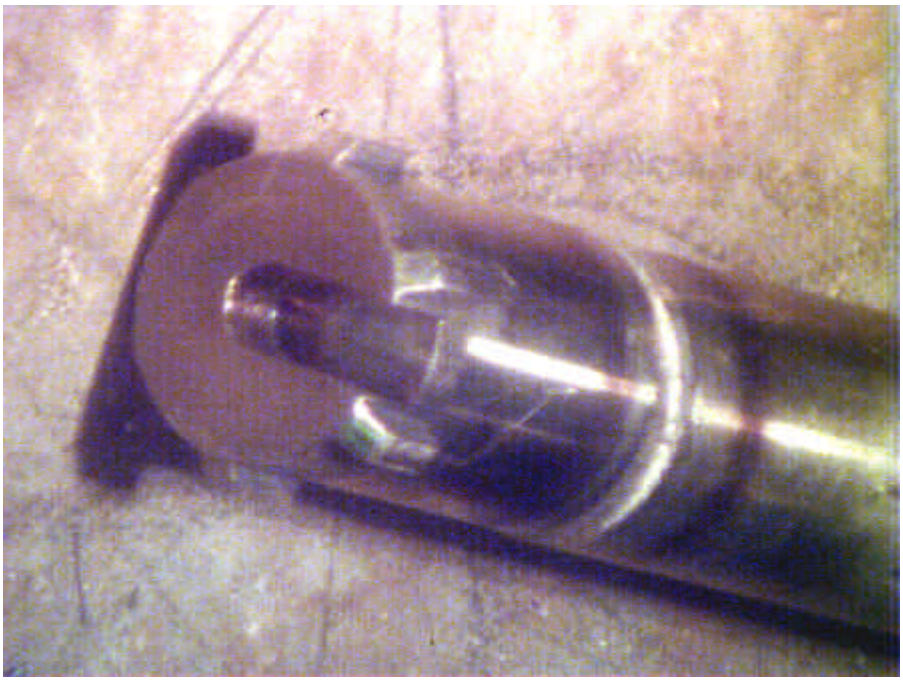

Figure 4.6 Bottom view of Capsule 9. [R9-bot-high.JPG]

4.2 Capsule Temperature Measurements

The temperature measurements and their locations as taken on Capsules 2 and 9 are shown in Table 4.3. A photo of a capsule undergoing a measurement is shown in Fig. 4.7. The apparatus consists of a Type C thermocouple held to the capsule by a modified hose clamp.

TABLE 4.3 **Capsules 2 and 9 Temperature Measurements**	
MOX Capsule 2	
Measurements taken on 10/27/99 from 0930 to 1345	
Top Weld	101.4°F (38.7°C)
Mid Point	125.4°F (51.8°C)
Bottom Weld	112.4°F (44.5°C)
Average	*113.1°F (45.0°C)*
Cell Ambient	86.0°F (30°C)
MOX Capsule 9	
Measurements taken on 10/26/99 from 0910 to 1230	
Top Weld	102.4°F (39.0°C)
Mid Point	127.6°F (53.2°C)
Bottom Weld	108.6°F (42.5°C)
Average	*112.8°F (44.9°C)*
Cell Ambient	86.4°F (30.2°C)

Notes :
Temperature measurements were taken 10" from the hot cell table top and allowed to stabilize for 45 minutes. Fahrenheit and Centigrade values were determined by switching between instrument readouts, not mathematical conversion. These values are used to set the capsule surface heat transfer coefficient, as discussed in Section 3.6.

4.3 Capsule Dimensional Inspection

The results of the stainless steel capsule dimensional inspections are shown in Table 4.4. Within 0.001 inches, there were no indications of bowing, out of roundness, or other distortions. Measurements for bowing and distortions were carried out between the capsule welds. Only a

slight difference between pre- and post-irradiation diametrical values was noted, less than 0.001 inches, which is attributable to thermal expansion due to the somewhat higher measurement temperature in the hot cell. The lengths of the capsules were found to agree with the preirradiation values, within 0.007 inches. Figure 4.8 details the measurement method for radial dimensions.

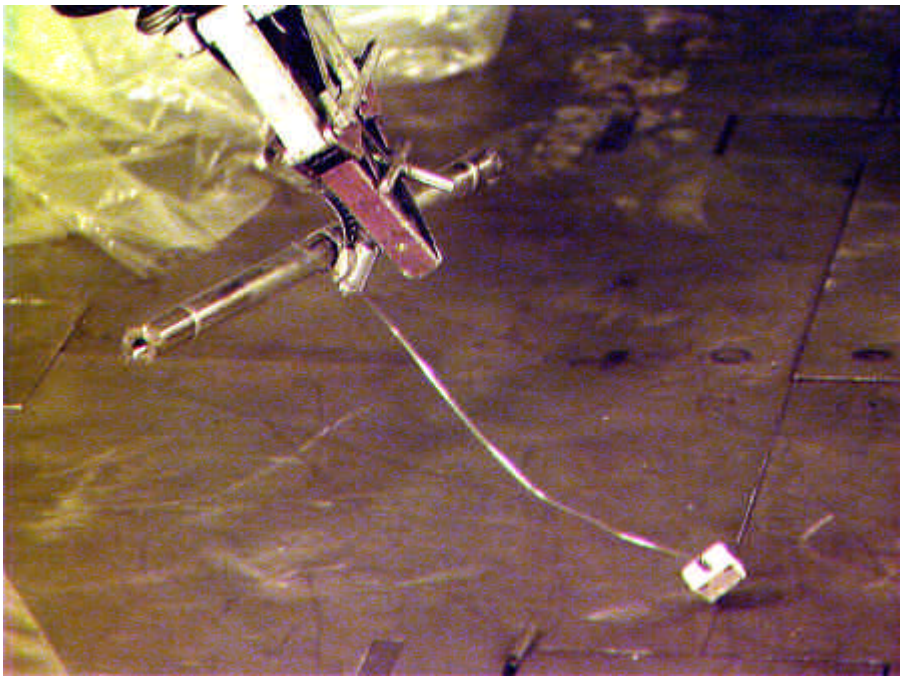

Figure 4.7 Free air temperature measurement on Capsule 9. [R9-temprt.JPG]

TABLE 4.4 Capsule Measurements			
Axial Location	**Diameter Measurement (in) (±0.0005 in)**		**Preirradiation Value (in)**
	0°	**90°**	
Capsule 2			
3.9" from capsule top	0.4653	0.4651	0.4643 to 0.4649
Center of capsule	0.4656	0.4653	
6.7" from capsule top	0.4654	0.4652	
Capsule 9			
4.0" from capsule top	0.4651	0.4650	0.4643 to 0.4649
Center of capsule	0.4652	0.4648	
6.5" from capsule top	0.4653	0.4652	
Length (in) (±0.005 in)			
Capsule 2	9.585		9.578 after welding (9.59 before welding)
Capsule 9	9.581		9.576 after welding (9.59 before welding)
Mass (g) (±0.1 g)			
Capsule 2	192.3		Not given
Capsule 9	192.8		Not given

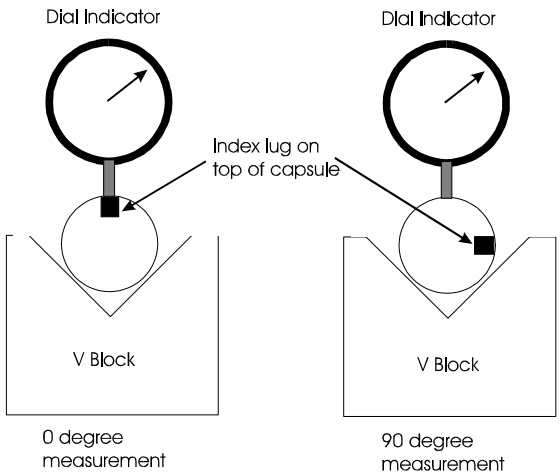

Figure 4.8 Schematic of diameter measurement. [vblock.wpg]

4.4 Capsule Gamma Scans

Both Capsules 2 and 9 were raster scanned to obtain a two dimensional view of the capsule internal structure. These scans were composed of just over 5000 points and were taken with a 1/16" diameter collimator in two energy ranges. The range 400 to 700 KeV was employed to broadly cover the fission products while the range 800 to 1575 keV was used to broadly cover the activation products. These two energy ranges were selected because they show the most details of interest for a general view.

An effort was made to detect the free ^{85}Kr inventory in the plenum region of the fuel pin contained in Capsule 9 using the gamma scanner, but no ^{85}Kr could be observed due to the high background from other isotopes.

In addition, both capsules underwent an axial line scan (400 points) along their length using the same collimator as was used in the two-dimensional scans. Results from these two energy ranges are presented in the following sections. Overall, the capsules appeared to be intact with no unusual structure or abnormalities.

It should be noted that the resolution of the gamma scanner has been improved (from that used for the 8 GWd/MT PIE) by increasing the length of the collimator and reducing the distance between the capsule and the collimator. These improvements have resulted in significantly better resolution as can be seen by the squareness of the edges on the pellets in Figures 4.9 (Capsule 2) and 4.13 (Capsule 9).

4.4.1 Capsule 2 Gamma Scan

Figure 4.9 shows the result of the 400 to 700 KeV raster scan for Capsule 2. When compared to the schematic above it, one can make out the stainless steel end caps, the fuel pin end caps, and very clearly, the fuel pellet stack. The pedestal on the lower fuel pin plug is vaguely outlined as well as is the capsule boundary (the capsule bottom is to the left, the top to the right). Figure 4.10 shows the same scan in the 800 to 1575 keV energy range. This higher energy range outlines the stainless steel components to a greater degree.

The schematic at the top of Figure 4.9 and the following Figures is based on the nominal capsule design. This design has a fuel stack length of 6.0 inches. The drawings are scaled so that the stack height in both the schematic and the data match. In reality, the fuel stack length is slightly less than 6.0 inches (about 5.8 inches), so that a small misalignment between the components of the two is apparent to the careful reader in some cases. The fuel stack had a tolerance of +0.0, -0.2 inches, so this is normal. Actual dimensions are listed in Table 2.1.

Figure 4.11 shows an axial line scan along the capsule in the 400 to 700 keV energy range. Again, the elements of the capsule are clearly indicated. The fuel pellet stack appears to be about 5.8 inches long. Note the burnup peaking at the ends of the fuel stack and the signal dips indicating the dished ends of the 15 pellets.

Figure 4.12 shows an axial line scan in the energy range of 800-1575 KeV, which accents the stainless steel activation products. This figure shows the stainless steel capsule end caps and wall more clearly. The fuel can be seen because of the high energy fission product emitters such as ^{140}La.

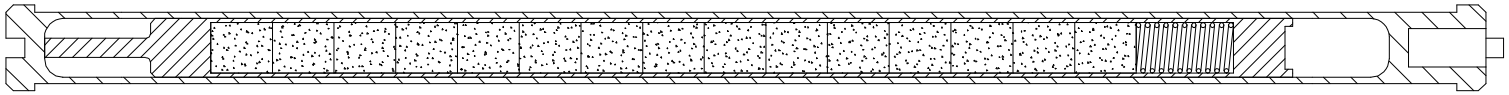

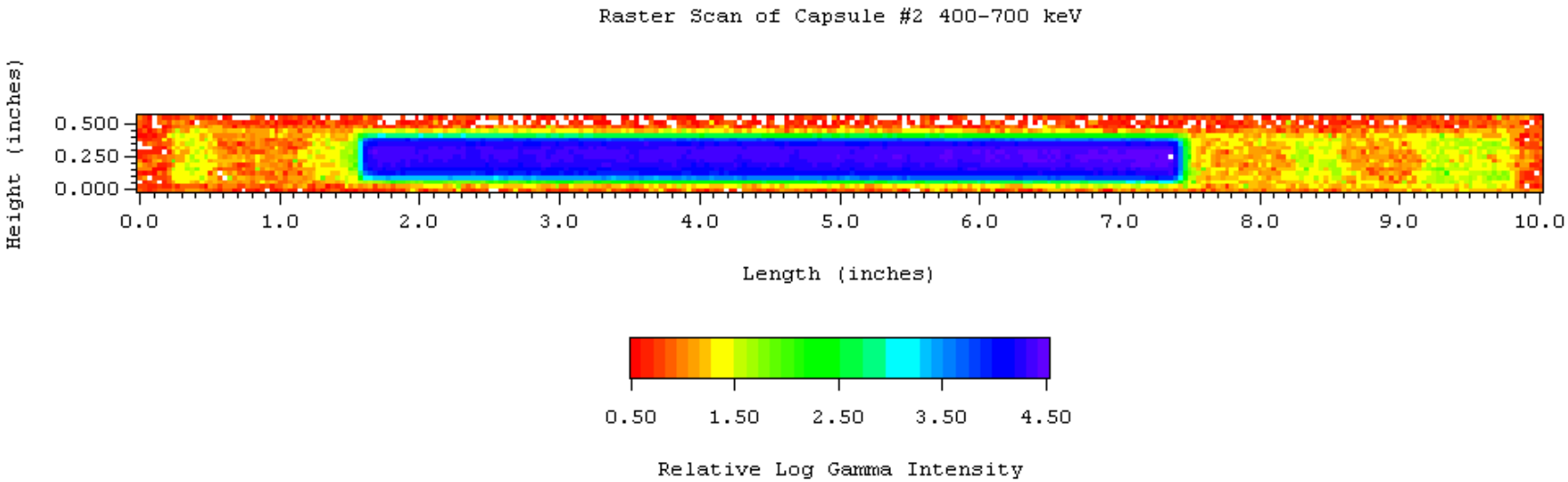

Figure 4.9 Capsule 2 mid energy gamma raster scan. [ras2.wpg]

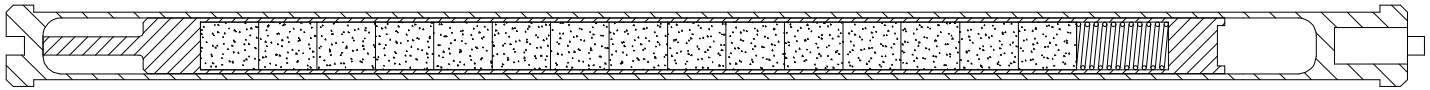

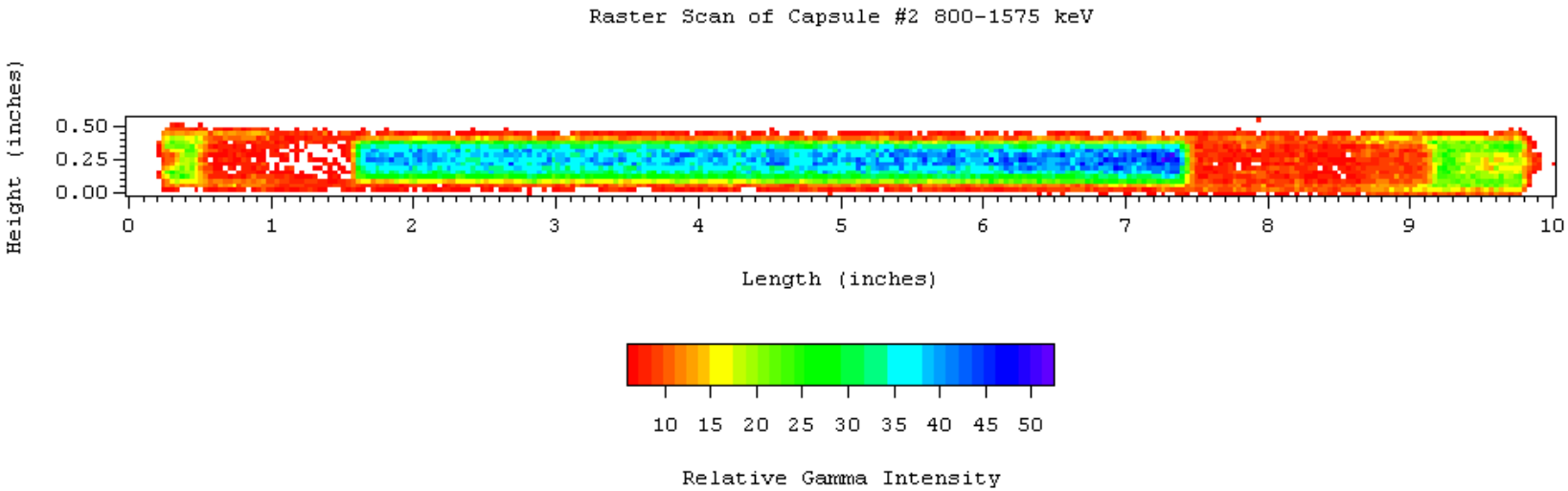

Figure 4.10 Capsule 2 high energy gamma raster scan. [ras2h.wpg]

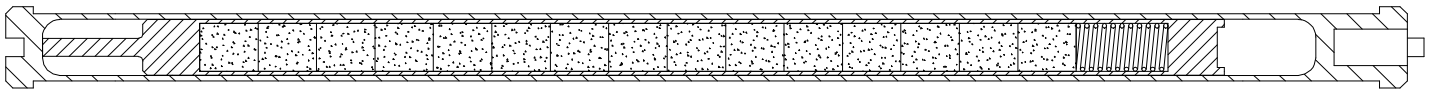

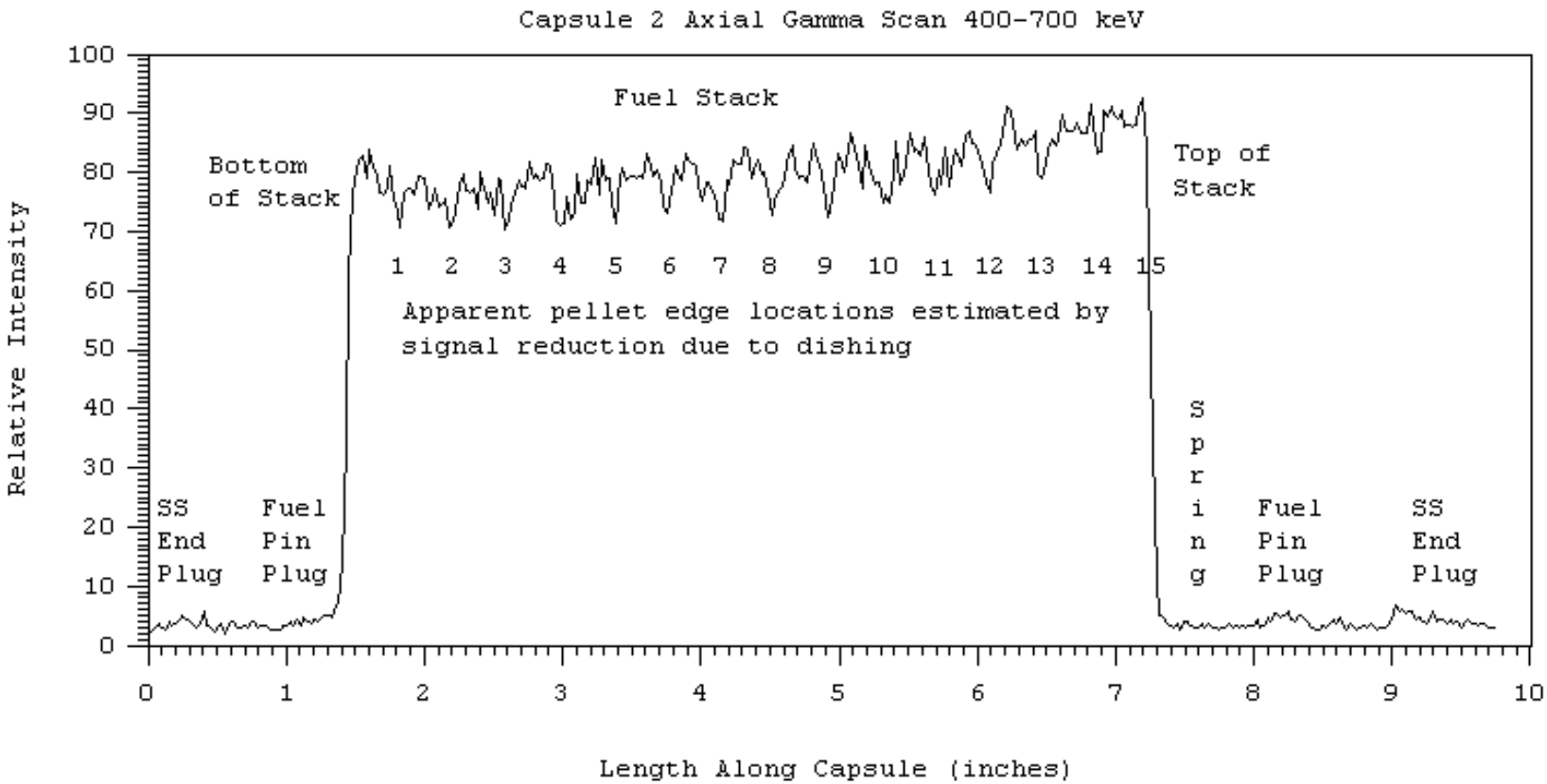

Figure 4.11 Capsule 2 mid energy gamma line scan. [ls2.wpg]

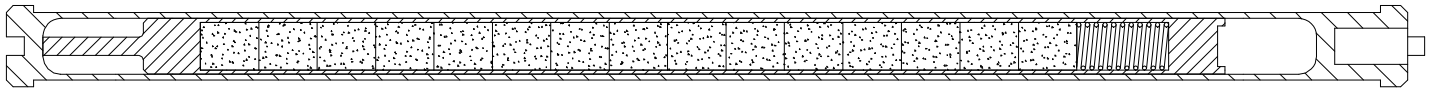

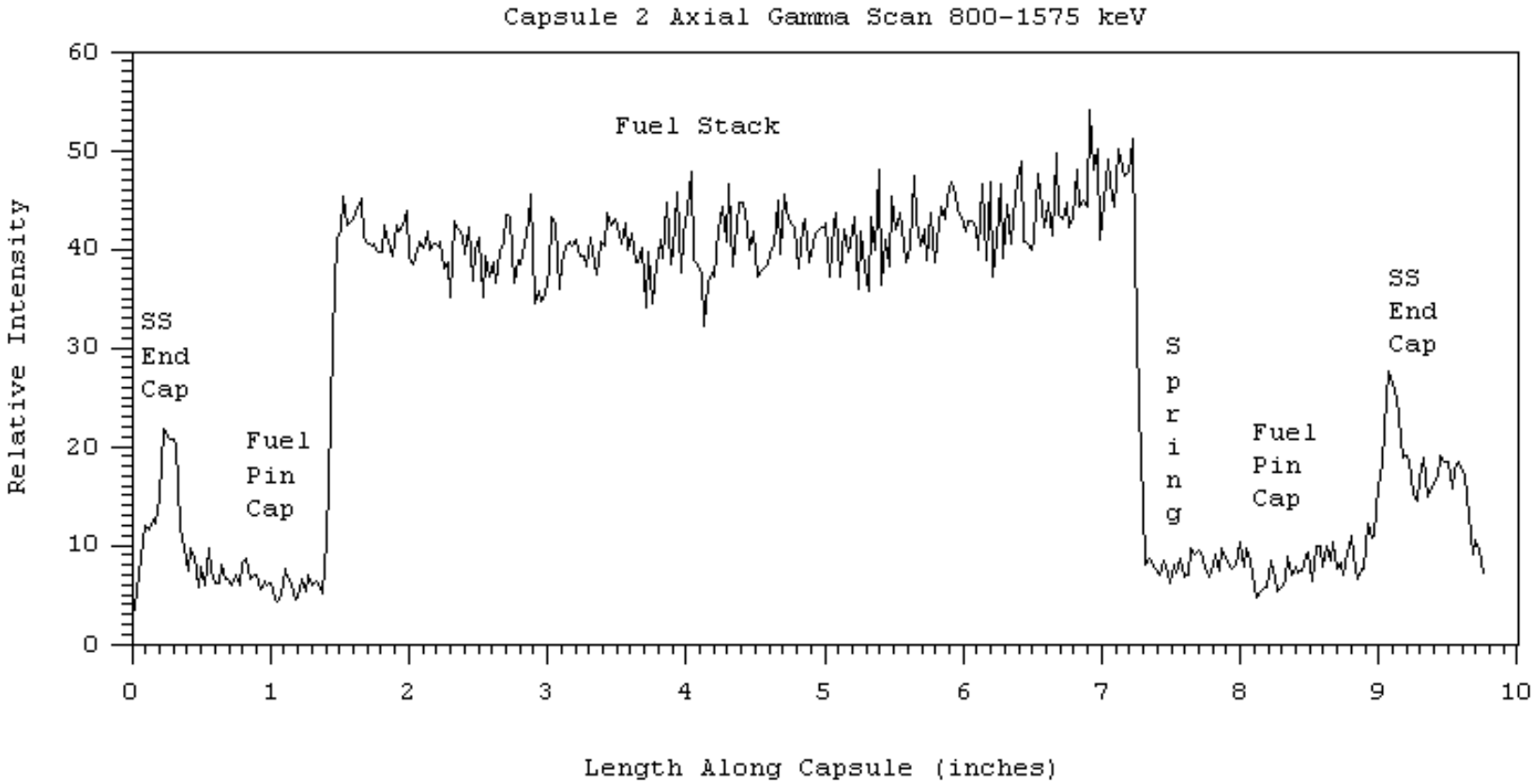

Figure 4.12 Capsule 2 high energy gamma line scan. [ls2h.wpg]

Overall, the capsule showed no structural problems. All components were observed to be in their proper locations and the fuel pellet stack does not appear to have swelled significantly.

4.4.2 Capsule 9 Gamma Scan

Figure 4.13 shows the results of the 400 to 700 keV raster scan for Capsule 9. As before, one can make out the stainless steel end caps, the fuel pin end caps, and the fuel pellet stack. Figure 4.14 shows the same scan in the 800 to 1575 energy range. No inconsistences or abnormalities in internal component locations were noted.

The relative intensities between the two capsules are different because they were scanned approximately two weeks apart. The scanning took place only a few weeks after the end of irradiation, so the contributions of the rapidly decaying short lived isotopes were still important. Thus, the recorded gamma intensity of Capsule 9 is lower because of the extra two weeks of decay time.

Figure 4.15 shows an axial line scan along Capsule 9 in the 400 to 700 keV energy range. Again, the elements of the capsule are visible. The fuel stack appears to be approximately 5.8 inches long, but in this case the pellet dishing is not clearly discernable. Apparently, the stronger presence of the shorter lived isotopes helped define the pellet edges in the scan of Capsule 2. Note the burnup peaking at the ends of the fuel stack, as was seen in the axial scan of Capsule 2.

Figure 4.16 shows an axial line scan in the energy range of 800-1575 KeV, which accents the stainless steel activation products.

Similar to Capsule 2, Capsule 9 appears to have no structural problems and all components were observed in their proper locations with no significant axial fuel swelling.

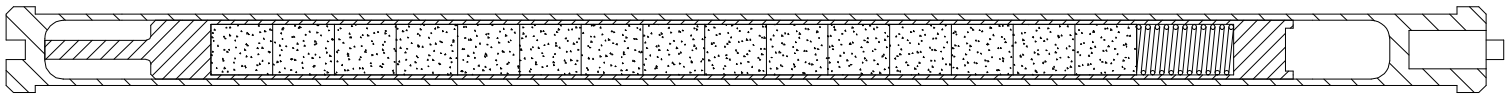

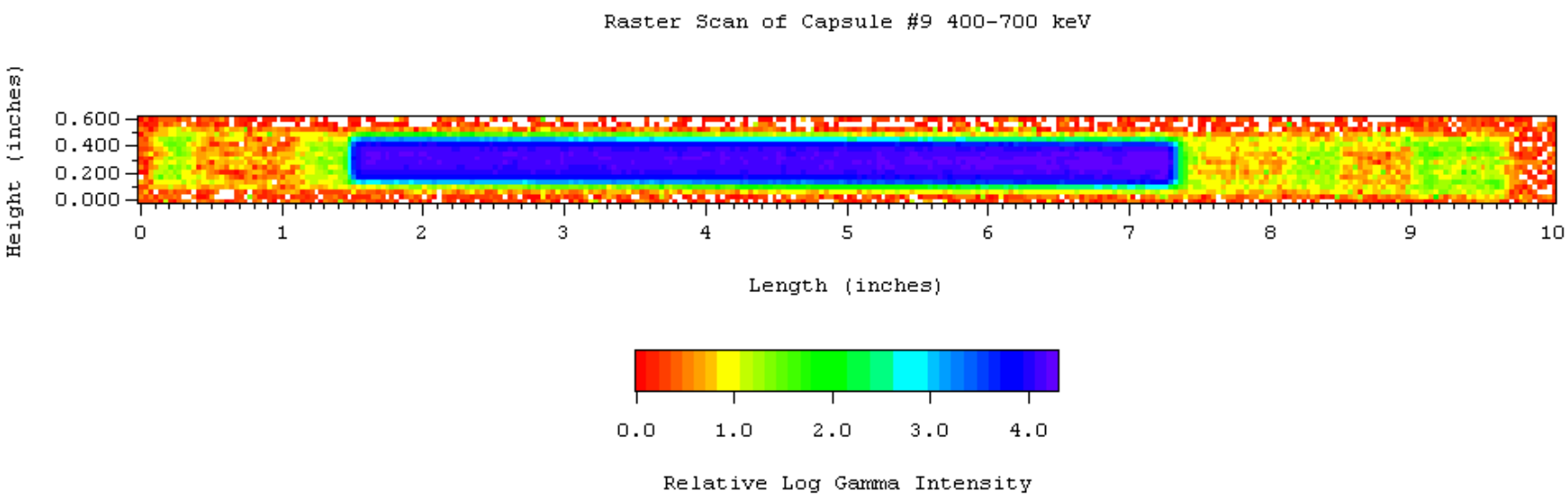

Figure 4.13 Capsule 9 mid energy gamma raster scan. [ras9.wpg]

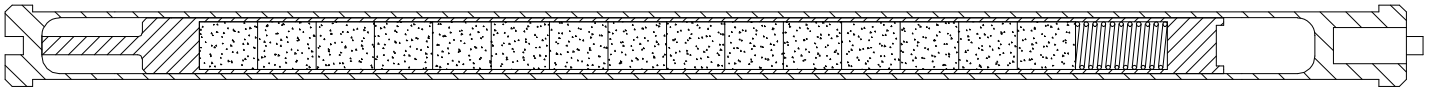

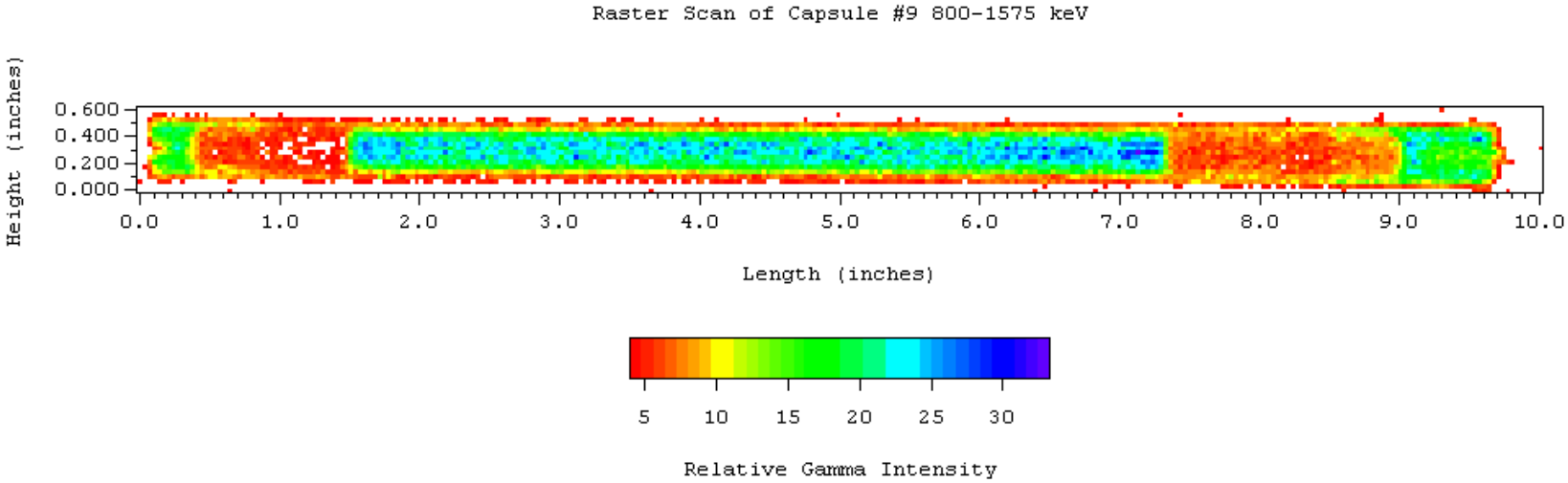

Figure 4.14 Capsule 9 high energy gamma raster scan. [ras9h.wpg]

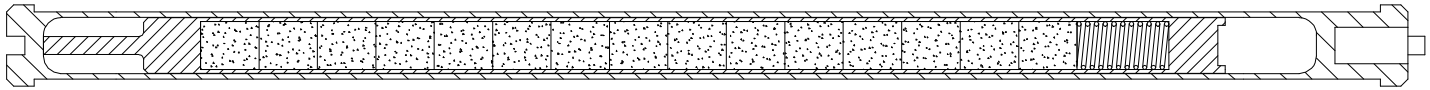

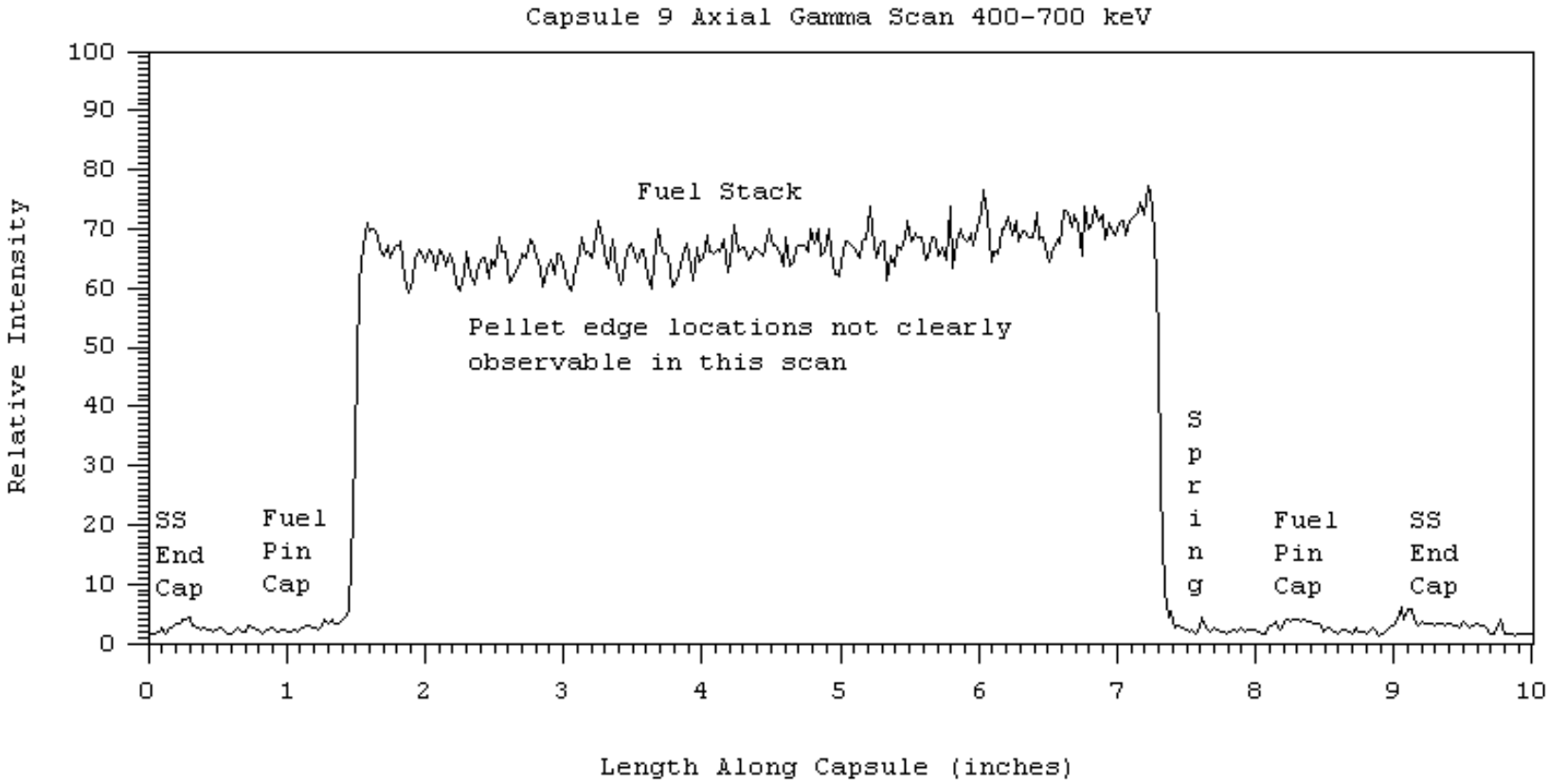

Figure 4.15 Capsule 9 mid energy gamma line scan. [ls9.wpg]

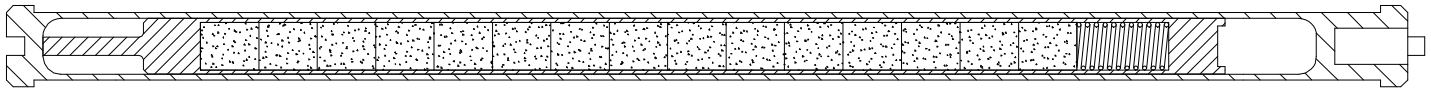

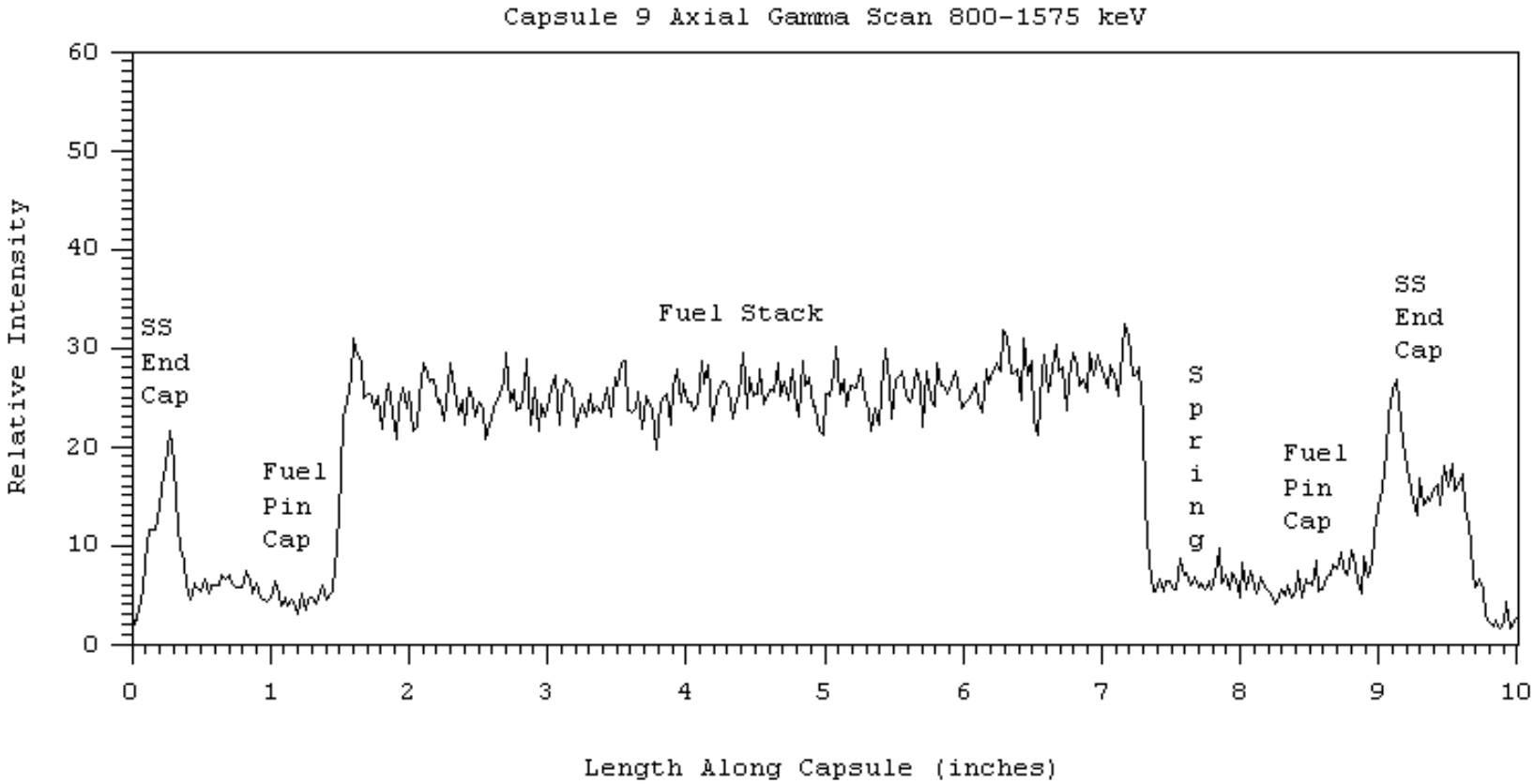

Figure 4.16 Capsule 9 high energy gamma line scan. [ls9h.wpg]

4.4.3 Gamma Scanner Data Collection Orientation

The gamma intensity data was collected with the alignment lug of the capsule facing the gamma scanner detector as shown in Figure 4.17.

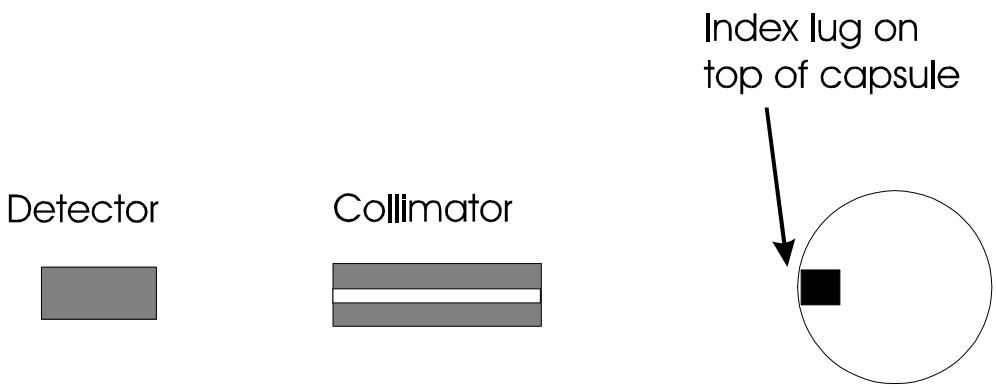

Figure 4.17 Orientation of the capsule and the gamma scanner collimator/detector. [gamdir.wpg]

4.5 Fission Gas Measurements

The fission gas pressure and ^{85}Kr content in both Capsules 2 and 9 and their associated fuel pins were measured by use of the MOX Fission Gas Pressure Measuring Apparatus. Details of this apparatus and its calibration are described in Ref. 16. Briefly, the apparatus functions by using a vacuum sealed drill-press like action to drill first through the trimmed top of the stainless steel capsule and then, after sampling the gas in the capsule upper plenum region, to continue drilling into the upper end cap of the contained fuel pin. The drilling stops as each barrier is penetrated to permit measurement of the gas pressure and sweeping of the released gases through a cold trap system to trap and determine the ^{85}Kr quantity. The heart of the apparatus is a ferrofluidic seal, which utilizes a novel magnetic fluid for rotary vacuum sealing and a stainless steel bellows for linear vacuum sealing. A diagram of the device is shown in Figure 4.18.

No anomalous fission gas release was observed in either capsule. The capsule pressures were subatmospheric, as expected since they were sealed at the elevation of INEEL, where the atmospheric pressure is about 12.5 psia. (The actual pressure in the capsule during welding could not be recorded.) The fuel pins were found to be sealed and the fission gas release was determined to be in the range of 1.5 to 2.0% (based on ^{85}Kr), with measured pressures equal to or slightly less than were predicted by the CARTS fuel performance calculation. No problems occurred with the apparatus. The details are summarized in Table 4.5.

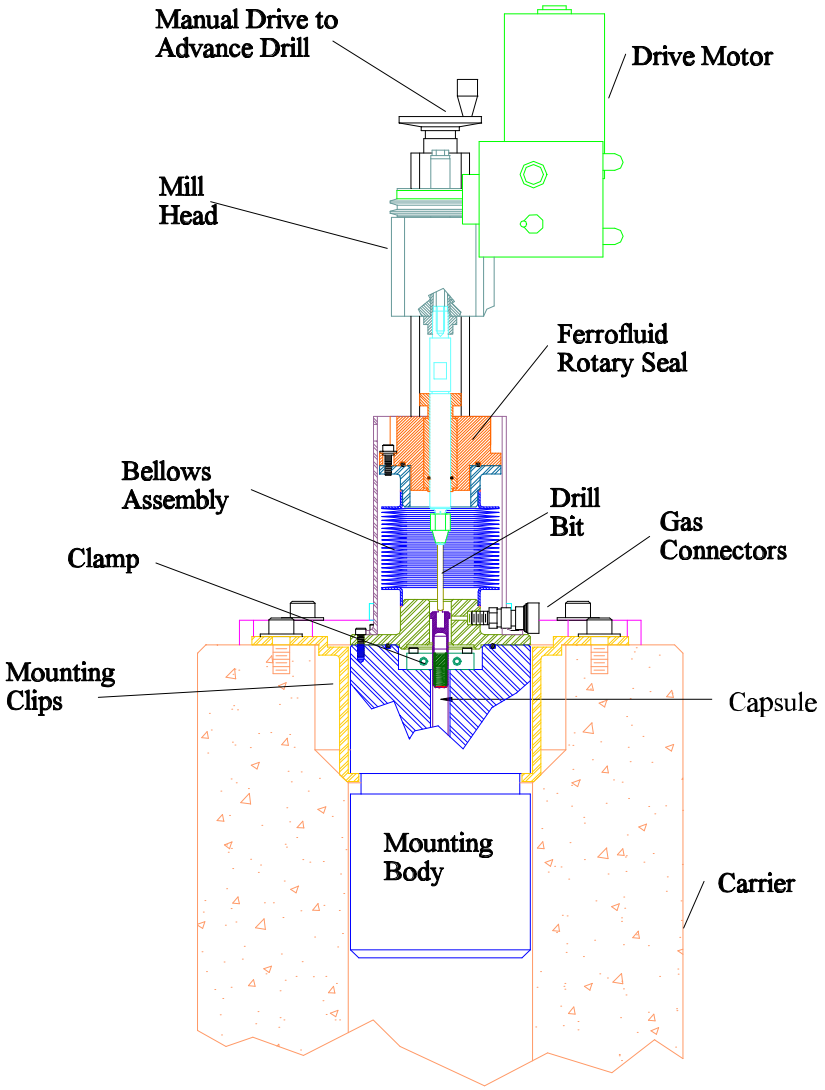

Figure 4.18 Cross sectional view of the Fission Gas Pressure Measuring Apparatus. [Drill Schematic 2.wpg]

TABLE 4.5
Fission Gas Measurements

Item	Best Estimate Free Volume[1] (cc)	Measured Pressure (psia)	Measured ^{85}Kr in Free Volume (mCi)	Best Estimate for Total ^{85}Kr Inventory[2] (mCi)	Model Predicted Pressure[3] (psia)	Release Fraction Based on ^{85}Kr Measurement
Capsule 2	2.477	10.1	0.00	0	N/A	N/A
Fuel Pin 5	1.197	23.8	4.38	303	27.5	0.0144
Capsule 9	2.477	10.0	0.00	0	N/A	N/A
Fuel Pin 12	1.225	27.5	5.86	300	27.5	0.0195

[1]Based on actual dimensional measurements and code predicted fuel swelling
[2]Based on ORIGEN calculations (Ref. 14)
[3]Based on CARTS calculations with an estimated release fraction of 0.012 and nominal fuel pellet stack length dimensions (Chapter 3)
Ambient temperature of 23°C
Measured values are approximately ±8% for pressure and ±6% for ^{85}Kr

4.6 Fuel Pin Photo Visual Inspections

Fuel Pin 5 was removed from Capsule 2 by cutting off the bottom of the capsule just above the weld. This operation also removed about ½ of the bottom pedestal of the fuel pin. After deburring the capsule body, the fuel pin was removed by grasping and pulling on the bottom pedestal. The pin slid out easily. After removal, the pin was photographed and measured. The exterior of Fuel Pin 5 was found to be in excellent condition.

No attempt was made to maintain the angular orientation of the fuel pin relative to the capsule index lug because the fuel pin is not locked within the capsule during irradiation. Photographs of the fuel pin are shown in Figures 4.19 through 4.21.

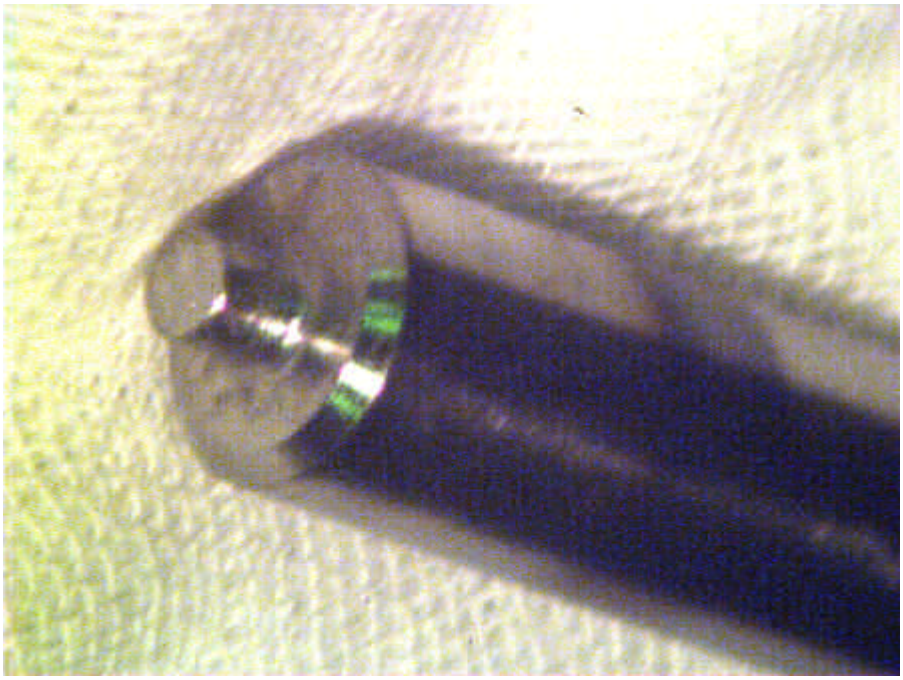

Figure 4.19 Bottom end of Fuel Pin 5. Note the shortened pedestal from the cutting operation. [P5-bottom.JPG]

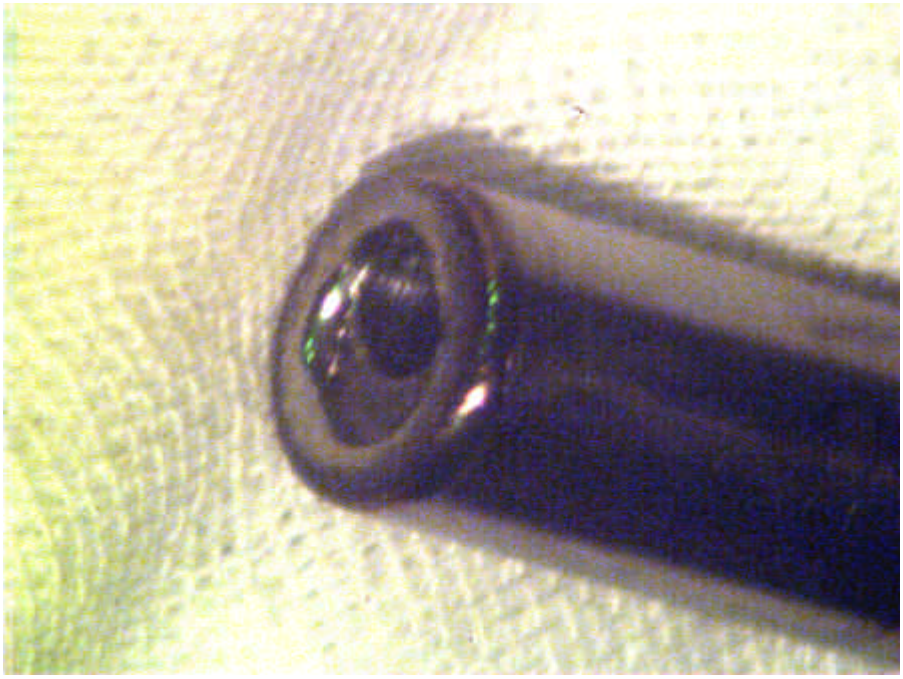

Figure 4.20 Top end of Fuel Pin 5. Note the hole from the fission gas pressure measurement. [P5-top.JPG]

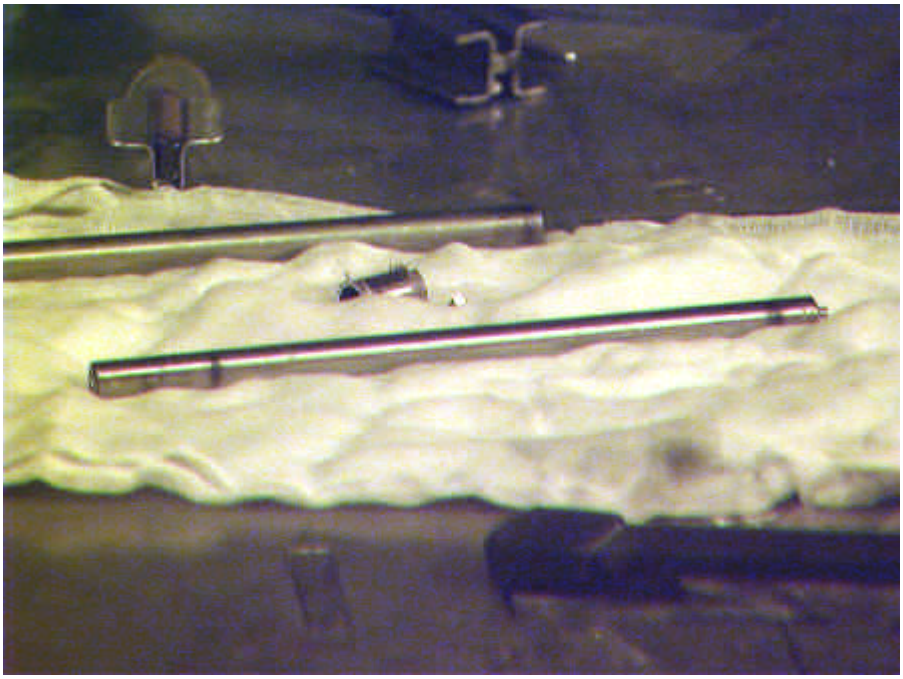

Figure 4.21 Side view of Fuel Pin 5. Note capsule components in background. [P5-side-front.JPG]

Fuel Pin 12 was removed from Capsule 9 in the same manner that Fuel Pin 5 was removed from Capsule 2. The exterior of Fuel Pin 12 was also found to be in excellent condition. Photographs of Fuel Pin 12 are shown in Figs. 4.22 through 4.24.

Figure 4.22 Bottom end of Fuel Pin 12. Note the shortened pedestal from the cutting operations. [P12-bottom.JPG]

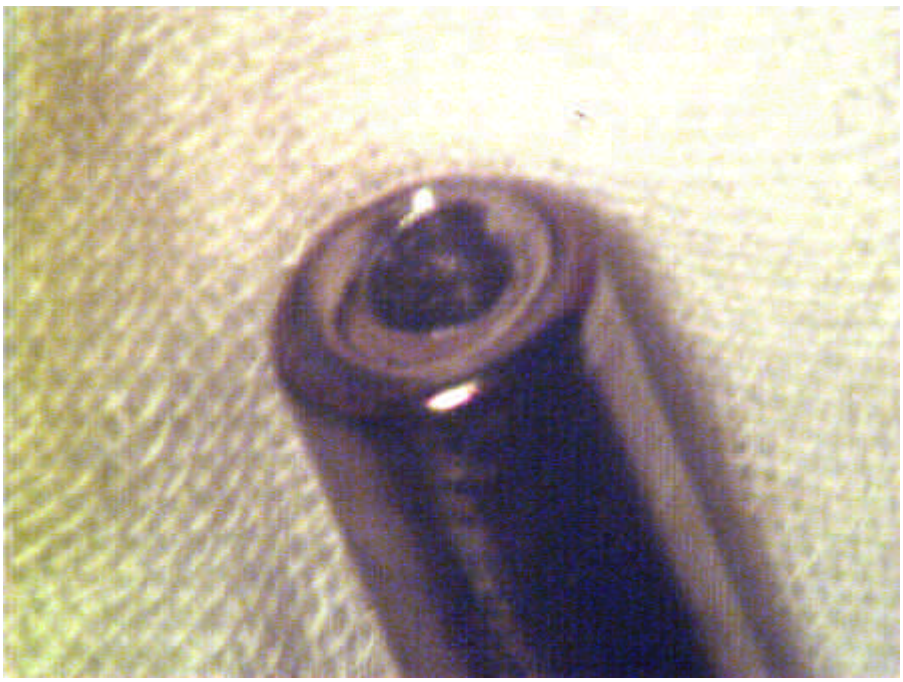

Figure 4.23 Top end of Fuel Pin 12. Note the hole from the fission gas pressure measurement. It also appears (top of hole) that the drill may have wandered or the pin may have rotated before the drill bit started cutting the hole. [P12-top.JPG]

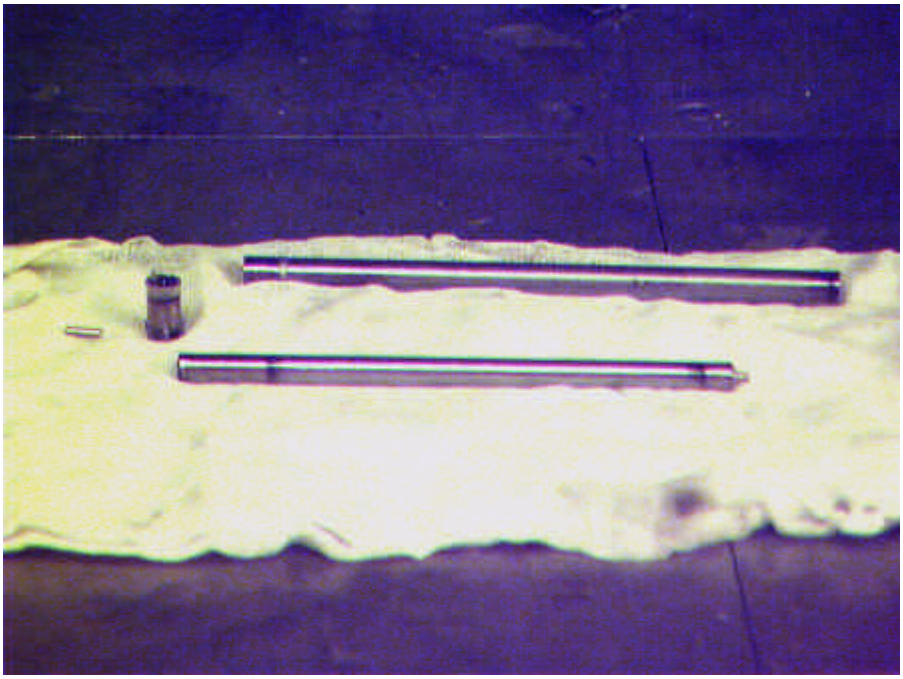

Figure 4.24 Side view of Fuel Pin 12. Note the capsule components in background. [P12-side-front.JPG]

4.7 Fuel Pin Dimensional Inspections

The results of the fuel pin dimensional inspections are shown in Table 4.6. For practical purposes, only insignificant variations from the preirradiated values were noted. Within 0.001 inches, there were no indications of bowing, out of roundness, or bambooing. Radiation-induced dimensional changes in the Fuel Pin 5 clad diameter were less than 0.001 inches, as discussed in Chapter 6. Fuel Pin 12 clad has two spots where the pre/post irradiation diameter difference was greater than 0.001 inches, but less than 0.002 inches. The method of measurement was the same as that shown in Figure 4.7**.**

In general, Fuel Pin 12 appears to be slightly larger in diameter than Fuel Pin 5; however, both fuel pins easily slid within their respective (very closely fitting) capsules.

TABLE 4.6 Fuel Pin Measurements			
Axial Location from Top (inches)	**Diameter Measurement (in) (±0.0005)**		**Preirradiation Values (in)**
	0°	**90°**	
Fuel Pin 5			
0.50	0.3811	0.3810	0.3806 to 0.3808
2.00	0.3811	0.3814	
3.50	0.3814	0.3814	
5.50	0.3805	0.3815	
7.00	0.3805	0.3805	
Fuel Pin 12			
0.50	0.3812	0.3814	0.3806 to 0.3808
2.00	0.3825	0.3824	
3.50	0.3824	0.3814	
5.50	0.3818	0.3817	
7.00	0.3814	0.3815	
Length (in) (±0.005)			
Fuel Pin 5	7.413		7.41 less pedestal
Fuel Pin 12	7.413		7.41 less pedestal
Mass (g) (±0.1g)			
Fuel Pin 5	111.2		Not given
Fuel Pin 12	111.7		Not given

4.8 Metrology Summary

No abnormal appearance or behavior was noted for either the capsules or the fuel pins. Gamma scans supported this conclusion by revealing intact capsule and fuel pin internals. Fission gas pressure was within expected bounds and the fuel pins were easily withdrawn from the opened capsules. All mechanical indications are that the irradiation is proceeding as planned.

5. METALLOGRAPHY

5.1 Introduction

This Chapter details the PIE of the microstructure of the Type A fuel (non-TIGR plutonium oxide feed) contained in Capsule 2 (Fuel Pin 5) and the Type B fuel (TIGR plutonium oxide feed) contained in Capsule 9 (Fuel Pin 12) of the Average Power Test. Specimens were cut from locations within the pellet stack near the top and bottom of both fuel pins. No differences were noted between the fuel types. The major observation was the presence of numerous plutonium rich agglomerates with some sizes as large as 500µm. No irradiation difficulties have been experienced with these agglomerates, but they do indicate less than optimal powder mixing.

5.2 Sample Preparation

Two specimen disks were cut from each fuel pin, one near the top of the pin (pellet 1) and one near the bottom of the pin (pellet 14). (See Figures 7.1 through 7.4 for details of the cutting guide.) The specimens were mounted in a metallographic mount by epoxy potting. Subsequently, each mount was rough ground and then polished with progressively finer diamond compounds.

Each mount was assigned a unique number. Table 5.1 shows the relationship between the specimen numbers and the mount identity number. The mounts were photographed and a composite image assembled. Higher magnification was used to examine specific details.

TABLE 5.1
Mount ID Numbers and Fuel Pellet Locations

Specimen Number	Mount ID	Location
FP-5-M-1	6145	Fuel Pin 5 Pellet 1
FP-5-M-2	6146	Fuel Pin 5 Pellet 14
FP-12-M-1	6143	Fuel Pin 12 Pellet 1
FP-12-M-2	6144	Fuel Pin 12 Pellet 14

5.3 Results of the Polishing

The results of the polishing are shown in Figures 5.1 through 5.11 for the four mounts. No abnormal behavior was seen; the cracking is normal for LWR fuel. However, rather large plutonium rich agglomerates are clearly visible. Originally, it was believed that the powder mix

received a high level of mixing such that the agglomerates would be very small. However, now that the higher burnup of these intermediate capsules clearly shows the agglomerates, this is seen to not be the case. These regions can be seen in Figures 5.1 through 5.4, where they appear as "blemish" like light gray patches. For the most part, the visible agglomerates extend from the pellet surface up to about the 1/4 radius point.

Figures 5.5 through 5.7 show zooms of Mount 6144 with radius markers. Note that the agglomerates are most common in the outer regions of the pellet where lower temperatures prevailed during the irradiation.

The agglomerates do not appear to be evenly distributed. Figure 5.8 illustrates the grouping or clumping of the agglomerates. Figure 5.9 shows an agglomerate at the edge of the pellet interacting with the inner surface of the clad. Other than agglomerate bonding to the inner surface, no other clad interactions were noted.

The maximum agglomerate size found was about 500µm in diameter (Fig. 5.10). As can be seen from the figures, agglomerates in the 200µm diameter range were common. Figure 5.11 shows a high magnification view of a plutonium-rich agglomerate. The high concentration of fission bubbles within the agglomerate is clearly visible.

Higher magnification views (Fig. 5.12) of the inner regions of the pellet showed little indication of the large agglomerate structures seen in the outer regions of the pellet. Figure 5.13 shows some regions (bubbles/voids/porosity?) that might be indicative of agglomerate coalescing, but a conclusion is elusive.

The agglomerates have a much higher plutonium density and thus a much higher burnup than the surrounding UO_2 matrix. The agglomerates are generally clearly visible after two cycles in an LWR, a burnup of roughly 20-30 GWd/MT. At temperatures below about 900 to1000°C, thermal diffusion is insufficient for the repair of defects, so the agglomerates retain their structure. [Ref 15] The lack of the characteristic agglomerate structure in the central region of these micrographs is not surprising as the central pellet regions ran at temperatures in excess of 900°C during the irradiation; consequently, coalescing of the gas bubbles/voids occurs in these regions.

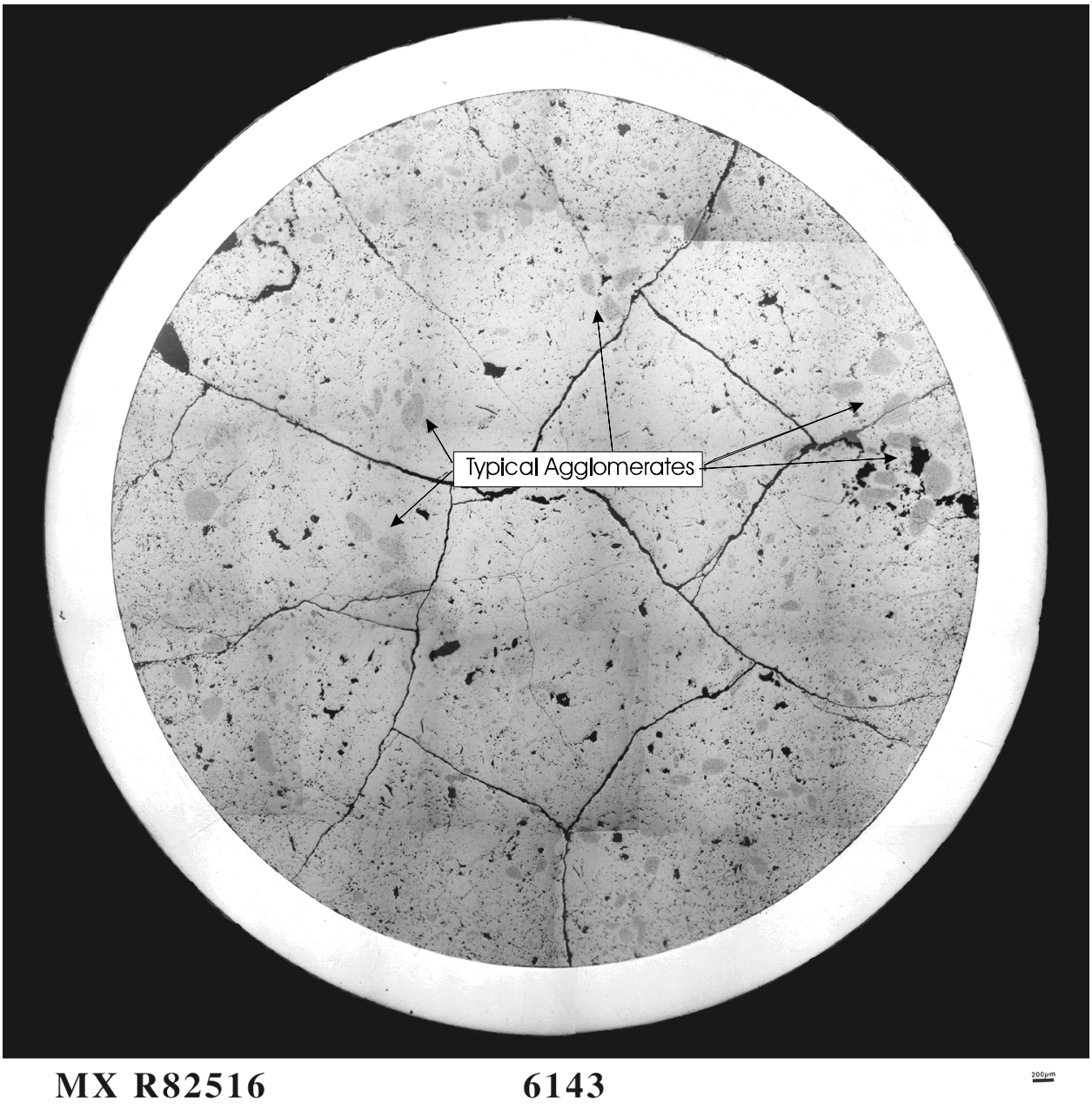

Figure 5.1 Composite view of Mount 6143. The plutonium rich agglomerates can be clearly seen. [CircleAg.wpg]

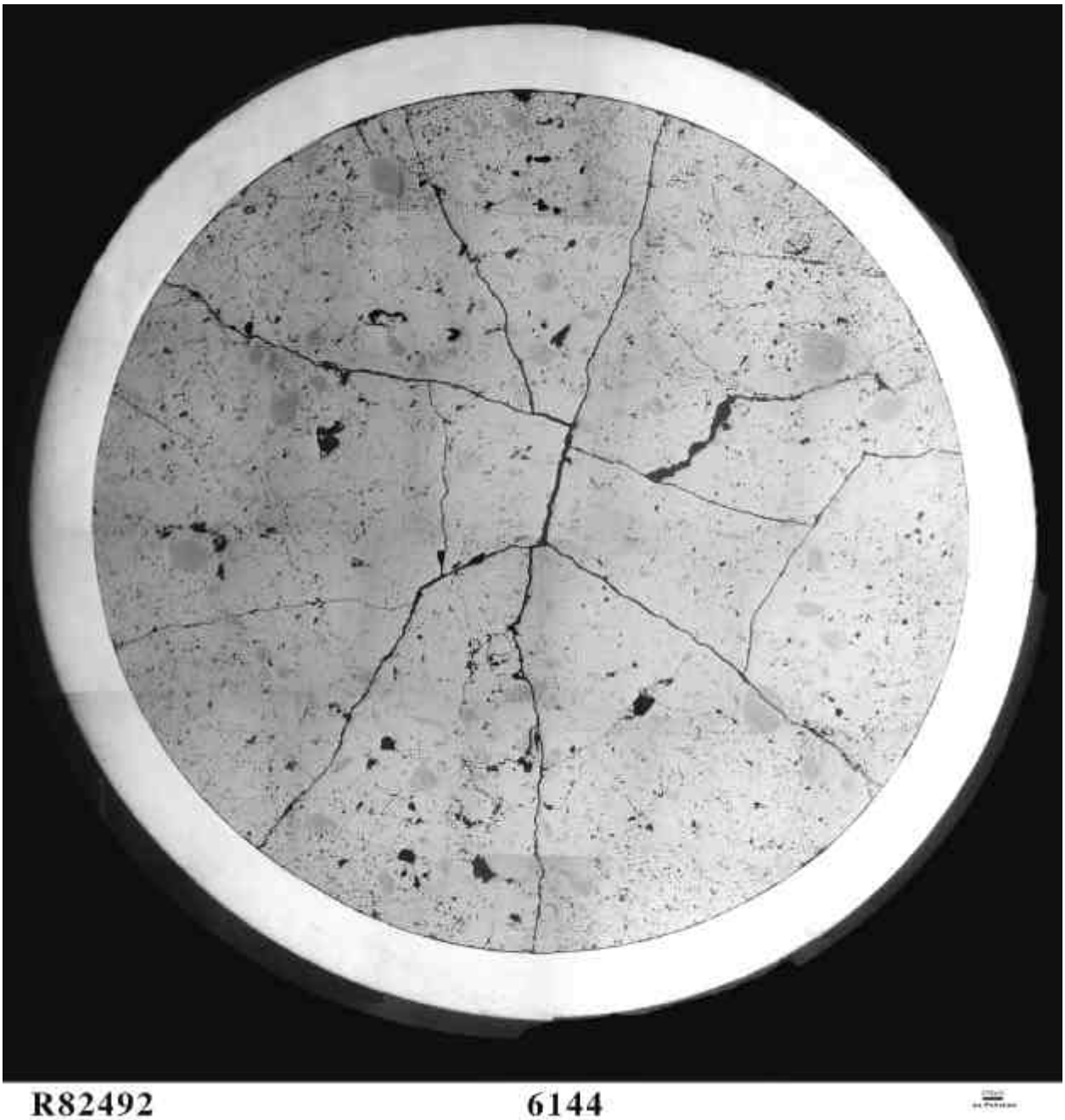

Figure 5.2 Composite view of Mount 6144. This level of cracking is considered normal. Note the plutonium rich agglomerates. [MXR82492.tif]

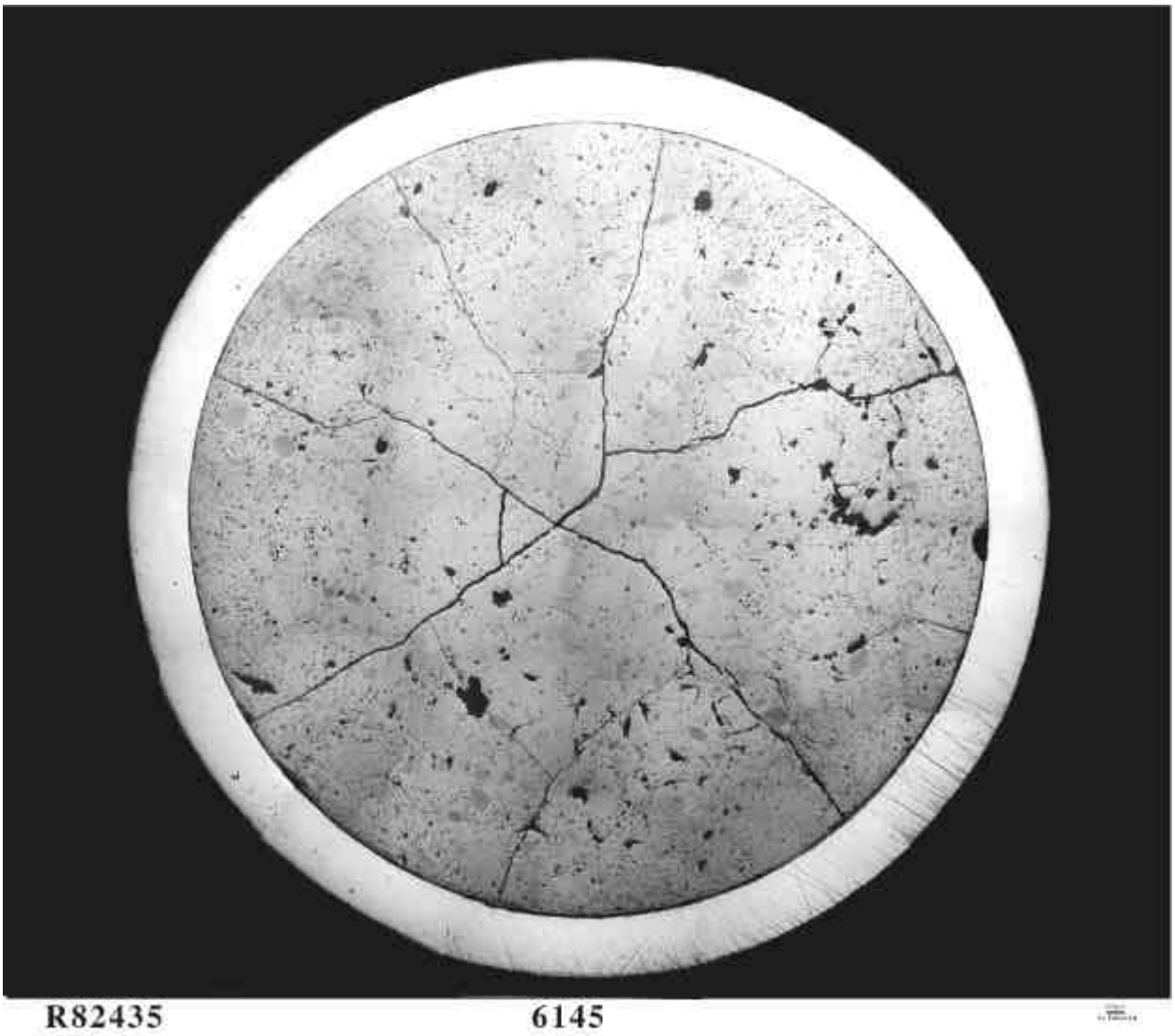

Figure 5.3 Composite view of Mount 6145. Almost all the cracks are radial. The black regions are epoxy filled pull-out areas. The agglomerates are clearly visible. [MXR82435.tif]

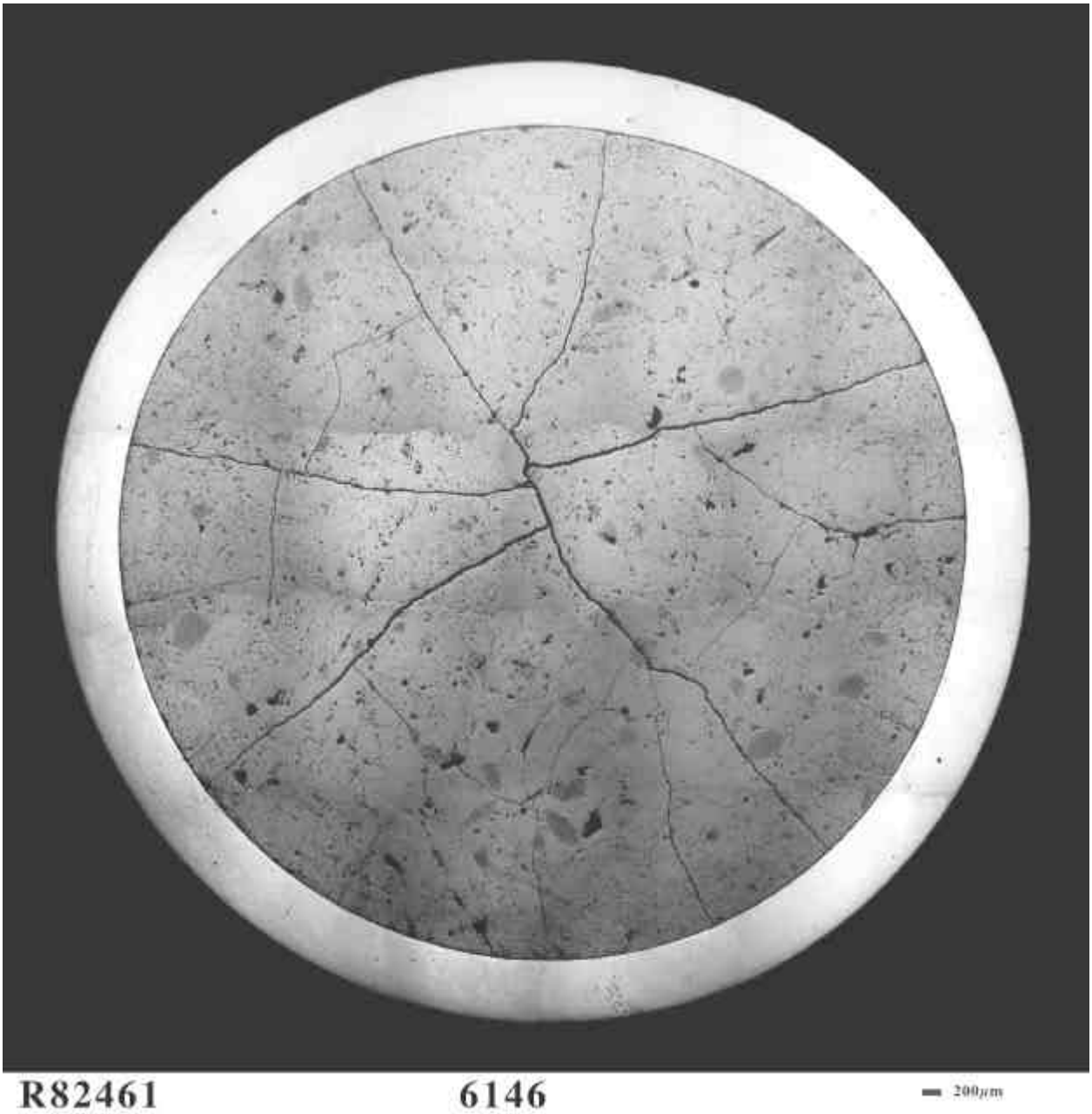

Figure 5.4 Composite view of Mount 6146. Again, note the plutonium rich agglomerates and radial cracks. [MXR82461.tif]

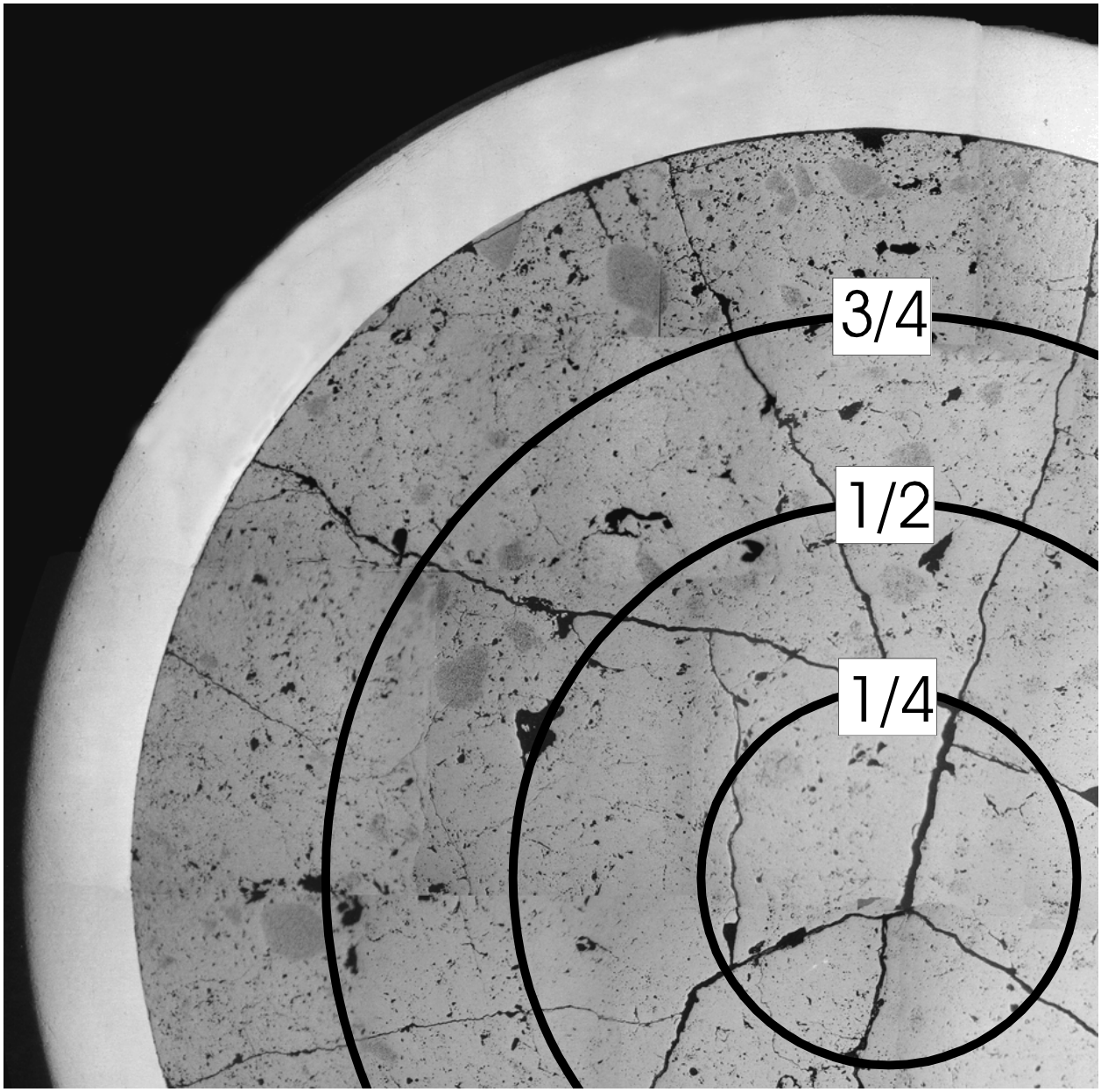

Figure 5.5 Graduated zoomed view of 1/4 of Mount 6144. [aggmap.wpg]

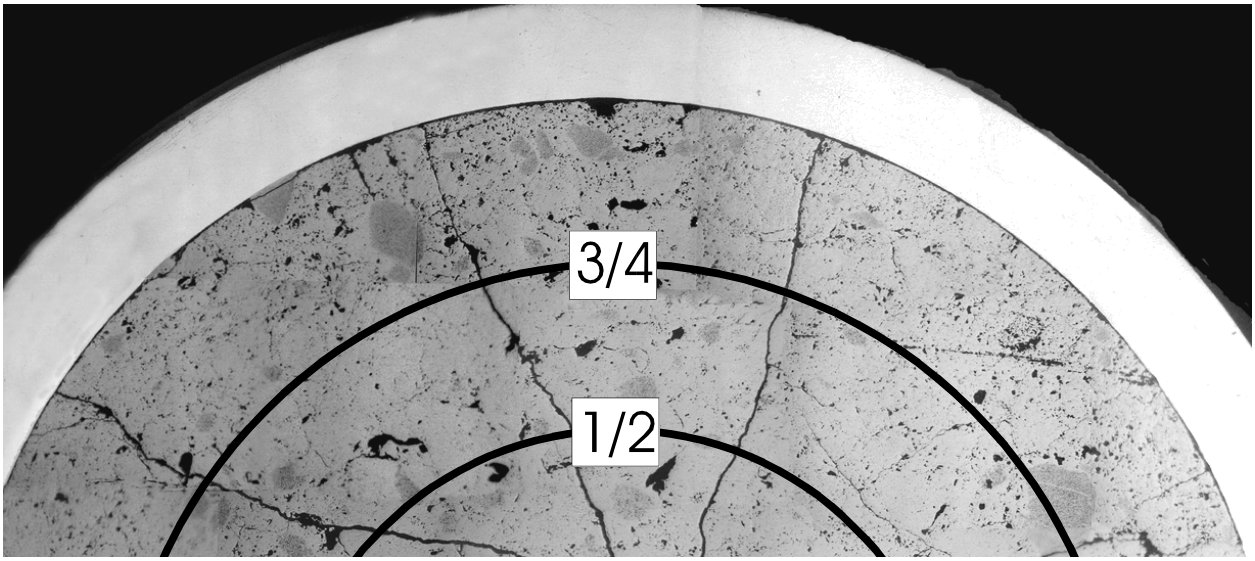

Figure 5.6 Graduated zoom of Mount 6144 showing plutonium rich agglomerates in the outer radius regions. [aggmap.wpg]

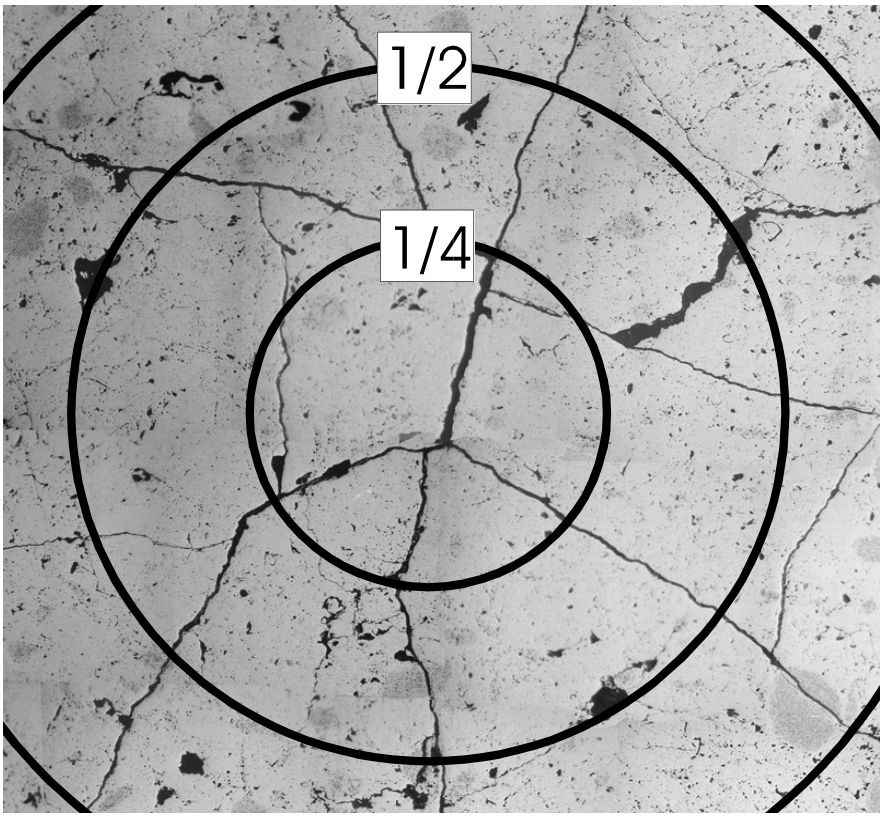

Figure 5.7 Graduated zoom of Mount 6144 showing the center region of the pellet. [aggmap.wpg]

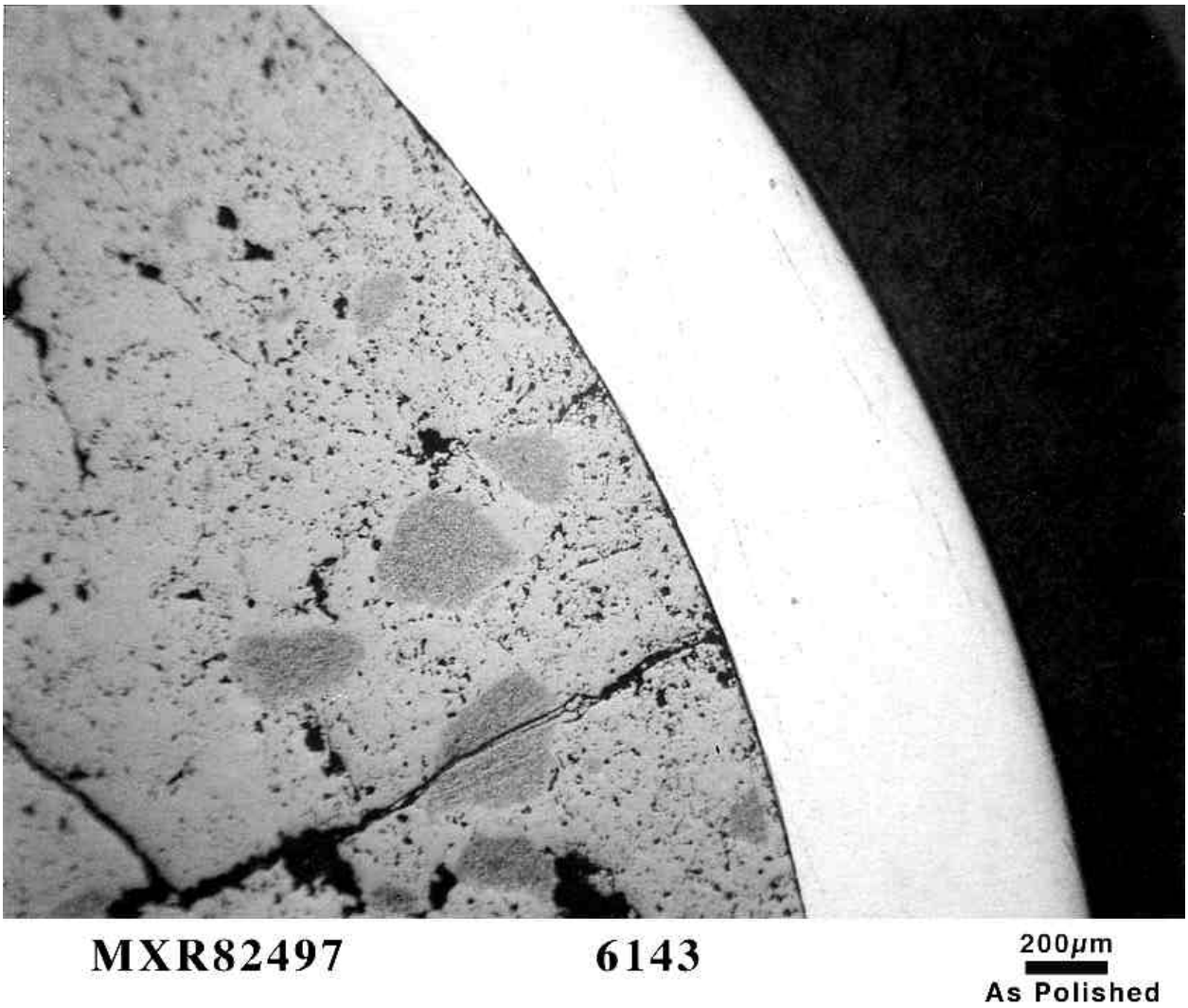

Figure 5.8 Closeup view of a group of agglomerates in Mount 6143. In general, the agglomerates were not uniformly distributed and some were rather large. [MXR82497.tif]

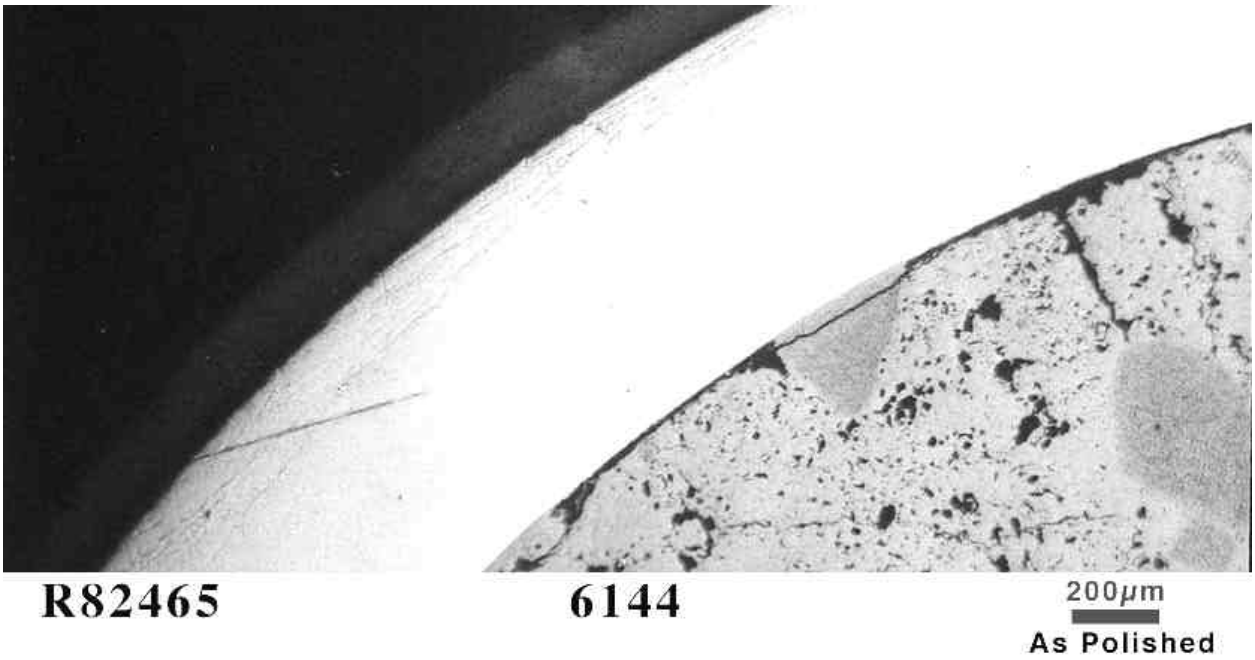

Figure 5.9 Closeup of Mount 6144 showing an agglomerate bonding to the clad. [MXR82465.tif]

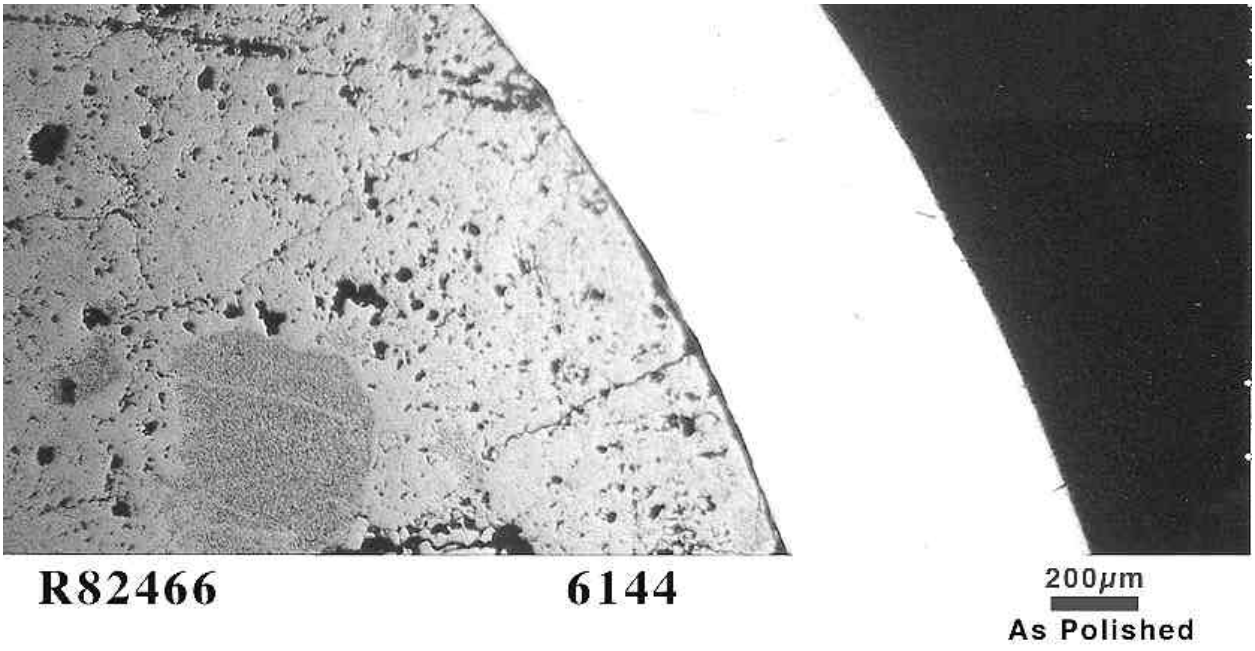

Figure 5.10 One of the larger agglomerates found in Mount 6144. Approximately 500µm in diameter. [MXR82466.tif]

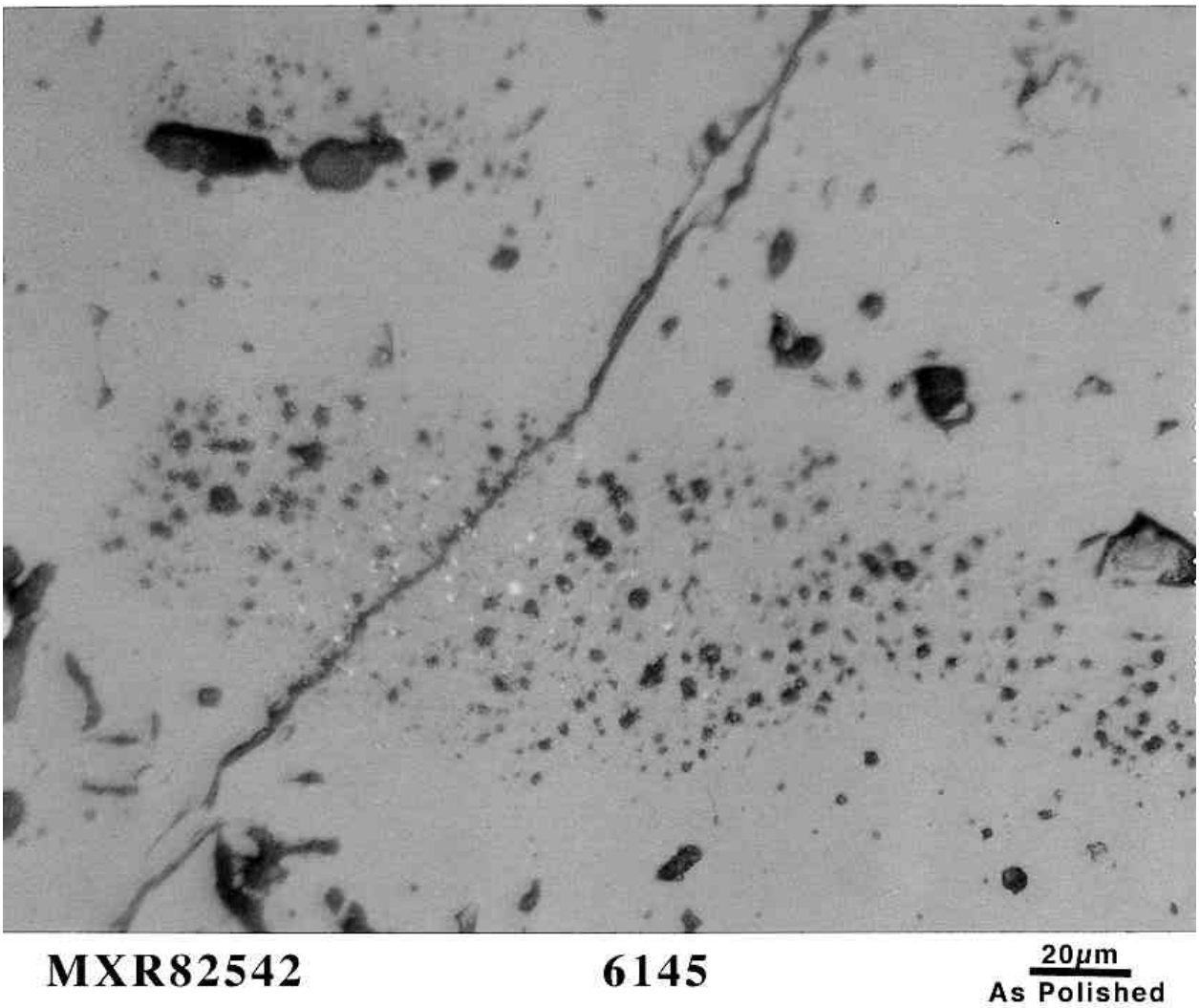

Figure 5.11 High magnification view of an agglomerate in Mount 6145. Note the higher density of bubbles/voids. [MXR82542.tif]

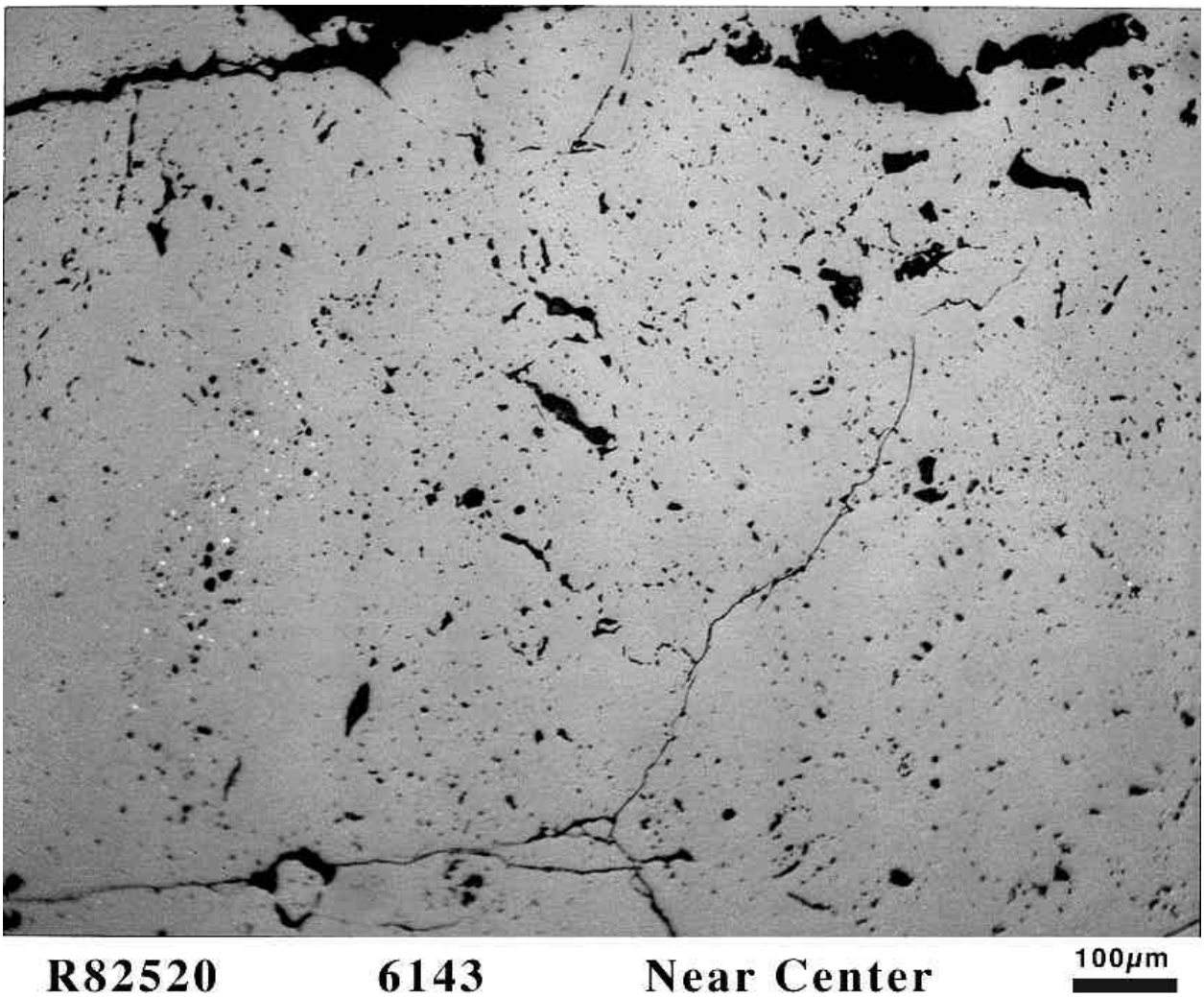

Figure 5.12 Medium magnification of the central region of Mount 6143. The central region lacks strong indications of agglomerates, although one may see a weak indication of an agglomerate in the lower left corner. [MXR82520.tif]

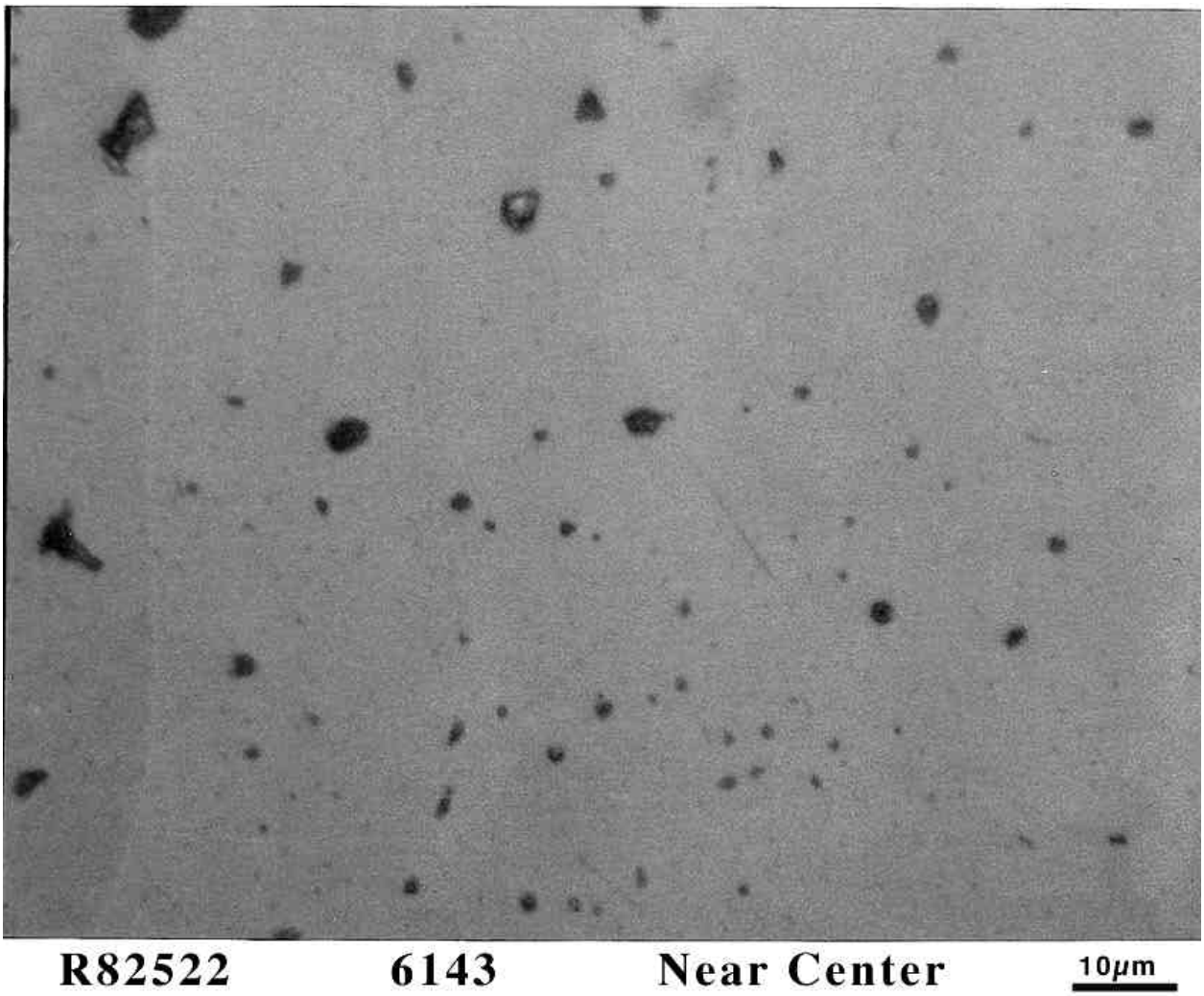

Figure 5.13 High magnification view of the central region of Mount 6143. Generally only small porosity is seen. Because of the higher temperature, the agglomerate structures likely have coalesced into the micron sized bubbles/voids. [MXR82522.tif]

5.4 Mount 6146 Etching

Mount 6146 was etched to bring out some of the phase and grain detail by using a solution of 2.5ml H_2SO_4 + 48 ml H_2O_2. The mount was swabbed with the solution for a period of roughly 30s. The resultant etching is not completely uniform, but the essence of the grain structure can be ascertained. The edge region etched more evenly than the center region. The grain size does not appear to be significantly different from the preirradiated state (as visually inferred from the micrographs).

A composite of the etching is shown in Figure 5.14; this is the same mount as shown in Figure 5.4. The edge regions for medium high and high magnification are shown in Figures 5.15 and 5.16. The central regions for similar magnification are shown in Figures 5.17 and 5.18.

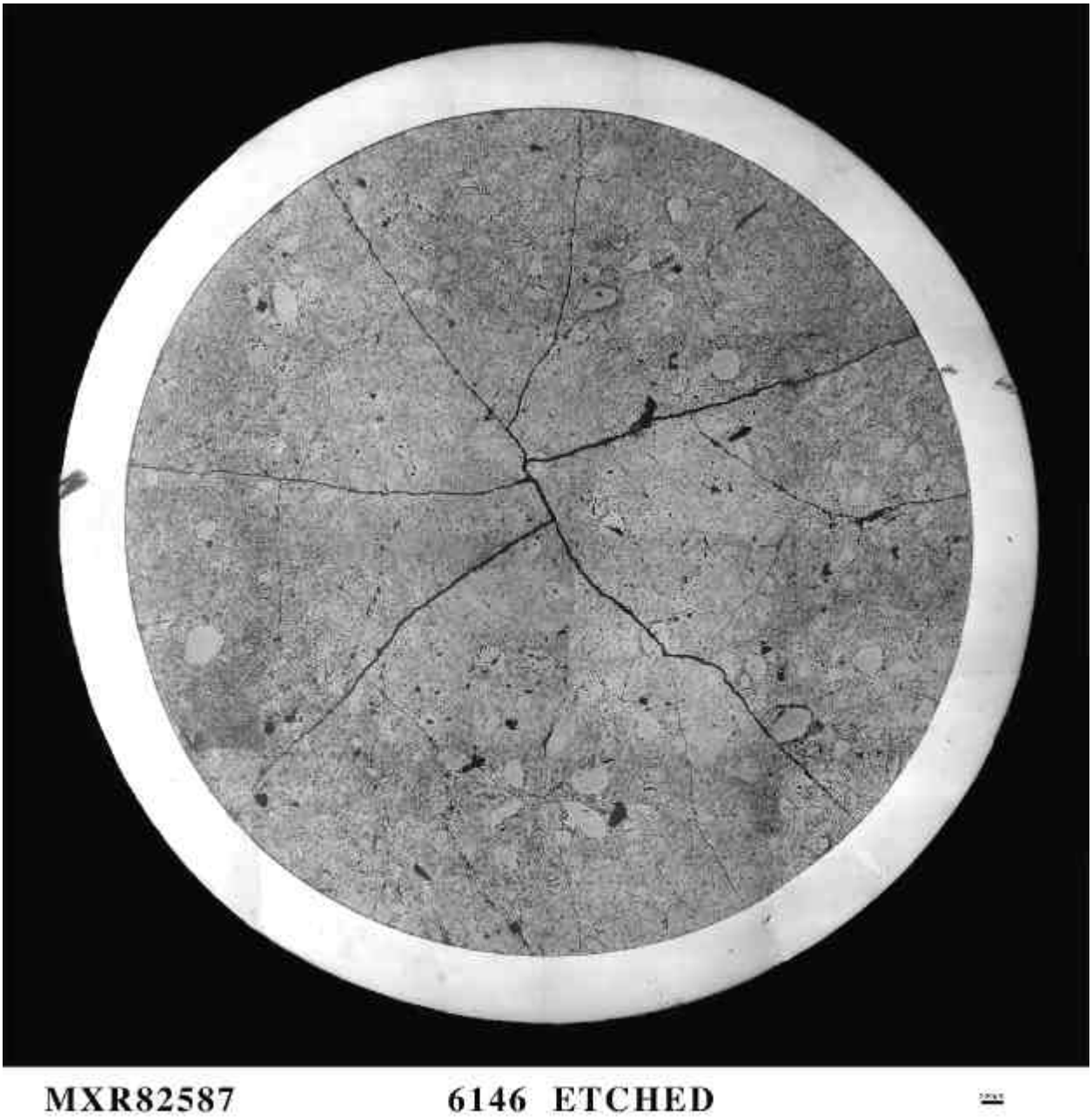

Figure 5.14 Composite view of Mount 6146 after etching. Note the plutonium rich agglomerates. [MXR82587.tif]

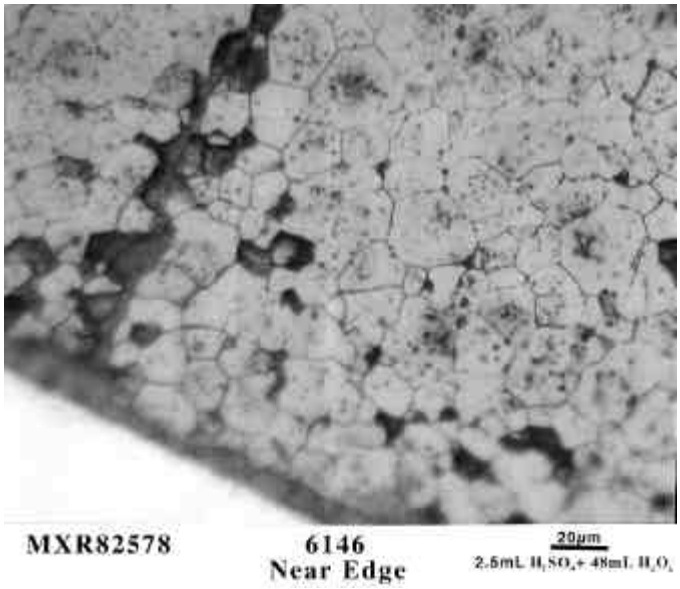

Figure 5.15 Medium high magnification of the edge region of Mount 6146. Note the grain boundaries. [MXR82578.tif]

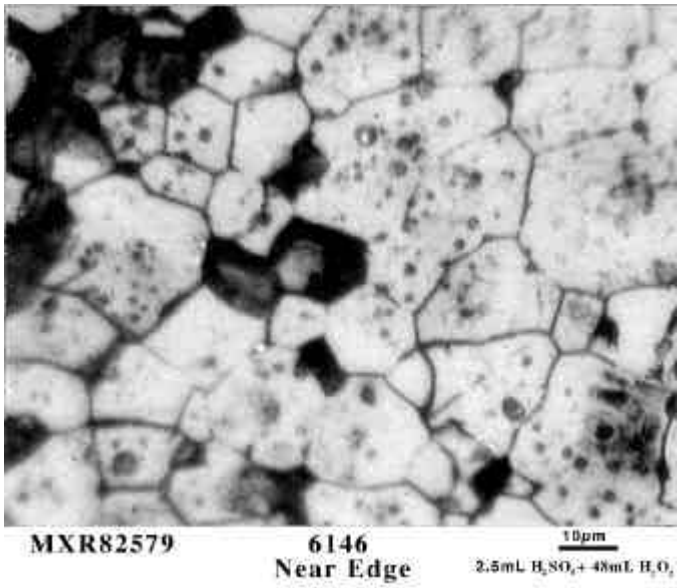

Figure 5.16 High magnification view of the edge region of Mount 6146. [MXR82579.tif]

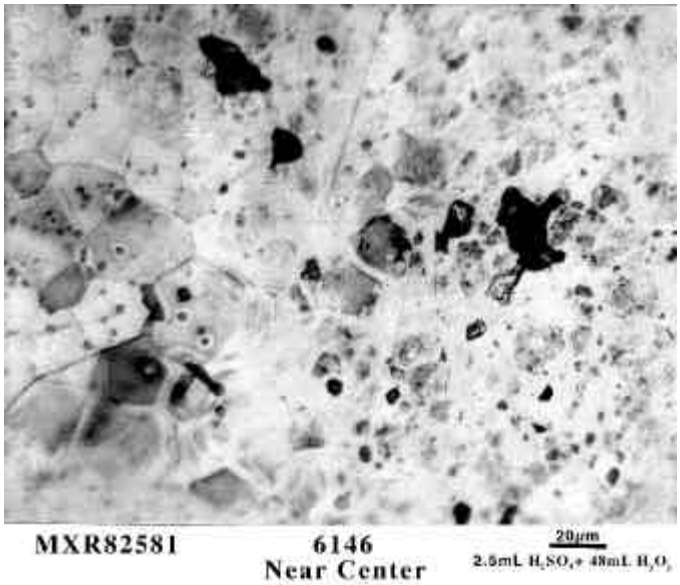

Figure 5.17 Medium high magnification view of the central region of Mount 6146. The grain boundaries are less pronounced than at the edge region. [MXR82581.tif]

Figure 5.18 High magnification view of the central region of Mount 6146. [MXR82582.tif]

5.5 Gamma Scan of Mount 6145

Mount 6145 was gamma scanned to obtain an estimate of the burnup profile as inferred from the gamma emitting fission products. The mount was scanned using a long 1/16" collimator. Because of the approximately 2 mil clearance between fuel pin and capsule, rotation may have occurred during cutting, consequently, the side of the mount that faced the reactor center line can not be reliably determined and the orientation of the scanned segment is random.

An initial spectrum analysis indicated that ^{106}Ru produced a strong and easily discriminated signal so it was chosen for the gamma scan. Also, ^{106}Ru is not as mobile as other fission products such as ^{137}Cs. The scan indicated that the activity was radially asymmetric about the center of the fuel specimen, which was expected from the MCNP code calculations performed at INEEL and which was observed in the previous PIE work at 8 GWd/MT. The inferred off center peaking is roughly 20%.

Figure 5.19 shows an unprocessed scan and Figure 5.20 shows the same results with smoothing. The scans include many more points than necessary for the collimator resolution (and the mount contains numerous cracks) so the reader is cautioned not to read too much into the fine detail. The actual resolution is only 6-8 points along the radius so only gross detail is resolved. This technique is not capable of accurately locating the burnup profile or resolving any “rim” effect.

The light blue ring between the clad (dark blue) and the fuel (green) is due to the finite resolution of the gamma scanner and comes from the detector seeing both the edge of the fuel and the edge of the clad at the same time. This is a transition artifact and should not be inferred to be part of the burnup structure.

Because of the coarse resolution, the scanning data should be considered qualitative rather than quantitative; however, these results do indicate that the burnup profile is asymmetric as was predicted by the calculations.

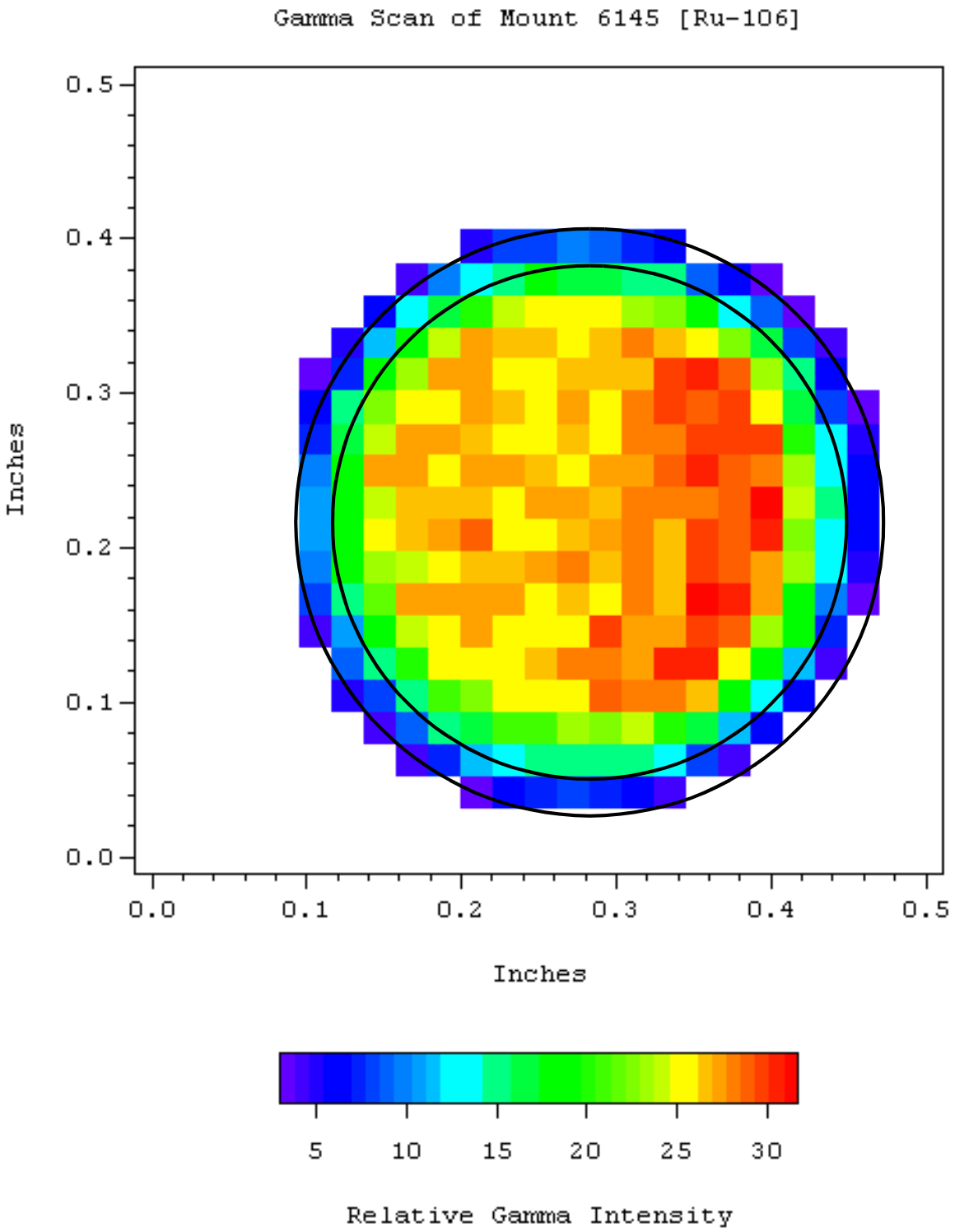

Figure 5.19 Data from raster scan of Mount 6145. The solid circles outline the approximate location of the clad. [raw6145.wpg]

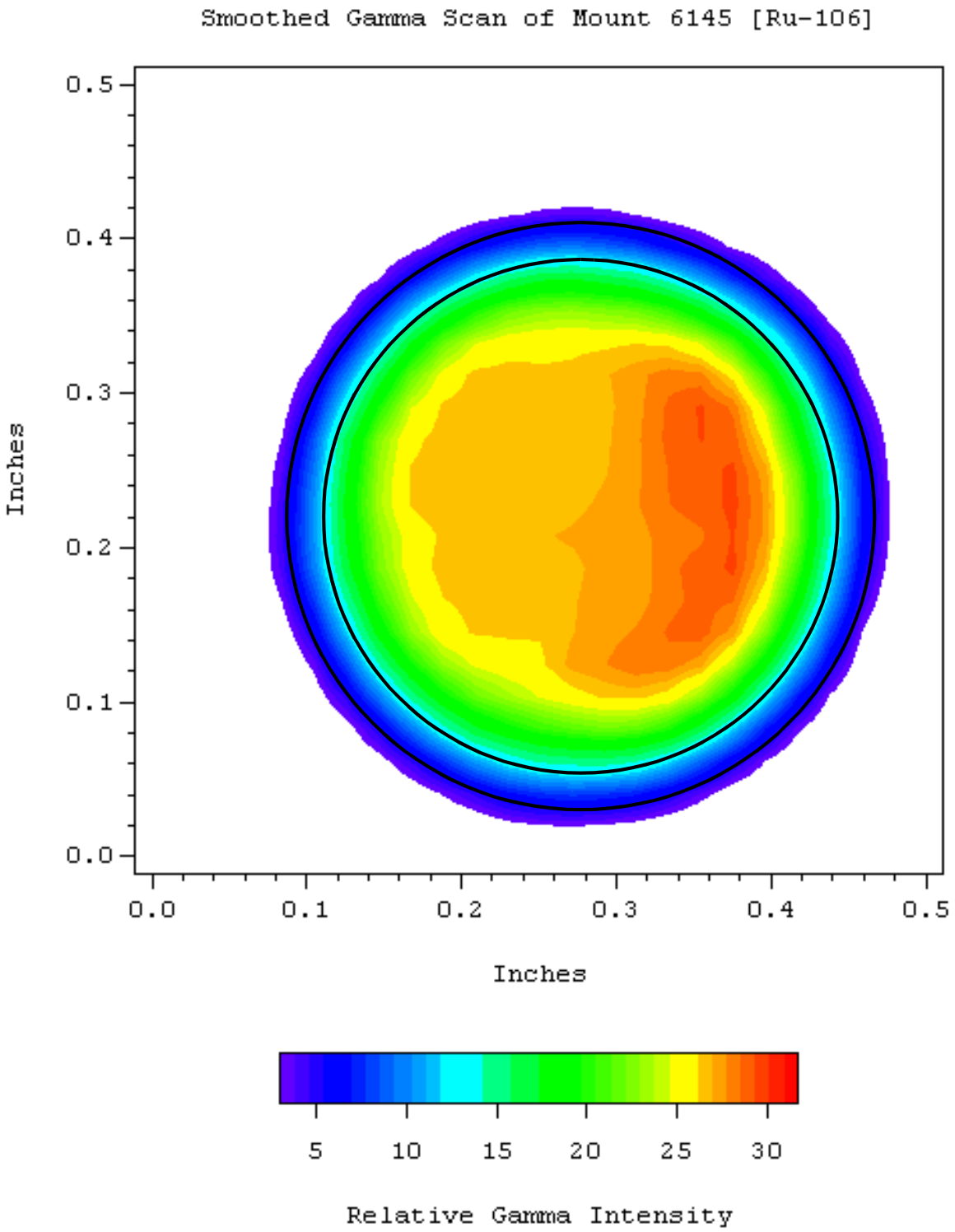

Figure 5.20 Smoothed data from the raster scan of Mount 6145. The solid circles outline the approximate location of the clad. [sm6145.wpg]

5.6 SEM Analysis

A SEM mount (Mount 6147) was made from the specimen FP-5-SEM-1 material and it was examined using the SEM/microprobe. Four elements were resolved - Pu, U, Pd, and Ru. Of these elements, Pu and U were selected for mapping because of their usable signals and their important in the structure of the agglomerates. An agglomerate was randomly selected from the mid radius region and it and the nearby fuel matrix were scanned for Pu and U by examining and processing the signal from the $L_{á}$ line. The Pu signal was weak, but usable. Figure 5.21 is a two color map of a portion of the agglomerate, the matrix, and the interface between the two. Note the strong Pu presence in the agglomerate (the black regions are voids). The elements Pd and Ru showed similar segregation, but in the form of much smaller discrete inclusions rather than the diffuse structure shown for Pu.

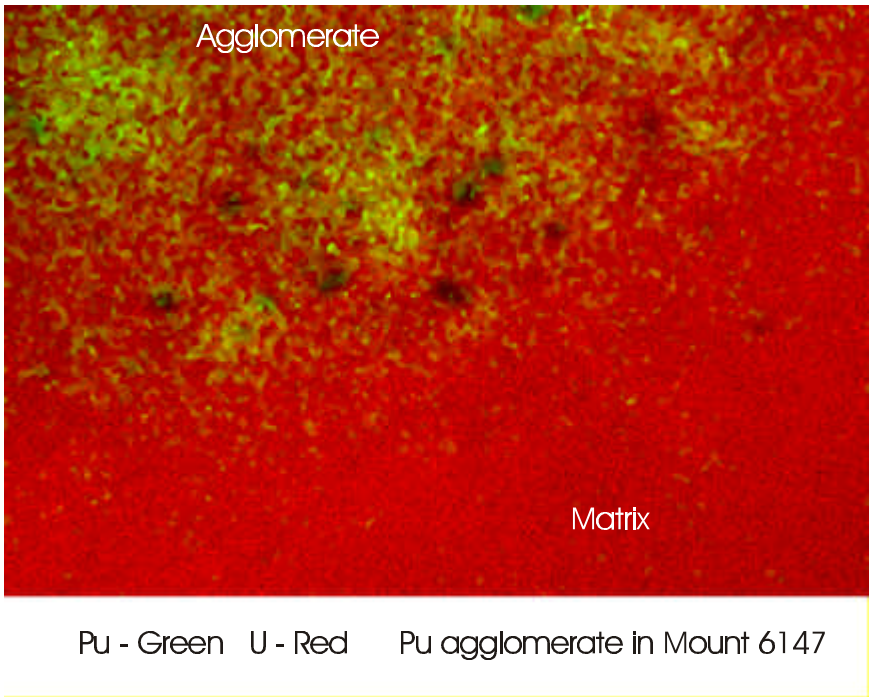

Figure 5.21 Color map of an agglomerate and the nearby matrix. The agglomerate was at the fuel pellet mid radius. [Pu-U Pic.wpg]

An electron backscatter image of the same region is shown in Figure 5.22 showing the more familiar view of the agglomerate.

Table 5.2 shows the relative X- ray signals (integrated counts) in the matrix and agglomerate along with their ratios. The reader is cautioned that considerable signal processing was required because of noise induced by the sample radiation, so that the uncertainty of the data could be considerable. Future work on the higher burnup capsules will examine the SEM mapping issues

in greater detail. The purpose of this work is to show the high degree of Pu segregation between the agglomerate and the matrix.

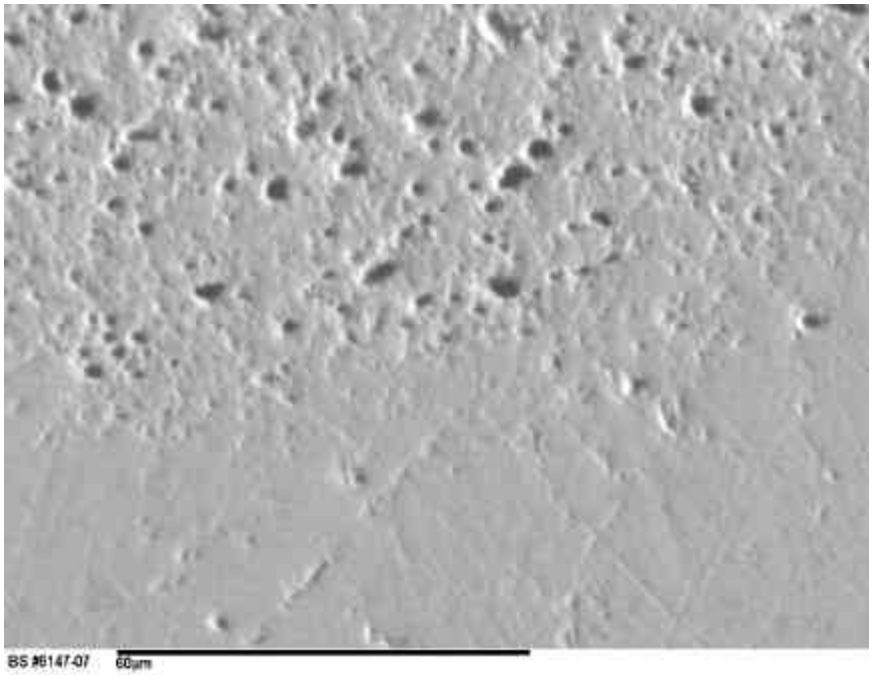

Figure 5.22 Electron backscatter view of the agglomerate and fuel matrix detailed in Figure 5.21. [6147-07.tif]

TABLE 5.2
SEM Data

Object	**Pu Relative Signal**	**U Relative Signal**	**Pu/(Pu+U)**
Fuel Matrix	89	5436	0.016
Agglomerate	647	4514	0.125
Ratios	7.3	0.83	

6. APT MOX FUEL DENSIFICATION AND SWELLING

6.1 Introduction

Three metallographic (Met.) mounts were prepared from Capsule 1 (Fuel Pin 2) after Phase I of the APT, see Section 5.3.4 in Reference 13 [the early PIE final report]. Following completion of Phase II, two mounts were prepared from Capsule 2 (Fuel Pin 5) and two from Capsule 9 (Fuel Pin 12); descriptions of the sample preparation and polishing and etching techniques are presented in Chapter 5 of this report. Altogether, seven metallographic mounts have been prepared from fuel pins withdrawn after Phases I and II of the APT irradiation; the mount identification numbers, fuel type, and axial locations are given in Table 6.1. (Pellet 1 is located adjacent to the fuel pin gas plenum.)

Table 6.1.
Fuel Pin Metallographic Mount Identification

APT Irradiation Phase	Met. Mount ID Number	Capsule	Fuel Pin	Fuel Type	Axial Location (Pellet Number)
I	6139	1	2	A	5
I	6140	1	2	A	5/6 interface
I	6141	1	2	A	6
II	6143	9	12	B	1
II	6144	9	12	B	14
II	6145	2	5	A	1
II	6146	2	5	A	14

The PIE metrology of the Phase-I capsules (1 and 8) and fuel pins (2 and 11) is contained in Chapter 4 of Reference 13. The Phase-II capsule (2 and 9) and fuel pin (5 and 12) PIE metrology is given in Chapter 4 of this report. The capsule and fuel pin metrological results and measurements made directly from photographic enlargements of the metallographic mounts are employed in this Chapter to determine:

1. The fuel pin Zircaloy clad thickness and internal diameter.
2. The free area within the fuel pin (that is, the peripheral gap between the fuel and the clad and the internal cracks within the fuel pellet), and
3. The fuel pellet outer diameter.

These quantities were determined for each of the metallographic mounts and are presented as functions of fuel burnup in Section 6.2. Finally, in Section 6.3, the data will be used to access the fuel densification assumptions currently employed with the Capsule Assembly Response - Thermal and Swelling (CARTS) code fuel swelling models (Section 3.3 of Reference 12).

6.2 Capsule Component Dimensions

6.2.1 Capsule Outer Diameter

The preirradiation value for the stainless steel capsule's outer diameter for Capsules 1, 2, 8, and 9 is reported as 0.4643 to 0.4649 inches for each capsule (Table 2.1). Here 0.4643 in. is the minimum measured outer diameter, while 0.4649 in. is the maximum measured outer diameter.

For the postirradiation hot-cell measurements, the average of the Capsule 1 measurements is 0.46462 in. [with a standard deviation (σ) of 0.16 mils]. The average outer diameter of Capsules 2, 8, and 9 is 0.46519 in. (σ = 0.18 mils).

Using the preirradiation dimensions for the stainless steel capsule, the measured capsule temperature (at the mid-point, within the fueled region) of ~52.5°C in the hot cell, and the thermal linear expansion formulation for 304 stainless steel (from CARTS), the estimated hot-cell diameter of the capsule lies in the range from 0.46453 to 0.46513 inches. This range essentially spans the observed measurements; there is no apparent change in the measured capsule outer diameter that cannot be explained simply by thermal expansion.

6.2.2 Fuel Pin Outer- and Inner-Clad Diameters

The nominal as-constructed outer diameter of the fuel pin Zircaloy cladding is 0.3810 inches (with tolerances of +0.0000 in. and –0.0005 in.). The preirradiation value for the Zircaloy clad outer diameter for Fuel Pins 2, 5, 11, and 12 is reported as 0.3806 to 0.3808 inches (Table 2.1).

The PIE metrology results for the clad outer diameter include positions outside the six-inch fueled region, which extends from one to seven inches as measured from the top of the fuel pin. Table 6.2 contains averages of the diameter measurements taken within the fueled region during the PIEs conducted to date. The burnups listed in this Table are capsule averages inferred from the pellet radiochemical analyses.

Figure 6.1 (upper half) shows the cladding outer diameter as a function of burnup as measured during the PIEs. Applying the thermal linear expansion formulation for Zircaloy (from CARTS) with the measured clad temperatures, the hot-cell diameter of the fuel pin would be expected to range from 0.38064 to 0.38084 inches. The cladding outer diameters (including the computed uncertainty) plotted in Figure 6.1 are greater than these expected values and, hence, cannot be accounted for by thermal expansion alone.

It is postulated that clad creep (outward) is occurring during the APT irradiation. All the

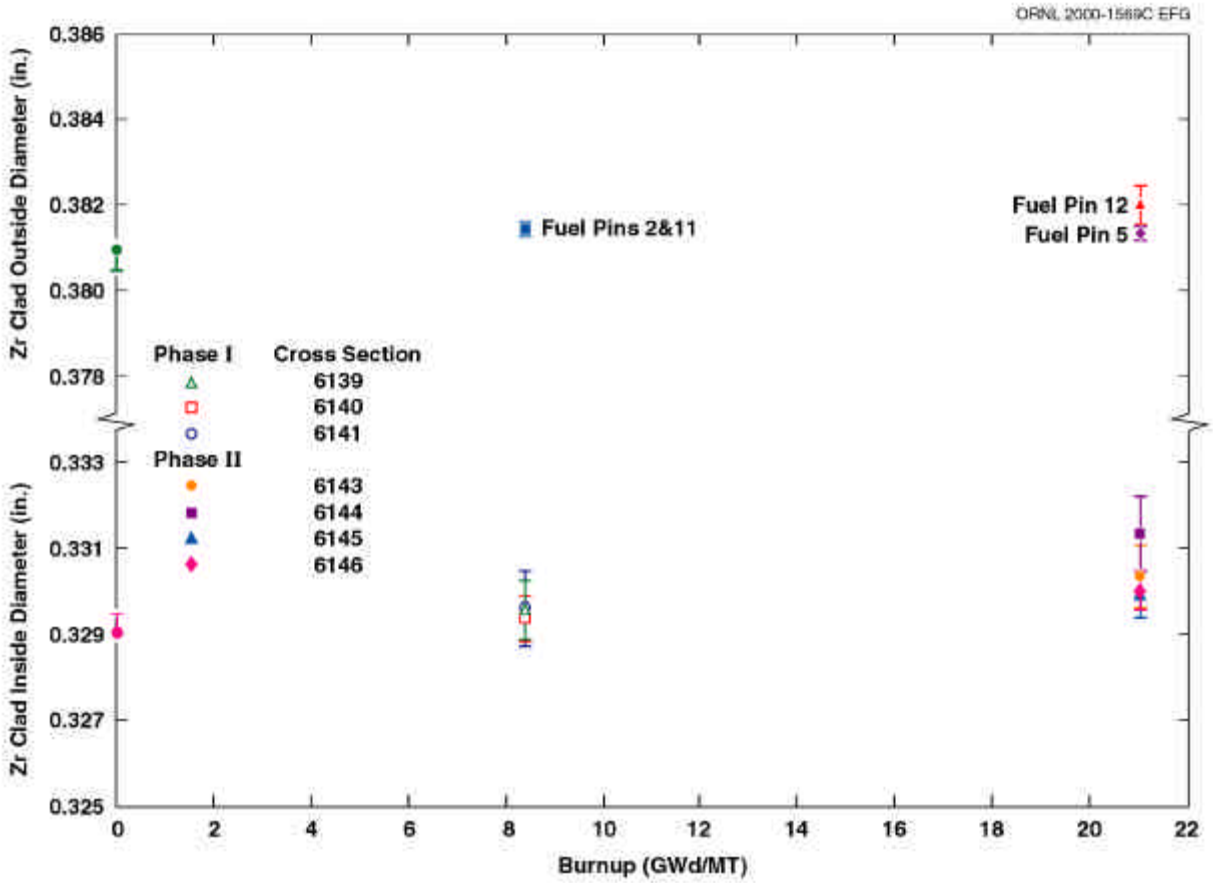

Figure 6.1 Cold clad inner and outer diameters as measured in APT MOX fuel pins.

ingredients for creep are present in the experiment: the presence of neutron irradiation, a positive pressure differential across the cladding throughout the irradiation [~6 psi at beginning of life (BOL) and ~17 psi at the end of Phase II], and the clad temperature during irradiation of 320°–400°C. The amount of cladding creep that would be expected for these conditions can be estimated by reference to literature values, but the situation is not analogous. Literature values are usually derived from PWR (pressurized water reactor) experience, where the creep is inward, not outward.

The fuel pin clad inner diameter will now be considered. The nominal construction inner diameter of the Zircaloy cladding is 0.3290 inches (with tolerances of +0.0005 in. and –0.0000 in.). The preirradiation value for the clad inner diameter for Fuel Pins 2, 5, 11, and 12 is reported as 0.3290 to 0.3294 inches (Table 2.1).

The postirradiation inner diameter of the cladding must be estimated from the PIE measurement of the clad outer diameter (the averages given in Table 6.2) by subtracting the clad thickness, as measured directly from photographic enlargements of the metallographic mounts. Using a scaling factor from the enlarged photographs and approximately 40 measurements of the clad

thickness from each metallographic mount, an average clad thickness and uncertainty for each mount is determined. The clad inner diameter is then calculated. Finally, the uncertainties in the clad outer diameter and clad thickness are propagated inward to yield the uncertainty in the inner diameter. The calculated clad inner diameter and uncertainty for each metallographic mount are presented in Table 6.3.

Table 6.2
Measured Fuel Pin Outer Diameters

APT Irradiation Phase	Burnup (Radiochemistry) (GWd/MT)[1]	Burnup MCNP[2] (GWd/MT)	Fuel Pin	Clad Average Outer Diameter (inches)	Standard Deviation about the mean (mils)
I	7.85 ±0.4	8.6 ±0.2	2	0.38134	0.16
I	7.85 ±0.4	8.6 ±0.2	11	0.38157	0.08
II	21.8 ±0.9	20.9 ±0.5	5	0.38136	0.15
II	22.1 ±0.9	20.9 ±0.5	12	0.38203	0.46

[1]Capsule burnups as inferred from pellet radiochemistry. The burnup is peaked at the capsule ends so the capsule average is generally not the same as an individual pellet burnup.
[2]Monte Carlo N-Particle

Table 6.3
Fuel Pin Cladding Inner Diameter

APT Irradiation Phase	Met. Mount ID Number	Capsule	Fuel Pin	Clad Inner Diameter (inches)	Uncertainty in Inner Diameter (mils)
I	6139	1	2	0.32961	0.68
I	6140	1	2	0.32934	0.53
I	6141	1	2	0.32960	0.86
II	6143	9	12	0.33034	0.71
II	6144	9	12	0.33134	0.86
II	6145	2	5	0.32996	0.55
II	6146	2	5	0.33005	0.45

The cladding inner diameter is shown as a function of burnup in the lower half of Figure 6.1. Even with the known uncertainties, it is obvious that the Zircaloy inner and outer diameters are increasing as the irradiation proceeds. At a burnup of 21 GWd/MT, from the Figure 6.1 values for both inner and outer clad diameters, it is obvious that the clad has been radially displaced ~0.4 mils outward from its preirradiation value.

The enlarged photographs of the metallographic mounts reveal slight concentricity differences in the inner and outer diameters of the clad. There are approximately 40 measurements per mount, and the standard deviation in the clad thickness ranges from 0.21 to 0.42 mils over the seven mounts. Nevertheless, when all the measurements for all mounts are considered (over 280 observations), the computed mean clad thickness is 0.02578 inches with an uncertainty of 0.12 mils.

For the mean thickness plus/minus one sigma, this gives a range of 0.02566 to 0.02590 inches for the observed clad thickness. The construction tolerances for the cladding allow a range of 0.0255 to 0.0260 inches for this thickness. The preirradiation values for the Zircaloy clad inner and outer diameters (for Fuel Pins 2, 5, 11, and 12 in Table 2.1) suggest that the clad thickness should range from 0.0256 to 0.0259 inches. This basically substantiates the scale and measurements made from the enlarged photographs of the metallographic mounts.

6.2.3 Fuel-to-Clad Radial Gap

Reviewing the metallographic mounts illustrated in Chapter 5, the appearance of the fuel is normal (with cracks caused by high thermal stresses during the ATR operation and thermal cycling, i.e., startups and shutdowns).

Under hot-cell conditions, there is less than 1°C difference between the capsule surface and the fuel centerline, and the capsule temperature is within 25°C of the hot-cell ambient conditions. Due to the low capsule temperatures, there is little thermal expansion of the capsule components; thus, existing cracks within the fuel and the peripheral gap (between the fuel and the cladding) both expand. During ATR operation, high temperatures within the fuel and the resulting thermal expansion tend to close the internal cracks and peripheral gap.

From the enlarged photographs of the metallographic mounts, the free area within the fuel pin can be estimated by measuring the gap and crack dimensions. This free area does not include the porosity within the fuel or the “pullouts” in the mounts (which are caused by loss of friable material during preparation of the mounts).

Generally, the portion of the free area within the cracks (at hot-cell conditions) for these seven metallographic mounts is greater than the free area portion in the peripheral gap. The total free area can be used to calculate an “adjusted” peripheral gap (that is, an adjusted gap between the fuel and clad, which includes all the free area within the fuel pin). This approach is consistent with the manner in which fuels codes treat the gap and cracks within the fuel pin. This adjusted gap can then be compared with the predictions of the fuels codes (such as CARTS).

The adjusted fuel-to-clad peripheral gap and uncertainty for each metallographic mount are listed in Table 6.4.

The fuel-to-clad radial gap is shown as a function of burnup in Figure 6.2. Prior to irradiation, the construction tolerances allow a range in the radial gap from 1.00 to 1.75 mils. This range is illustrated at zero burnup.

As shown in Figure 6.2, the gap at ~8.4 GWd/MT burnup is greater than the gap at BOL, and at ~21 GWd/MT burnup, the gap is approximately the same as the preirradiation value. This behavior is prototypic of commercial fuel; that is, the fuel densifies (i.e., shrinks in volume) in the earlier phase of irradiation.

Hodge discusses the fuel densification and swelling phenomena in Chapter 6 (Ref 11) of his white paper on fission gas release and fuel swelling. Also, an excellent graphical presentation of commercial fuel (Siemens) densification and swelling is given in Figure 6.1 of Reference 11. In general, densification is very rapid in the first 10 GWd/MT of burnup and is finished by 10–15 GWd/MT.

Table 6.4
Fuel to Clad Radial Gap

APT Irradiation Phase	Met. Mount ID Number	Capsule	Fuel Pin	Adjusted Gap(mils)	Uncertainty in Gap(mils)
I	6139	1	2	2.77	0.28
I	6140	1	2	2.50	0.30
I	6141	1	2	1.98	0.36
II	6143	9	12	1.30	0.21
II	6144	9	12	1.23	0.21
II	6145	2	5	1.67	0.20
II	6146	2	5	1.50	0.19

Fuel densification and swelling are essentially competing effects; early in the irradiation, densification dominates and the fuel volume shrinks, but after densification is complete, swelling continues in direct proportion to the burnup.

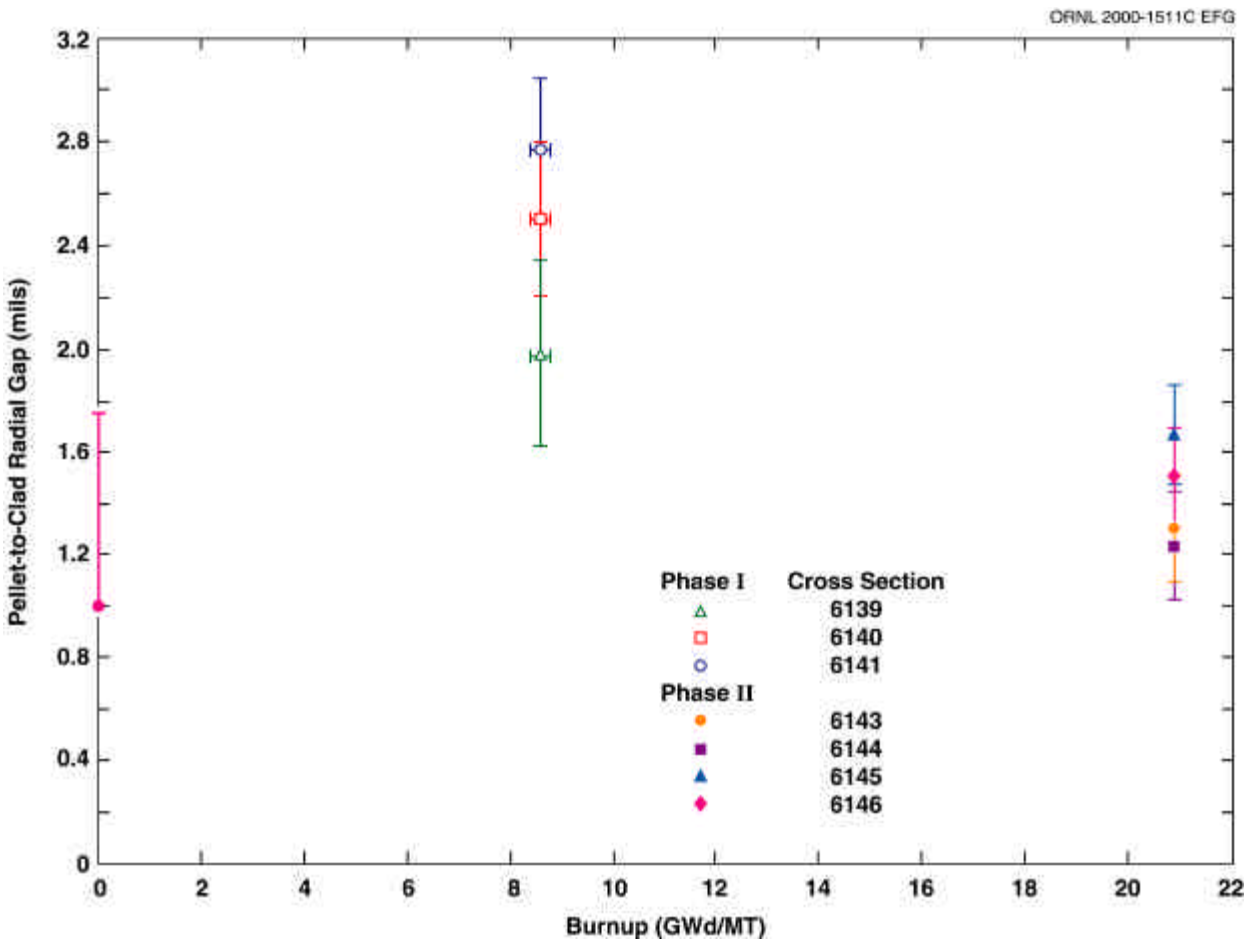

Figure 6.2 Cold radial pellet-to-clad gaps in APT MOX fuel pins.

6.2.4 Fuel Pellet Outer Diameter

Given the Zircaloy cladding inner diameter (from Section 6.2.2) and the "adjusted" peripheral gap between the fuel and the clad (from Section 6.2.3), the fuel outer diameter (i.e., in the absence of internal cracking) can be calculated via a difference of the two quantities.

The fuel pellet outer diameter and uncertainty for each metallographic mount are given in Table 6.5.

The range of pellet outer diameters is shown as a function of burnup in Figure 6.3. Prior to irradiation, the construction tolerances allow a range in the pellet diameter of 0.3260 to 0.3270 inches. This is the initial range shown at zero burnup.

Figure 6.3 again demonstrates the initial fuel densification and subsequent dominance of the fuel swelling. After the initial densification phase, pellet expansion (which is directly proportional to

burnup) will continue until the irradiation is stopped.

Table 6.5 Fuel Outer Diameter					
APT Irradiation Phase	**Met. Mount ID. Number**	**Capsule**	**Fuel Pin**	**Fuel Pellet Outer Dia.(inches)**	**Uncertainty in Diameter(mils)**
I	6139	1	2	0.32407	0.88
I	6140	1	2	0.32434	0.80
I	6141	1	2	0.32563	1.12
II	6143	9	12	0.32774	0.82
II	6144	9	12	0.32888	0.95
II	6145	2	5	0.32662	0.68
II	6146	2	5	0.32705	0.60

6.2.5 Conclusions from Dimensional Inspections of the Metallographic Mounts

Two primary conclusions can be drawn from the PIE metrological results and the dimensional inspections of the fuel pin metallographic mounts:

1. Outward expansion of the fuel pin Zircaloy clad appears conclusive. The degree of growth is within the expected range (0.1%–0.2%) for these operating conditions. (A discussion of irradiation-induced clad growth is included in Reference 19.) Clad expansion must be included in the predictive analyses of the fuels codes (and especially the CARTS analyses) for higher APT burnups (30 GWd/MT and above).

2. Fuel behavior (ergo cracking), densification, and swelling of the mixed uranium-plutonium oxide (MOX) test fuel appear to be normal and prototypic of commercial fuel. The appropriate degree of fuel densification will be included in future CARTS predictive analyses of higher APT burnups. An assessment of the fuel densification is given in Section 6.3.

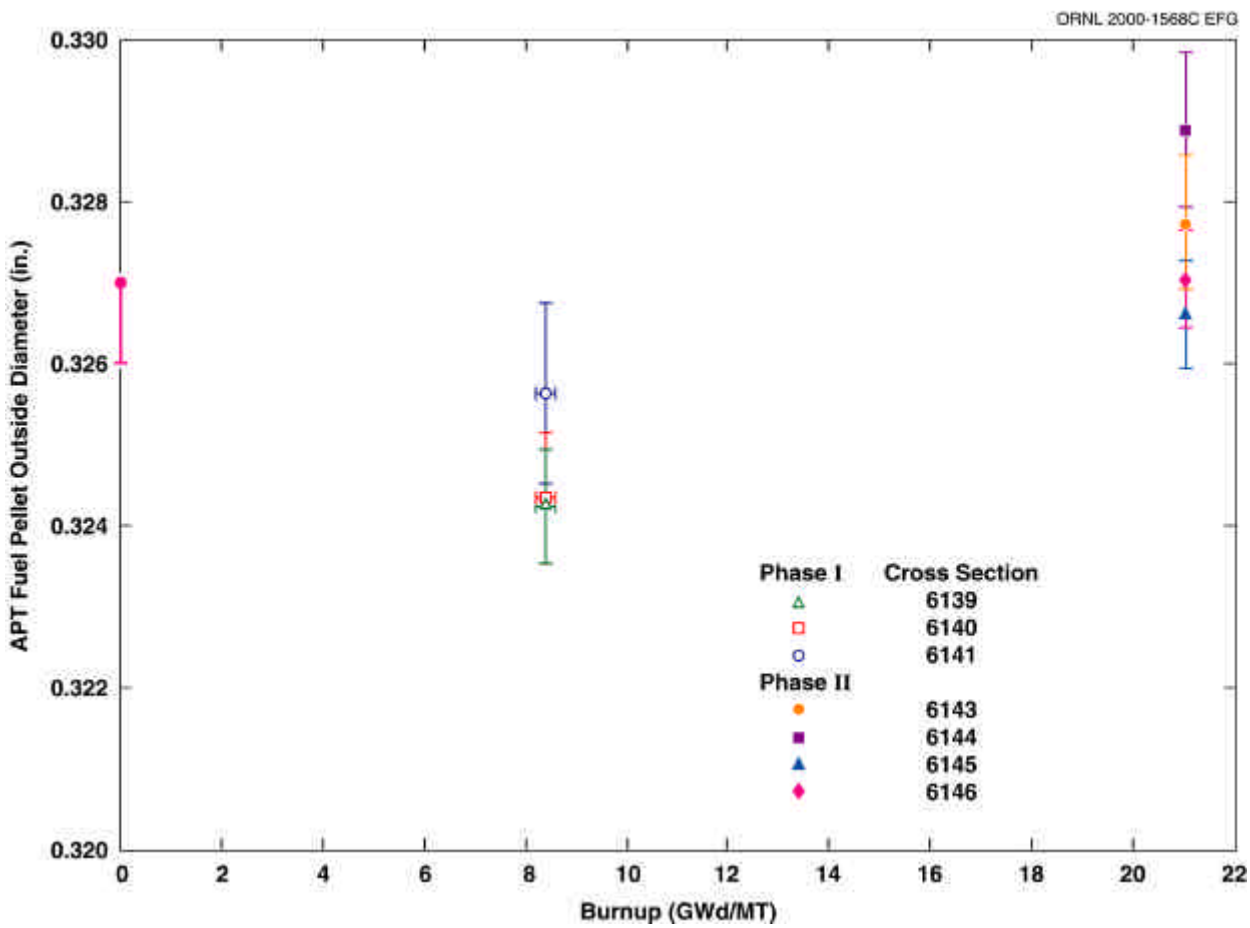

Figure 6.3 Cold pellet outer diameter in APT MOX fuel pins.

6.3 Assessment of APT Fuel Densification and Swelling

The CARTS code employs two fuel densification and swelling models (as selected by user input):

1. The first model is from the ESCORE code (Reference 17), which is an industry-derived code approved by the U.S. Nuclear Regulatory Commission (NRC).
2. The second model is from the FRAPCON-3 code (Reference 18), which is the NRC's audit code.

Both models have been used in previous CARTS safety analyses for the APT MOX experiments.

It is explicitly assumed that both models are appropriate to analyze the APT fuel behavior since both models have been developed and verified via an extensive European and domestic data

base. The only degree of freedom in applying these models to the APT Phase-I and Phase-II irradiations is the degree of fuel densification assumed.

Given the APT fuel production conditions (high sintering temperature and a long sintering time) at Los Alamos National Laboratory, it was initially believed that an upper limit of ~0.5% fuel densification was appropriate for the APT fuel; subsequently, 0.0% and 0.5% fuel densification were assumed as bounds for the APT Phase-IV safety analyses (Reference 12).

The data developed in Sections 6.2.3 and 6.2.4 now permit an estimate of the fuel densification (based on PIE observations) that is appropriate in applying the ESCORE and FRAPCON models in CARTS in describing the actual fuel behavior.

To determine the appropriate densification values, the CARTS code has been employed in simulating the APT Phase-I and Phase-II irradiations. For these simulations, a fuel densification and swelling model (either ESCORE or FRAPCON) was selected, and, then, the ultimate fuel densification was varied until a best-fit to the experimental data (i.e., Figures 6.2 and 6.3) was determined. For the ESCORE model, this best-fit value is 2.0% with densification complete by 10 GWd/MT. For the FRAPCON model, the best-fit value is 1.5% with densification complete by 5 GWd/MT.

The results of these simulations and model predictions using these values are illustrated in Figures 6.4 and 6.5. (Currently CARTS cannot evaluate clad creep; the creep-adjusted gap in Figure 6.4 is the observed gap minus clad creep). Not only is the initial densification phase adequately predicted, but the continuing and subsequent fuel swelling is also adequately predicted.

From Hodge's (Reference 11) review of the literature and as demonstrated in Figure 6.1 of his report, fuel densification of 1.0%–2.0% is prototypic of commercial fuel.

Future predictive CARTS calculations (for burnups of 30 GWd/MT and greater) will assume a fuel densification of 1.5% and 2.0%, respectively, for the FRAPCON and ESCORE models. These values are higher than was assumed in the Phase-IV safety analyses (Reference 12); however, the lower densification assumed (0.0% and 0.5%) in the safety analyses yields higher fuel swelling in the Phase-IV calculations, which is appropriately conservative. Therefore, the realistic predictions will employ higher fuel densification values than did the calculations presented in Reference 12, which are considered conservative as appropriate for the Phase-IV irradiation extension safety analyses.

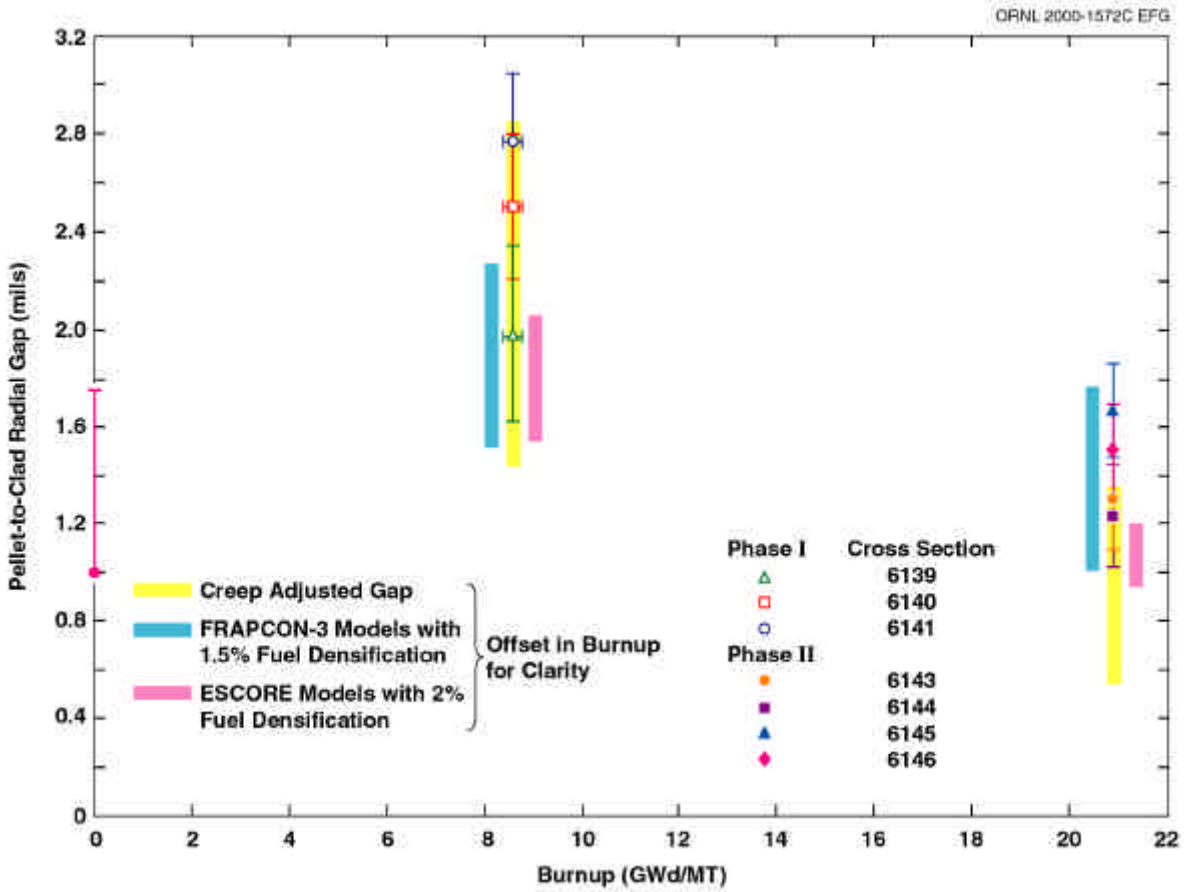

Figure 6.4 Cold radial pellet-to-clad gaps in APT MOX fuel pins compared with ESCORE and FRAPCON model results.

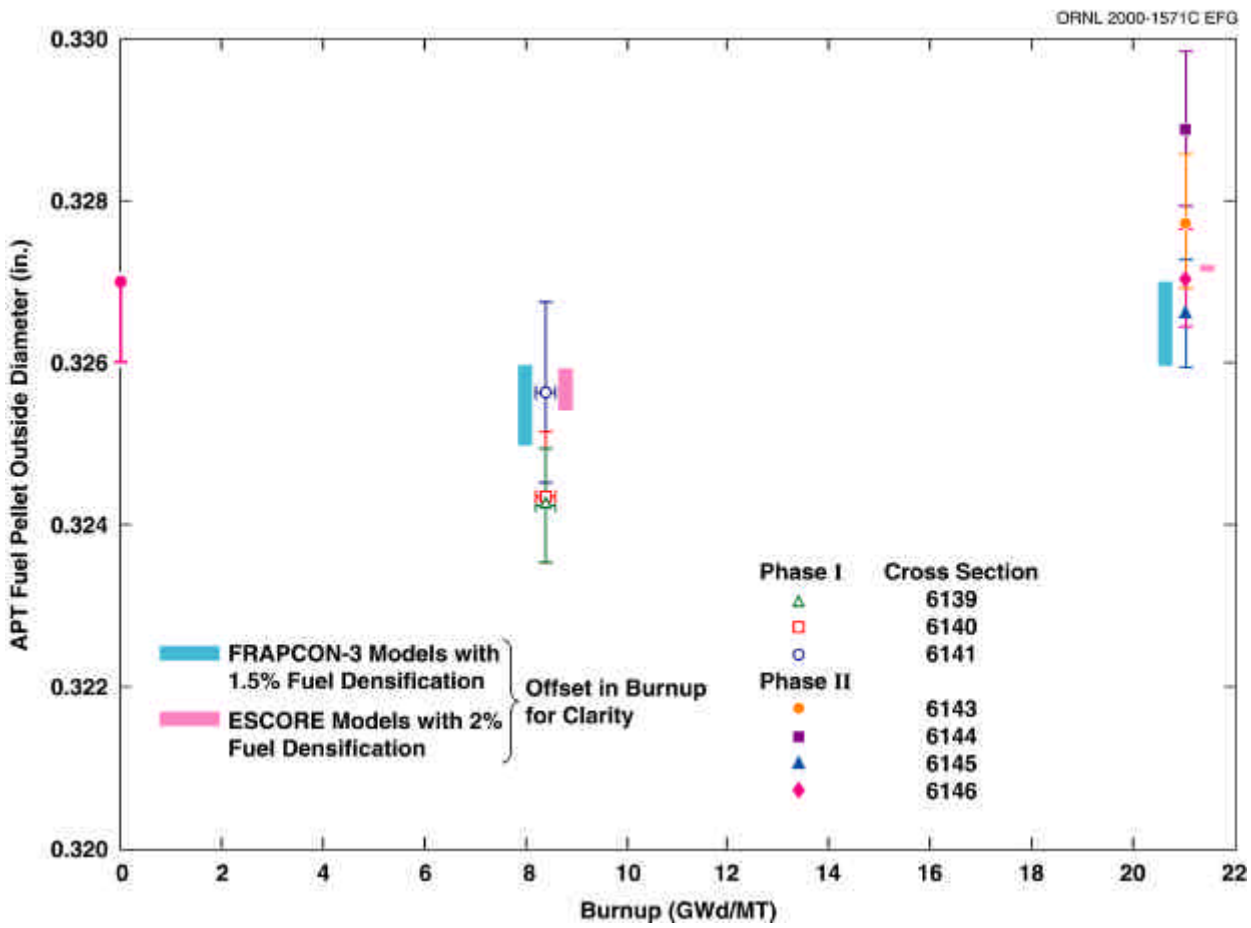

Figure 6.5 Cold pellet outer diameter in APT MOX fuel pins compared with ESCORE and FRAPCON model results.

7. RADIOCHEMISTRY RESULTS

7.1 Introduction

Fuel Pin 5 (untreated fuel) was segmented as shown in Figures 7.1 and 7.2. Table 7.1 details the disposition of the specimens (metallographic tasks are detailed in Chapter 5). Gallium tracking was the primary analysis concern for this pin as it contains the untreated MOX.

Fuel Pin 12 (treated) was segmented as shown in Figures 7.3 and 7.4. Table 7.2 details the disposition of the specimens. Ductility testing is the primary analysis concern for this pin.

A total of 12 specimens were sent to the Radioactive Materials Analytic Laboratory (RMAL) for analysis. One specimen was lost during preparation. See Table 7.3 for specimen summary details.

7.2 Gallium Analysis Results

The results of the gallium analysis are shown in Table 7.4. Past analysis of unirradiated cladding materials indicated that clad gallium levels were in the range of a few tenths of a ppm [Ref 13]. Thus, the results do not indicate any significant transfer of gallium to the clad. In addition, the pellets have gallium levels in the initial (unirradiated) range [Ref 10].

A bounding estimate of the maximum possible gallium transfer to the clad can be determined by examining pellet 15 in both fuel pins. Specimens are available for pellet 15, the clad around pellet 15, and the end plug below pellet 15. The total gallium in these specimens may be summed and the conservative assumption made that the clad started out with zero gallium and its final gallium content is due solely to transfer from the pellet. Doing so leads to the conclusion that no more than about 14% of the gallium in the fuel pellet could have been transferred to the clad. This logic is summarized in Table 7.5.

A source of uncertainty for the clad gallium analysis is that small particles of fuel may have adhered to the clad, thus skewing the clad gallium analysis to a higher value. The specimens were lightly brushed after fuel removal to avoid disturbing the clad inner surface. This brushing was insufficient to remove any strongly adhering particles. This further supports the conclusion that any gallium transfer to the bulk clad was insignificant.

It should also be noted that improvements in the removal of fission products (primarily barium) from the dissolved specimens prior to gallium measurements have eliminated the analytical difficulties that plagued the previous PIE work [13].

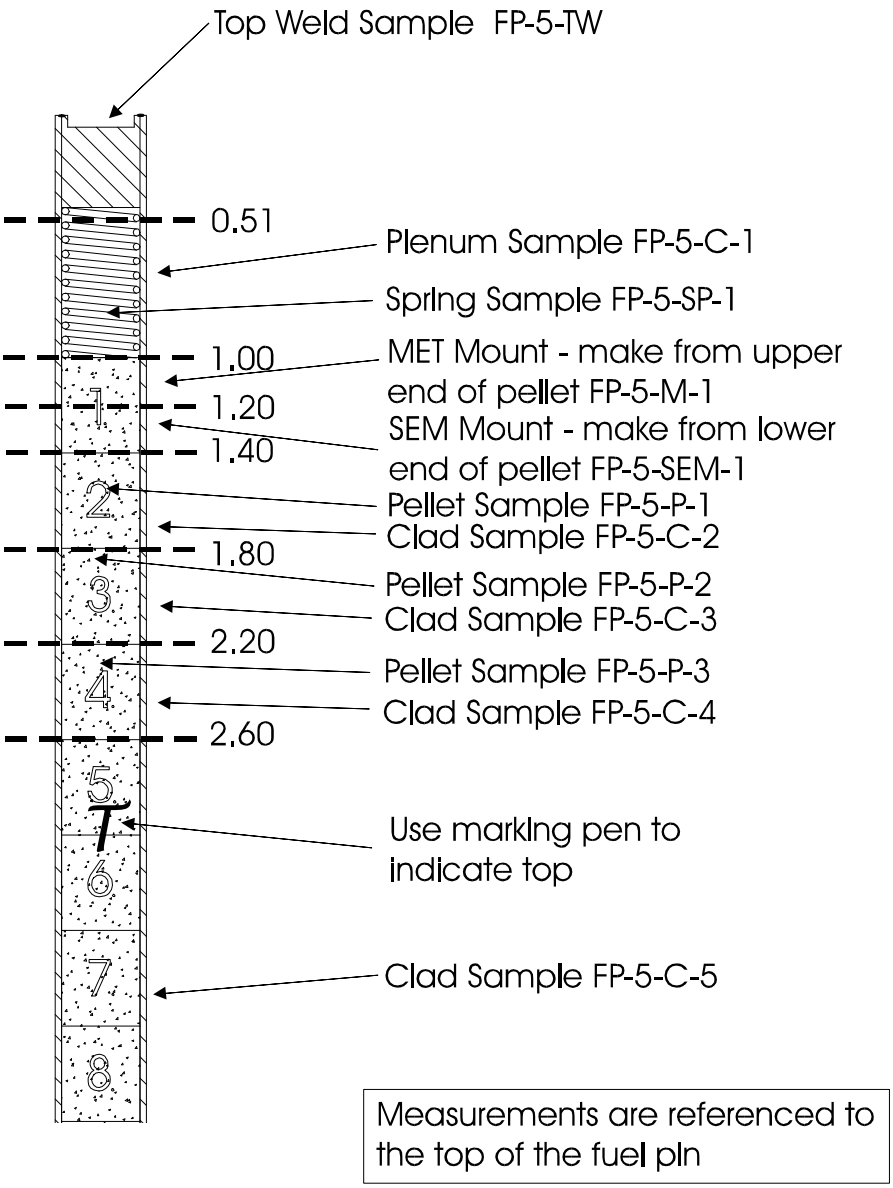

Figure 7.1 Fuel Pin 5 Upper half cutting guide.

Detailed Cutting Guide for Bottom Half of Fuel Pin 5

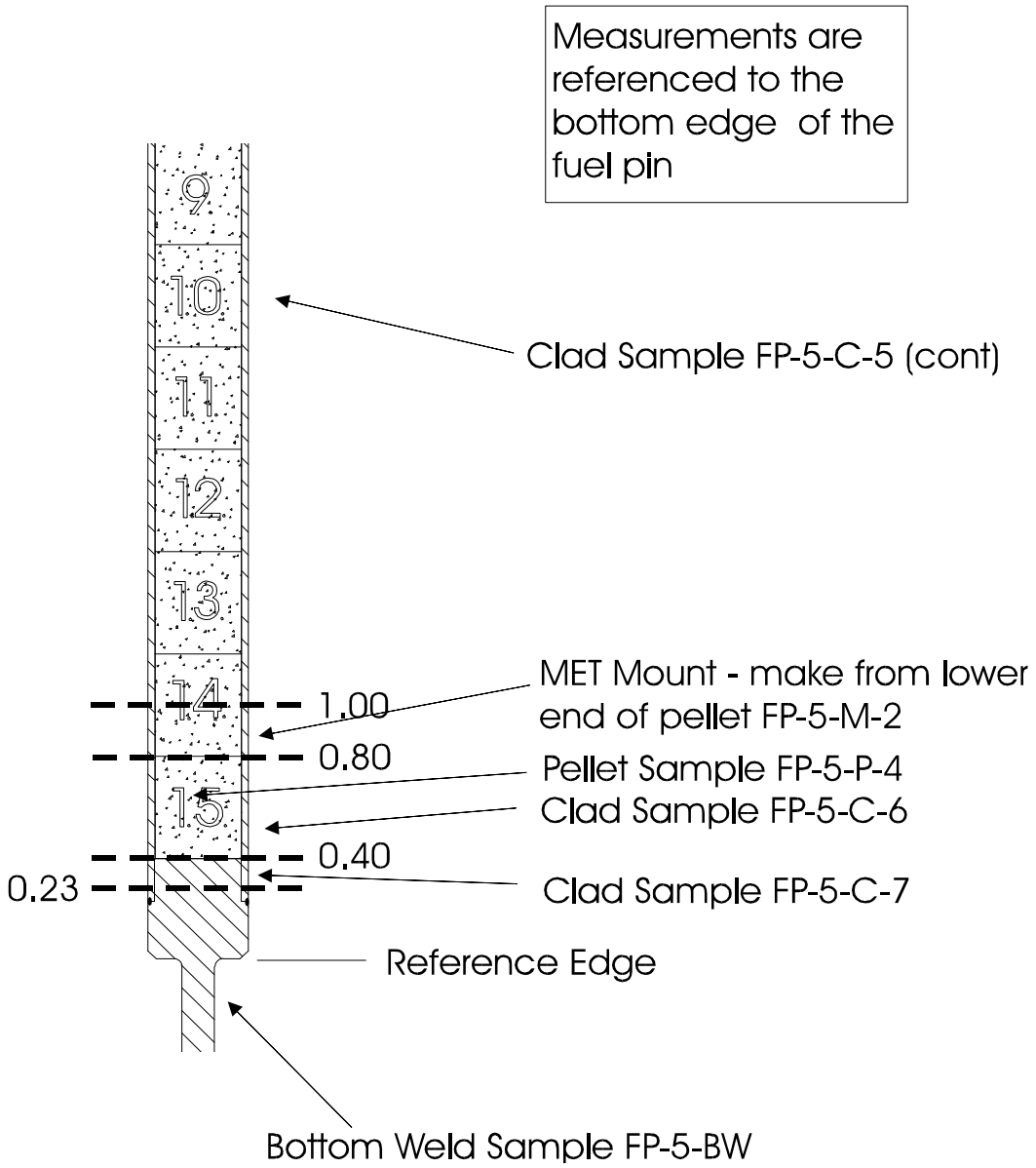

Figure 7.2 Fuel Pin 5 bottom half cutting guide.

TABLE 7.1 Fuel Pin 5 Sampling			
Specimen	**Location**	**Interest**	**Disposition**
FP-5-C-1	Plenum Clad	Ga Analysis	Radiochemistry
FP-5-C-2	Pellet 2 Clad	Reserve	Archive
FP-5-C-3	Pellet 3 Clad	Ga Analysis	Radiochemistry
FP-5-C-4	Pellet 4 Clad	Ga Analysis	Radiochemistry
FP-5-C-5	Pellets 5-13 Clad	Ductility Testing	Archive (fuel left in clad)
FP-5-C-6	Pellet 15 Clad	Ga Analysis	Radiochemistry
FP-5-C-7	Bottom Cap	Ga Analysis	Radiochemistry
FP-5-P-1	Pellet 2	Burnup & Ga Analysis	Radiochemistry
FP-5-P-2	Pellet 3	Ga Analysis	Radiochemistry
FP-5-P-3	Pellet 4	Reserve	Archive
FP-5-P-4	Pellet 15	Ga Analysis	Radiochemistry
FP-5-TW	Top Weld	Reserve	Archive
FP-5-BW	Bottom Weld	Reserve	Archive
FP-5-SP-1	Spring	Reserve	Archive
FP-5-M-1	Top of Pellet/Clad 1	Microstructure	Metallography
FP-5-M-2	Bottom of Pellet/Clad 14	Microstructure	Metallography
FP-5-SEM-1	Bottom of Pellet/Clad 1	Pellet/Clad interaction	SEM[1]

[1]Two or more thin wafers may be cut from this specimen and prepared as mounts, with the mount displaying the best surface to be used for the actual SEM analysis.

Detailed Cutting Guide for Top Half of Fuel Pin 12

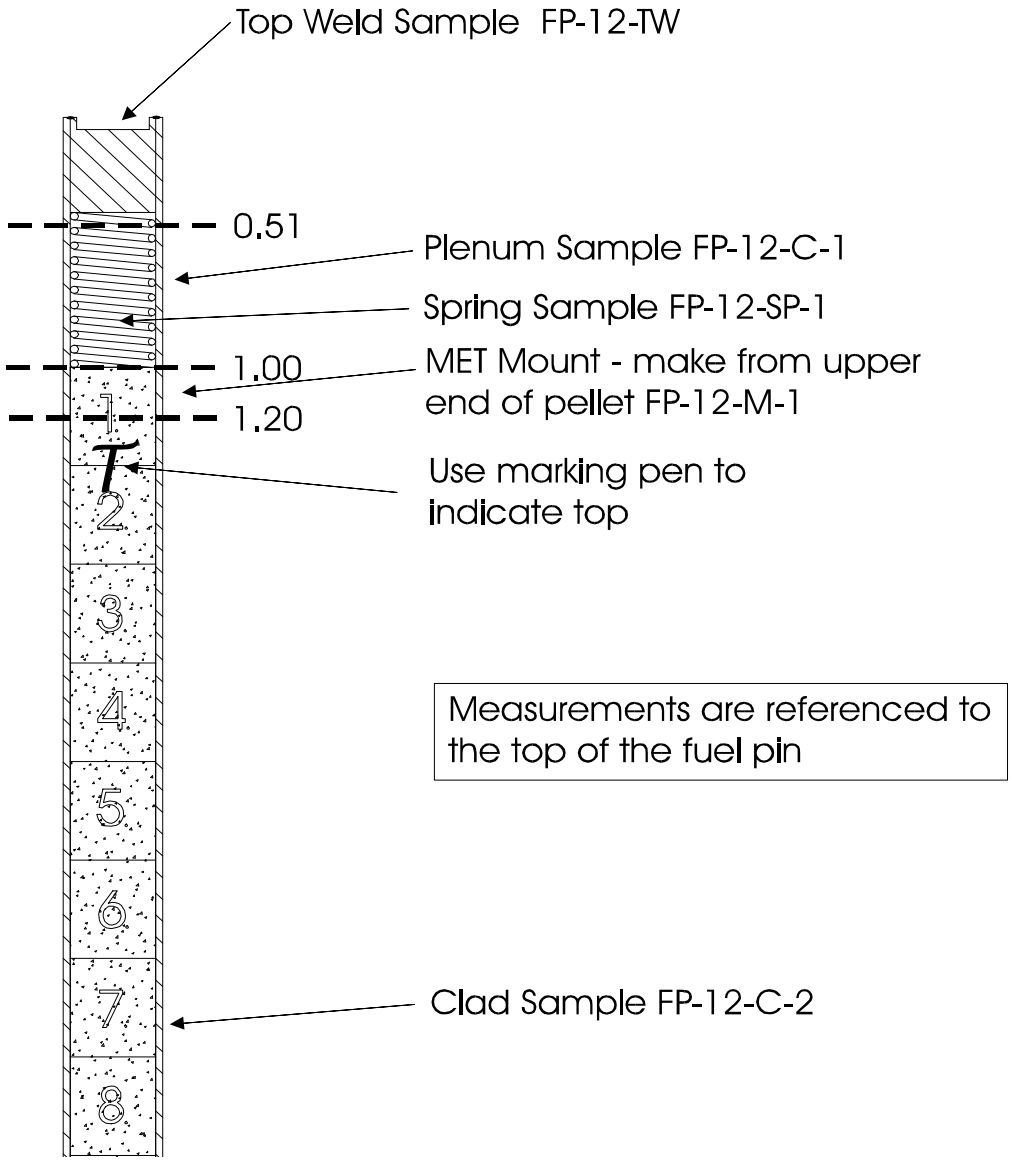

Figure 7.3 Fuel Pin 12 top half cutting guide.

Detailed Cutting Guide for Bottom Half of Fuel Pin 12

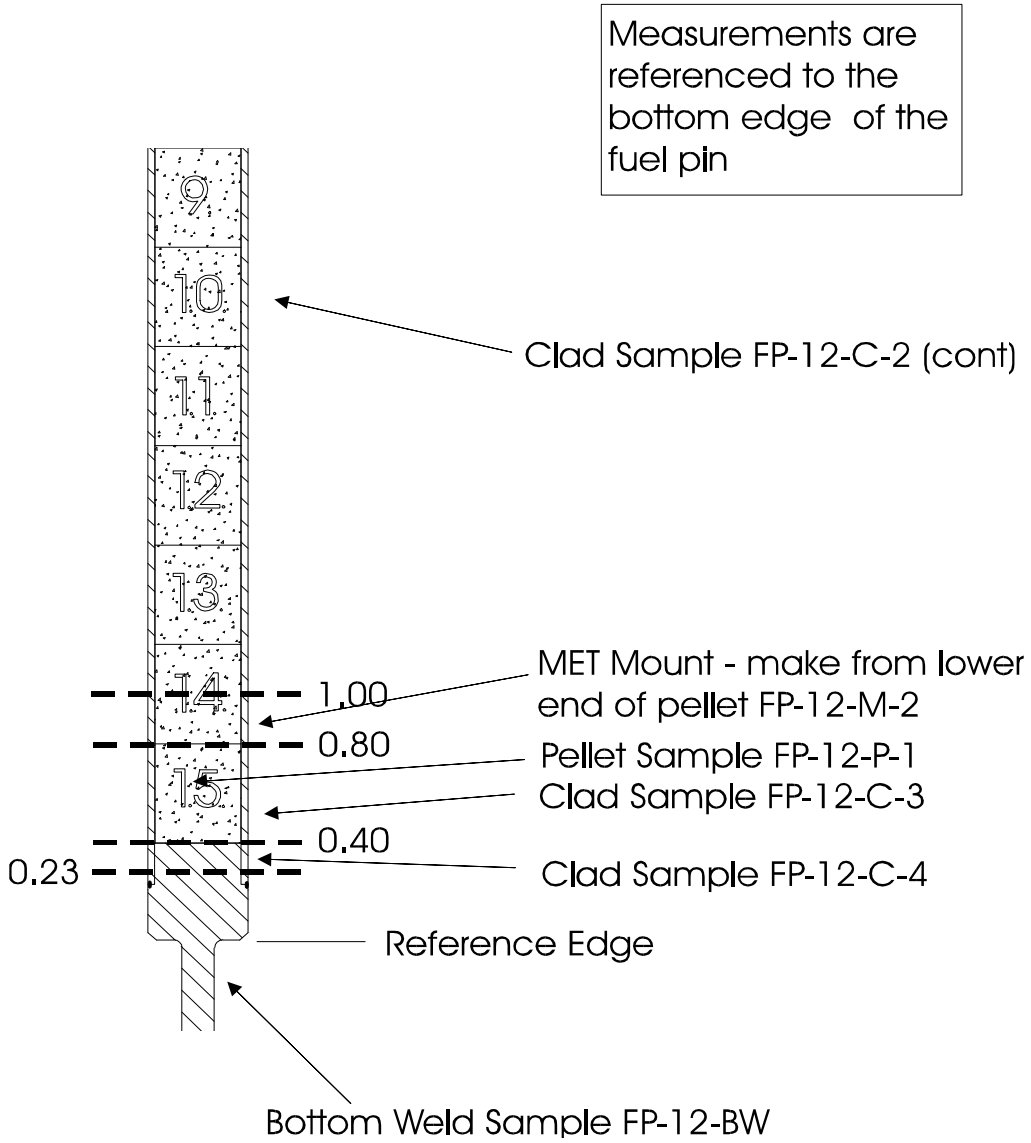

Figure 7.4 Fuel Pin 12 bottom half cutting guide.

TABLE 7.2 Fuel Pin 12 Sampling			
Specimen	**Location**	**Interest**	**Disposition**
FP-12-C-1	Plenum Clad	Ga Analysis	Radiochemistry
FP-12-C-2	Pellets 5-13 Clad	Ductility Testing	Archive (fuel left in clad)
FP-12-C-3	Pellet 15 Clad	Ga Analysis	Radiochemistry
FP-12-C-4	Bottom Cap	Ga Analysis	Radiochemistry
FP-12-P-1	Pellet 15	Burnup & Ga Analysis	Radiochemistry
FP-12-TW	Top Weld	Reserve	Archive
FP-12-BW	Bottom Weld	Reserve	Archive
FP-12-SP-1	Spring	Reserve	Archive
FP-12-M-1	Top of Pellet/Clad 1	Microstructure	Metallography
FP-12-M-2	Bottom of Pellet/Clad 14	Microstructure	Metallography

TABLE 7.3 Summary of RMAL Analysis Specimens			
Specimen	**Location**	**Interest**	**Disposition**
FP-5-C-1	Plenum Clad	Ga Analysis	Radiochemistry
FP-5-C-3	Pellet 3 Clad	Ga Analysis	Radiochemistry
FP-5-C-4	Pellet 4 Clad	Ga Analysis	Radiochemistry
FP-5-C-6	Pellet 15 Clad	Ga Analysis	Radiochemistry
FP-5-C-7	Bottom Cap	Ga Analysis	Radiochemistry
FP-5-P-1	Pellet 2	Burnup & Ga Analysis	Radiochemistry
FP-5-P-2	Pellet 3	Ga Analysis	Radiochemistry (Lost in preparation)
FP-5-P-4	Pellet 15	Ga Analysis	Radiochemistry
FP-12-C-1	Plenum Clad	Ga Analysis	Radiochemistry
FP-12-C-3	Pellet 15 Clad	Ga Analysis	Radiochemistry
FP-12-C-4	Bottom Cap	Ga Analysis	Radiochemistry
FP-12-P-1	Pellet 15	Burnup & Ga Analysis	Radiochemistry

TABLE 7.4
Results of Gallium Analysis

Specimen Number	Mass (grams)	PPM Gallium (mass)	Uncertainty (±)
Fuel Pin 5 Specimens			
FP-5-C-1	1.9838	0.284	0.057
FP-5-C-3	1.2158	0.247	0.049
FP-5-C-4	1.1874	0.303	0.061
FP-5-C-6	1.1637	0.310	0.062
FP-5-C-7	1.8297	0.459	0.092
Clad Average		*0.321*	
FP-5-P-1	5.2829	2.05	0.41
FP-5-P-4	5.3258	2.31	0.46
Pellet Average		*2.18*	
Fuel Pin 12 Specimens			
FP-12-C-1	1.4792	0.480	0.096
FP-12-C-3	1.1600	0.580	0.110
FP-12-C-4	1.7129	0.238	0.048
Clad Average		*0.433*	
FP-12-P-1	4.9651	1.34	0.27

TABLE 7.5 Bounding Gallium Mass Balance (Assumes Clad Starts with Zero Gallium)			
Specimen Number	**Mass (grams)**	**PPM Gallium (mass)**	**Gallium Mass (µgrams)**
Gallium Balance Fuel Pin 5 Pellet 15			
FP-5-P-4	5.3258	2.310	12.30
FP-5-C-6	1.1637	0.310	0.36
FP-5-C-7	1.8297	0.459	0.84
Total Gallium			13.50
Maximum Transfer to Clad (Zero Initial Gallium)			8.9%
Gallium Balance Fuel Pin 12 Pellet 15			
FP-12-P-1	4.9651	1.340	6.65
FP-12-C-3	1.1600	0.580	0.67
FP-12-C-4	1.7129	0.238	0.41
Total Gallium			7.73
Maximum Transfer to Clad (Zero Initial Gallium)			14%

7.3 Radiochemical Determination of Fuel Burnup

Three pellet specimens, FP-5-P-1, FP-5-P-4, and FP-12-P-1, were analyzed for burnup essentially utilizing the method detailed in *ASTM E 321 Standard Test for Atom Percent Fission in Uranium and Plutonium Fuel (Neodymium-148 Method)*. A correction was applied to the ^{148}Nd yield to include the ^{241}Pu fission fraction (approximately 0.061) and to compensate for the conversion of ^{147}Nd to ^{148}Nd (approximately 2% of the ^{148}Nd). The overall correction was small, approximately 3%.

The calculated burnups vs the radiochemistry measured burnups for specific pellet locations are shown in Table 7.6. As can be seen, excellent agreement was obtained. The fuel pin average burnup (both pins) was calculated by the MCNP code to be 20.9 GWd/MT.

The detailed results are shown in Tables 7.7 through 7.9. The estimated accuracy of the radiochemistry burnup is approximately 4%; the estimated accuracy of the calculations (MCNP and FRAPCON codes) are 2.5%

TABLE 7.6
Fuel Burnup

Specimen	Pellet Location	Calculated Burnup (GWd/MT)	Radiochemistry Burnup (GWd/MT)
FP-5-P-1	2	22.3	23.3
FP-5-P-4	15	21.2	22.0
FP-12-P-1	15	21.2	22.5

TABLE 7.7
FP-5-P-1 Burnup

Burn-up Data

FP-5-P-1

5.2829 g fuel pellet

N_A = 6.02E+23 atoms/mole

Uranium	atom %	Pu	atom %	Nd	atom ratio		atom %	wt.%
				142/143	0.0841 +/- 0.0003	^{142}Nd	2.0854%	2.0421%
				143/143	1.0000 +/- 0.0000	^{143}Nd	24.7967%	24.4530%
^{233}U	0.0000 +/- 0.0001	^{238}Pu	0.265 +/- 0.0030	144/143	0.8776 +/- 0.0029	^{144}Nd	21.7616%	21.6102%
^{234}U	0.0010 +/- 0.0000	^{239}Pu	63.485 +/- 0.0363	145/143	0.7410 +/- 0.0019	^{145}Nd	18.3743%	18.3736%
^{235}U	0.1576 +/- 0.0001	^{240}Pu	30.471 +/- 0.0008	146/143	0.6641 +/- 0.0031	^{146}Nd	16.4675%	16.5805%
^{236}U	0.0173 +/- 0.0004	^{241}Pu	4.495 +/- 0.0316	148/143	0.4205 +/- 0.0027	^{148}Nd	10.4270%	10.6428%
^{238}U	99.8234 +/- 0.0006	^{242}Pu	1.283 +/- 0.0085	150/143	0.2455 +/- 0.0039	^{150}Nd	6.0876%	6.2977%
		^{244}Pu	0.0001 +/- 0.0001					
Total (mg/g)[1]	733 +/- 0.20%	(mg/g)[1]	4.82 +/- 0.26%	(mg/g)[1]	1.82 +/- 0.43%		100.0000%	100.0000%

[1] Concentration in sample with units of mg of element per gram of sample.

$^{235}U_R$	1.141 mg/g	$^{239}Pu_R$	3.055 mg/g	$^{241}Pu_R$	0.218 mg/g
$^{235}U_R$	2.92E+18 atoms/g	$^{239}Pu_R$	7.69E+18 atoms/g	$^{241}Pu_R$	5.45E+17 atoms/g
$^{238}U_R$	731.726 mg/g	$^{240}Pu_R$	1.472 mg/g	^{148}Nd:	0.194 mg/g
$^{238}U_R$	1.85E+21 atoms/g	$^{240}Pu_R$	3.69E+18 atoms/g	^{148}Nd:	7.89E+17 atoms/g produced

0.017 Nd-148 atoms per Pu fission (corrected for Pu-239 and Pu-241 fission fraction along with Nd-147 capture)

$(^{235}U+^{238}U+^{239}Pu+^{240}Pu+^{241}Pu)_R$	1.87E+21	atoms/g remaining (dominate contributors)
$(^{235}U+^{239}Pu)_C$	4.64E+19	atoms/g consumed (assume dominated by Pu)

Burnup =	**2.43%**
GWd/MT=	**23.29**

TABLE 7.8
FP-5-P-4 Burnup

Burn-up Data

FP-5-P-4

5.3258 g fuel pellet

N_A = 6.02E+23 atoms/mole

Uranium	atom %	Pu	atom %	Nd	atom ratio		atom %	wt.%
				142/143	0.0503 +/- 0.0002	^{142}Nd	1.2805%	1.2538%
				143/143	1.0000 +/- 0.0000	^{143}Nd	25.4582%	25.1018%
^{233}U	0.0000 +/- 0.0000	^{238}Pu	0.2051 +/- 0.0332	144/143	0.8463 +/- 0.0006	^{144}Nd	21.5453%	21.3923%
^{234}U	0.0010 +/- 0.0000	^{239}Pu	66.1353 +/- 0.0661	145/143	0.7315 +/- 0.0082	^{145}Nd	18.6227%	18.6193%
^{235}U	0.1643 +/- 0.0014	^{240}Pu	28.8916 +/- 0.0316	146/143	0.6399 +/- 0.0051	^{146}Nd	16.2907%	16.4002%
^{236}U	0.0167 +/- 0.0007	^{241}Pu	4.0855 +/- 0.0003	148/143	0.4184 +/- 0.0015	^{148}Nd	10.6517%	10.8706%
^{238}U	99.8151 +/- 0.0019	^{242}Pu	0.6825 +/- 0.0010	150/143	0.2416 +/- 0.0035	^{150}Nd	6.1507%	6.3621%
		^{244}Pu	0.0000 +/- 0.0000					
Total (mg/g)[1]	848 +/- 0.31%	(mg/g)[1]	6.32 +/- 1.12%	(mg/g)[1]	1.95 +/- 0.51%		100.0000%	100.0000%

[1] Concentration in sample with units of mg of element per gram of sample.

$^{235}U_R$	1.376 mg/g	$^{239}Pu_R$	4.173 mg/g	$^{241}Pu_R$	0.260 mg/g
$^{235}U_R$	3.52E+18 atoms/g	$^{239}Pu_R$	1.05E+19 atoms/g	$^{241}Pu_R$	6.49E+17 atoms/g
$^{238}U_R$	846.475 mg/g	$^{240}Pu_R$	1.831 mg/g	^{148}Nd:	0.212 mg/g
$^{238}U_R$	2.14E+21 atoms/g	$^{240}Pu_R$	4.59E+18 atoms/g	^{148}Nd:	8.63E+17 atoms/g produced

0.017 Nd-148 atoms per Pu fission (corrected for Pu-239 and Pu-241 fission fraction along with Nd-147 capture)

$(^{235}U+^{238}U+^{239}Pu+^{240}Pu+^{241}Pu)_R$	2.16E+21	atoms/g remaining (dominate contributors)
$(^{235}U+^{239}Pu)_C$	5.08E+19	atoms/g consumed (assume dominated by Pu)

Burnup =	**2.30%**
GWd/MT=	**22.04**

TABLE 7.9
FP-12-P-1 Burnup

Burn-up Data

FP-12-P-1

4.9651 g fuel pellet

N_A = 6.02E+23 atoms/mole

Uranium	atom %	Pu	atom %	Nd	atom ratio		atom %	wt.%
				142/143	**0.0477 +/- 0.0005**	^{142}Nd	1.1986%	1.1733%
				143/143	**1.0000 +/- 0.0000**	^{143}Nd	25.1275%	24.7716%
^{233}U	**0.0000 +/- 0.0000**	^{238}Pu	**0.2096 +/- 0.0300**	144/143	**0.8519 +/- 0.0031**	^{144}Nd	21.4061%	21.2506%
^{234}U	**0.0010 +/- 0.0007**	^{239}Pu	**65.8241 +/- 0.0399**	145/143	**0.7450 +/- 0.0014**	^{145}Nd	18.7200%	18.7135%
^{235}U	**0.1630 +/- 0.0014**	^{240}Pu	**29.0792 +/- 0.0078**	146/143	**0.6553 +/- 0.0012**	^{146}Nd	16.4661%	16.5740%
^{236}U	**0.0161 +/- 0.0001**	^{241}Pu	**4.1444 +/- 0.0143**	148/143	**0.4287 +/- 0.0066**	^{148}Nd	10.7722%	10.9917%
^{238}U	**99.8192 +/- 0.0022**	^{242}Pu	**0.7427 +/- 0.0035**	150/143	**0.2511 +/- 0.0047**	^{150}Nd	6.3095%	6.5253%
		^{244}Pu	**0.0000 +/- 0.0000**					
Total (mg/g)[1]	**795 +/- 0.27%**	(mg/g)[1]	**4.69 +/- 0.13%**	(mg/g)[1]	**1.84 +/- 0.95%**		100.0000%	100.0000%

[1] Concentration in sample with units of mg of element per gram of sample.

$^{235}U_R$	1.280 mg/g	$^{239}Pu_R$	3.082 mg/g	$^{241}Pu_R$	0.196 mg/g
$^{235}U_R$	3.28E+18 atoms/g	$^{239}Pu_R$	7.76E+18 atoms/g	$^{241}Pu_R$	4.89E+17 atoms/g
$^{238}U_R$	793.586 mg/g	$^{240}Pu_R$	1.367 mg/g	^{148}Nd:	0.202 mg/g
$^{238}U_R$	2.01E+21 atoms/g	$^{240}Pu_R$	3.43E+18 atoms/g	^{148}Nd:	8.23E+17 atoms/g produced

0.017 Nd-148 atoms per Pu fission (corrected for Pu-239 and Pu-241 fission fraction along with Nd-147 capture)

$(^{235}U+^{238}U+^{239}Pu+^{240}Pu+^{241}Pu)_R$	2.02E+21	atoms/g remaining (dominate contributors)
$(^{235}U+^{239}Pu)_C$	4.84E+19	atoms/g consumed (assume dominated by Pu)

Burnup =	**2.34%**
GWd/MT=	**22.45**

8. SUMMARY AND CONCLUSIONS

8.1 Fuel and Clad Performance Found Acceptable

The intermediate-withdrawal PIE has been performed on two capsules irradiated in the reflector of the ATR for a total of 383 EFPDs with an accumulated average burnup of 20.9 GWd/MT. These capsules have been irradiated during 13 ATR operational cycles and have experienced 18 thermal cycles. The average LHGR has been 8.6 kW/ft, which is about 40 percent higher than normally experienced by commercial fuel at this burnup.

Both Capsule 2 (containing Fuel Pin 5) and Capsule 9 (containing Fuel Pin 12) were visually and dimensionally examined. No signs of capsule damage or distortion were observed. Gamma scans indicated that all internal components (pellets, end caps, and spring) were in their initial locations, and there were no signs of fuel pin damage or distortion. The extent of end-pellet peaking as exhibited by the gamma scans is in accordance with the MCNP code predictions used for the pretest thermal-hydraulic analyses. Measurement of internal gas pressure was successful, indicated no fuel pin leakage, and the pressure was within expectations. The capsules were opened by cutting at the bottom, just above the weld. After the capsules were opened, the fuel pins were removed and visually and dimensionally inspected.

Metallographic examination of fuel specimens revealed good performance; nothing detrimental or unexpected was noted. The observed plutonium rich agglomerates were larger than is expected in mission fuel, but are not troublesome. The pellet cracking is considered normal.

Sectioned fuel was polished, etched, and gamma-scanned. The fuel exhibited no restructuring, and the microstructure appeared essentially unchanged when compared to the unirradiated condition. The extent of fuel swelling, as inferred from polished cross sections, was studied in detail and found to be in accordance with expectations based on reviews of the available literature.

The qualitative gamma scan indicated that the burnup profile is off-center peaked, as expected from the MNCP code pretest calculations, but the peaking is not as strong as noted in the 8 GWd/MT scan [Ref. 13]. Selected segments of the clad were set aside for later ductility testing.

Gallium analyses of fuel and clad specimens indicate no significant migration of the gallium to the clad. The preirradiation level of gallium in the clad is sufficient to mask any small transfer, but a conservative bounding analysis places a maximum upper bound of no more than 9% of the gallium for the non-TIGR treated fuel and 14% for the TIGR treated fuel. This is an improvement over the 8 GWd/MT PIE results, where the gallium measurements were less precise and the upper bounds were conservatively placed at 27% for the TIGR treated fuel.

Overall, the capsules handled the irradiation without incident and there are no indications of any mechanisms that may result in threats to containment integrity from continued irradiation of the

sister capsules. There are no significant differences in the observed states of the untreated (Fuel Pin 5) and TIGR-treated (Fuel Pin 12) pellets. The PIE results support the conservative predictions of the best-estimate CARTS code calculations as discussed in Chapter 3, and were used to better understand fuel and fuel clad behavior as discussed in Chapter 6.

8.2 Pellet Densification and Permanent Clad Expansion

Analyses of the intermediate-withdrawal and early-withdrawal fuel pellet cross section photographs has provided conclusive evidence that fuel pellet densification has occurred. The safety analyses for Phase IV include a zero-densification assumption, which is appropriate for the conservative calculations. However, the realistic calculations to predict hot cell conditions for the 30-GWd/MT and future withdrawals will employ the densifications (2.0 percent for use with the ESCORE swelling model and 1.5 percent for the FRAPCON swelling model) as determined from the current analyses.

There is also clear evidence of a progressive expansion of the clad. This expansion is permanent, persisting after cooling has caused the pellet to shrink away from the inner clad surface. The extent is small, about 0.2 percent diametral. Although the direction is outward, not inward, the magnitude is consistent with the radiation-induced clad expansions and examples of clad creep documented in the literature. This observed clad expansion will be represented in future predictions for this test irradiation.

It should be noted that an important consequence of the outward clad creep and the greater-than-expected pellet densification is that when these effects are modeled in the CARTS calculations, pellet-clad contact is no longer predicted during any of the irradiation phases. As discussed in Chapter 3 of this report, pellet-clad contact (and the associated clad mechanical strain) were predicted by the pretest calculations for this intermediate withdrawal.

8.3 Clad Samples Identified for Future Testing

Two clad sections were prepared but not destructively tested during this PIE; they were set aside for later ductility testing when the necessary test apparatus has been fabricated and installed in the hot cell. Table 8.1 lists these items along with the samples stored from the previous PIE task. It should be noted that the fuel pin 2 and 9 samples are relatively long, and can be subdivided as desired in the future. Four of the samples were left fueled, pending defueling instructions, to avoid compromising later tests should a specific defueling method be required.

Table 8.1 Clad Samples Archived for Later Testing					
Capsule	**Fuel Pin**	**Fuel Type**	**Sample**	**Approx. Length (inches)**	**State**
1	2	Non-TIGR	Upper clad region of Fuel Pin 2	1.6	Fuel removed
8	11	TIGR	½ of Top weld of Fuel Pin 11, Sample FP-11-TW	N/A	Ready for potting
8	11	TIGR	Upper clad region of Fuel Pin 11, Sample FP-11-C-6	2.4	Fueled
8	11	TIGR	Lower clad region of Fuel Pin 11, Sample FP-11-C-8	2.4	Fueled
8	11	TIGR	½ of Bottom weld of Fuel Pin 11, Sample FP-11-BW	N/A	Ready for potting
2	5	Non-TIGR	Middle clad region of Fuel Pin 5, Sample FP-5-C-5	3.8	Fueled
9	12	TIGR	Middle clad region of Fuel Pin 12, Sample FP-12-C-2	5.2	Fueled

9. ACKNOWLEDGMENTS

The authors wish to thank Steve Childs, Charlie DeVore, Tom Kenney, Pat Howard, and Jeff Moody of the Irradiated Fuels Examination Laboratory Staff for their help with the MOX capsule PIE task; thanks also go to Hu Longmire of the Metals and Ceramics Division for performing the metallographic work. The SEM/microprobe task was performed by Larry Walker, also from the Metals and Ceramics Division, who supported us both in the task and with equipment testing. In addition, we wish to express our appreciation to John Keller and Joseph Giaquinto of the Radioactive Materials Analysis Laboratory for performing the radiochemical analysis.

10. REFERENCES

1. B.S. Cowell and S.A. Hodge, *Fissile Materials Disposition Program Light-Water Reactor Mixed Oxide Fuel Irradiation Test Project Plan*, ORNL/TM-13419, Rev 1, Feb 1998

2. B.S. Cowell, *Technical Specification: Mixed-Oxide Pellets for the Light-Water Reactor Irradiation Demonstration Test*, ORNL/MD/LTR-75, June 1997

3. K.R. Thoms, *Design, Functional, and Operational Requirements for the Advanced Test Reactor Mixed Oxide Fuel Irradiation Experiment*, ORNL/MD/LTR-76, September 1997

4. B.S. Cowell, *Purchase Order: Mixed-Oxide Pellets and Fuel Pin Assemblies*, ORNL/MD/LTR-77, August 1997

5. S.A. Hodge, *Effects of Fission Gas Release and Pellet Swelling Within the LWR Mixed Oxide Irradiation Test Assembly*, ORNL/MD/LTR-83 Rev 1, November 1997

6. L.J. Ott, *Thermal/Hydraulic Calculations for the LWR MOX Irradiation Test Assembly at 12 KW/FT*, ORNL/MD/LTR-85, Vol. 1&2, October 1997

7. B.S. Cowell, *Purchase Order: Mixed-Oxide Capsule Assemblies*, ORNL/MD/LTR-90, Rev 0, August 1997

8. B.S. Cowell and S.A. Hodge, *ATR Capsule Assembly Loading and Operation Schedule*, ORNL/MD/LTR-91 Rev 3, August 2000

9. R.N. Morris, *MOX Capsule Post-Irradiation Examination Vol. I: Test Plan for Low Burnup Fuel*, ORNL/MD/LTR-93, August 1997

10. R.N. Morris, J. Giaquinto, S.A. Hodge, *MOX Average Power Test Fuel Pellet Initial Gallium Content*, ORNL/MD/LTR-182

11. S. A. Hodge, *Fission Gas Release and Pellet Swelling Within the Capsule Assembly During Phase IV of the Average Power Test*, Revision 0, ORNL/MD/LTR-184, Oak Ridge National Laboratory, July 2000.

12. L. J. Ott, *Thermal/Hydraulic Calculations for Phase IV of the LWR MOX Irradiation Average-Power Test*, Revision 0, ORNL/MD/LTR-191, Oak Ridge National Laboratory, July 2000.

13. R.N. Morris, et. al., *MOX Average Power Early PIE: 8 GWd/MT Final Report*, ORNL/MD/LTR-172, November 1999

14. W.K. Terry, *As-Run Radiological Characterization of MOX Fuel Capsules Removed From the ATR After Cycle 120A - WKT-04-99*, November 8, 1999

15. Y.Guerin, et al., *Microstructure Evolution and In-Reactor Behaviour of MOX Fuel*, International Topical Meeting on Light Water Reactor Fuel Performance, Park City, Utah, April 10-13, 2000.

16. R.N. Morris, C.A. Baldwin, C.M. Malone, *MOX Fission Gas Pressure Measuring Apparatus*, ORNL/MD/LTR-176, January 2000

17. *ESCORE - the EPRI Steady-State Core Reload Evaluator Code: General Description*, prepared by Combustion Engineering, Inc., Windsor, Connecticut, EPRI NP-5100, February 1987.

18. G. A. Berna, et al., *FRAPCON-3: A Computer Code for the Calculation of Steady-State, Thermal-Mechanical Behavior of Oxide Fuel Rods for High Burnup*, NUREG/CR-6534, December 1997.

19. F. Garzarolli, et al., *Behavior and Properties of Zircaloys in Power Reactors: A Short Review of Pertinent Aspects in LWR Fuel*, Zirconium in the Nuclear Industry: Eleventh International Symposium, ASTM STP 1295, 1996, pages 12-32.

11. DISTRIBUTION

1. P.T. Rhoads, U.S. Department of Energy, MD-3, 1000 Independence Avenue SW, Forrestal Building 6G-050, Washington DC 20585
2. J. Thompson, U.S. Department of Energy, MD-3, 1000 Independence Avenue SW, Forrestal Building 6G-050, Washington DC 20585

3-7. D. Alberstein, Los Alamos National Laboratory, P.O. Box 1663, Los Alamos, NM 87545

8-12. R.C. Pedersen, Idaho National Engineering and Environmental Laboratory, EROB, 2525 Fremont Avenue, Idaho Falls, ID 83415-3419

13. P. Kasik, MPR Associates Inc., 320 King Street, Alexandria, VA 22314-3238
14. C.A. Baldwin
15. B.S. Cowell
16. S.R. Greene
17. D.W. Heatherly

18-22. S.A. Hodge

23. L.L. Horton
24. M.W. Kennard, Stoller Nuclear Fuel, 485 Washington Avenue, Pleasantville, NY 10570

25.-29. L.L. Losh, Framatome Cogema Fuels, 3315 Old Forest Road, Lynchburg, Va 24506

30-34. C.M. Malone

35-39. R.N. Morris

40. L.J. Ott
41. N.H. Packan
42. D.J. Spellman
43. K.R. Thoms
44. ORNL Laboratory Records (RC)